HAL
open science

Prominences and their eruptions as observed with the IRIS mission and ancillary instruments

Ping Zhang

To cite this version:

Ping Zhang. Prominences and their eruptions as observed with the IRIS mission and ancillary instruments. Solar and Stellar Astrophysics [astro-ph.SR]. Université Paris Saclay (COmUE), 2019. English. NNT : 2019SACLS064 . tel-02094359

HAL Id: tel-02094359

https://theses.hal.science/tel-02094359

Submitted on 9 Apr 2019

HAL is a multi-disciplinary open access archive for the deposit and dissemination of scientific research documents, whether they are published or not. The documents may come from teaching and research institutions in France or abroad, or from public or private research centers.

L'archive ouverte pluridisciplinaire **HAL**, est destinée au dépôt et à la diffusion de documents scientifiques de niveau recherche, publiés ou non, émanant des établissements d'enseignement et de recherche français ou étrangers, des laboratoires publics ou privés.

université PARIS-SACLAY

UNIVERSITÉ PARIS SUD
Comprendre le monde, construire l'avenir

NNT : 2019SACLS064

Prominences and their eruptions as observed with the IRIS mission and ancillary instruments

Thèse de doctorat de l'Université Paris-Saclay
préparée à l'Université Paris-Sud

Ecole doctorale n°572 Ondes et Matière (EDOM)
Spécialité de doctorat: Physique des plasmas

Thèse présentée et soutenue à Orsay, le 25 février 2019, par

PING ZHANG

Composition du Jury :

Karine Bocchialini Institut d'Astrophysique spatiale, Université Paris-Sud	Présidente
Oddbjørn Engvold Institute of Theoretical Astrophysics, NORVÈGE	Rapporteur
Wei Liu Lockheed Institute for Space Research, Stanford University, ETATS-UNIS	Rapporteur
Nicolas Labrosse School of Physics and Astronomy, University of Glasgow, ROYAUME-UNI	Examinateur
Stephane Régnier Mathematics, Physics and Electrical Engineering, Northumbria University, ROYAUME-UNI	Examinateur
Éric Buchlin Institut d'Astrophysique spatiale, Université Paris-Sud	Directeur de thèse
Jean-Claude Vial Institut d'Astrophysique spatiale, Université Paris-Sud	Co-directeur de thèse
Petr Heinzel Astronomical Institute, Czech REPUBLIC	Invité

Thèse de doctorat

Acknowledgements

First of all, I would like to express my sincere gratitude to my supervisors, Dr. Eric Buchlin and Jean-Claude Vial, for their guidance throughout my PhD. Not only did they support my PhD work, but they also helped a lot with my life in France, e.g., the application of my Visa and accommodation.

I am also grateful to the rest of my thesis committee: Prof. Bocchialini, Prof. Engvold, Prof. Liu, Prof. Labrosse, Prof. Régnier and Prof. Heinzel for their encouragement, insightful comments, questions and suggestions.

I would like to thank all the members of the solar group at IAS for the stimulating discussions and the support. Many thanks to Prof. Leibacher and Susanna for the insightful comments and advice to improve my presentation.

My sincere thanks also go to all the members of IAS and the faculty of Universite Paris-Sud for all the support I have received during my study in France. Thanks to the computer center staff for helping me in the technical problems. I am deeply thankful to Dr. Yuying Zhang and Dr. Xueyan Song for their consideration and encouragement.

I also thank all the members of the IRIS science team at LMSAL. Many thanks to Prof. De Pontieu and Paola for the guidance during my training and planning there as the IRIS planner.

Last but not least, I would like to express my deepest gratitude and appreciation to my family members for their support, encouragement and heart warming messages.

Abstract

Solar prominences are very large-scale magnetic structures in the solar atmosphere. They have been investigated for many decades, but the issues of their formation, stability, and eruption are still not well understood.

Much progress has been made in our knowledge of prominences and their eruptions with both synoptic (continuous) measurements from space (with SoHO/EIT, STEREO/SECCHI/EUVI, and SDO/AIA) and multiwavelength spectroimaging. Since the launch of IRIS in 2013, a lot of results have been obtained in both observational and modeling domains with IRIS high spectral and spatial resolution imaging and spectroscopy.

In this thesis we focus on the observational signatures of the processes which have been put forward for explaining eruptive prominences. We also try to figure out the variations of physical conditions of the eruptive prominence and estimate the masses leaving the Sun vs. the masses returning to the Sun during the eruption.

As far as velocities are concerned, we derive a full velocity vector for each pixel of the observed prominence by combining an optical flow method on the AIA 304 Å and IRIS Mg II h&k images in order to derive the plane-of-sky velocities and a Doppler technique on the IRIS Mg II h&k profiles to compute the line-of-sight velocities. As far as densities and temperatures are concerned, we compare the absolute observed intensities with values derived from Non Local Thermodynamic Equilibrium (NLTE) radiative transfer computations to build pixel per pixel maps of these quantities. The derived electron densities range from 1.3×10^9 to 7.0×10^{10} cm^{-3} and the derived total hydrogen densities range from 1.5×10^9 to 3.6×10^{11} cm^{-3} in different regions of the prominence. The mean temperature is around 1.1×10^4 K which is higher than in quiescent prominences. The ionization degree is in the range of 0.1 to 10.

The mass flows in the prominence and their variations with time are consequently computed. The derived total hydrogen mass is in the range of 1.3×10^{14} to 3.0×10^{14} g. The total mass drainage from the prominence to the solar surface during the whole observation time of IRIS is about one order of magnitude smaller than the total mass of the prominence.

We also explore the correlations between the observable spectral features in h and k lines of Mg II to physical quantities such as the density and the Emission Measure (EM). We choose to compute one-dimensional (1D) isothermal and isobaric models using the PRODOP_Mg NLTE code available at MEDOC (IAS) with the exact computation of the incident radiation. Then we derive correlations between the k and h emergent intensities on one hand and the densities and EM on the other hand. With some assumptions on the temperature we obtain a unique

relation between the k (and h) intensities and the EM that should be useful for deriving either the hydrogen and electron densities or the effective thickness of an observed prominence.

Thus, the detailed evolution of the morphology and thermodynamic properties of an erupting prominence have been investigated in this thesis. These studies can help us to better understand some aspects of prominences, e.g., the distribution and evolution of densities, temperatures, velocities and ionization degree. These could be useful constraints for theoretical prominence models. In the conclusion, we summarize our results and provide some suggestions for future analysis, observations and ideal observing capabilities.

Contents

List of Figures **9**

List of Tables **13**

1 Solar Prominences **1**
1.1 What are solar prominences? . . . 1
1.2 Classifications . . . 3
1.3 Substructures of prominences . . . 5
1.4 Prominence models . . . 7
1.5 Prominence eruptions . . . 12
1.5.1 Models for eruptions . . . 13
1.5.2 Observational properties . . . 14
1.6 Spectral Diagnostics . . . 16
1.6.1 Spectral inversion for optically thin lines . . . 16
1.6.2 NLTE modeling . . . 18

2 Instruments and data analysis techniques **21**
2.1 IRIS . . . 21
2.2 SDO . . . 24
2.2.1 AIA . . . 25
2.3 STEREO . . . 26
2.3.1 SECCHI/EUVI . . . 26
2.4 COSMO . . . 27
2.4.1 K-COR . . . 28
2.5 Data analysis techniques . . . 29
2.5.1 Data archives . . . 29
2.5.2 3D reconstruction . . . 30
2.5.3 The Radiometric calibration . . . 32

3 Launch of a CME-associated eruptive prominence **37**
3.1 Introduction . . . 37
3.2 Observations . . . 37

3.3 Data analysis 40
3.3.1 Prominence morphology and geometry evolution 40
3.3.2 Velocities in the prominence 47
3.3.3 Mg k/h ratio 60
3.4 Diagnostics of density, temperature, and ionization degree 63
3.5 Hydrogen Mass flows 76
3.6 Discussion 79

4 Spectral diagnostics of prominence plasma 81
4.1 Description of PRODOP_Mg 81
4.2 Grid of models 83
4.2.1 Boundary conditions 84
4.3 Results 84
4.4 Conclusion 91

5 Two weeks as an IRIS planner 93
5.1 The daily plan 93
5.1.1 Calibration and Coordination 93
5.1.2 Timeline 97
5.2 Post-planning activities: data verification and presenting highlights 104
5.3 Conclusions 104

6 Discussion and Conclusion 107

Bibliography 111

Appendix A Computation of the incident radiation 123

French and English Abstracts 125

List of Figures

1.1 Example of prominences and filaments observed in Hα and 304 Å. 2
1.2 Examples of active region, intermediate, quiescent and polar crown prominences 4
1.3 High resolution Hα image of parts of the southern end of a multi-thread filament observed by the 1-meter Swedish Solar Telescope (SST) on 26 August 2003 . 5
1.4 A Hα image of a filament and the 3 structural components: spine, barbs and two legs 6
1.5 Schematic representations of the general chirality relations 7
1.6 Schematic diagram showing the normal-polarity and the inverse-polarity configurations (right panel) of a filament. 8
1.7 Sheared arcade model for a filament channel 9
1.8 Formation of a flux rope 10
1.9 Sketch of an injection model 11
1.10 Sketch of a levitation model. 11
1.11 A prominence eruption observed on August 31, 2012 by the Solar Dynamics Observatory 12
1.12 Schematic view of the CME features 14
1.13 RHESSI X-ray contours over plotted on TRACE 195 images. 15
1.14 Theoretical values of contribution functions for the O III and O IV lines 18

2.1 Schematic diagram of the light path in the IRIS instrument 22
2.2 IRIS SJI image observed at 05:24 UT on Dec 14 23
2.3 Examples of three raster modes of IRIS 24
2.4 The SDO satellite with the three instruments 25
2.5 The Sun observed by STEREO-A and B from two other different directions . . 27
2.6 Schematic diagram of K-COR 28
2.7 Schematic diagram of the geometry of a prominence observed with STEREO A and B 31
2.8 The STEREO-A and SDO images. 32
2.9 The in-flight sensitivity degradation of the IRIS NUV spectrograph 33
2.10 Spectra of Mg II k and h lines at disk center and $\mu = 0.23$ (Kohl and Parkinson, 1976). 34

2.11 IRIS mosaic observation made on May 27, 2014. 34
2.12 Averaged Mg II k and h profiles over a region of 100"×100" at the center of the Sun 35
2.13 IRIS slit-jaw image in 1400 Å and the corresponding Mg II k&h spectra 36
2.14 Calibrated profiles from IRESP and KP methods 36

3.1 The spectra of the Mg II and C II lines 39
3.2 The time variations of the integrated DN of the Mg II and C II lines 39
3.3 Images obtained by SDO/AIA in the He II 304 Å line at different times before (left) and during the prominence eruption (middle, right). 40
3.4 The positions of the Sun, Earth and STEREO-A/B satellites for 2014-05-28 16:00 UT. 41
3.5 Images obtained by the EUVI instrument on board STEREO A at 16:16:15 UT (a) and STEREO B at 16:16:38 UT (b) in the He II 304 Å channel. 41
3.6 High contrast images taken by K-COR on May 28 2014 42
3.7 SOHO LASCO C2 difference image from the CACTUS database at 23:36 UT . 42
3.8 The STEREO-A image and SDO image of the prominence 43
3.9 Full disk Hα image on 28 March 2014 taken by GONG. 44
3.10 (a) Hα image of the filament on 21 May 2014 taken by Big Bear Solar Observatory (BBSO). (b) He II 304 Å image of the filament on 21 May 2014 taken by SDO/AIA. 45
3.11 3D reconstruction with STEREO A and AIA image pairs (in red) and STEREO A and B image pairs (in green). 45
3.12 The 3D geometry of the prominence at 16:16 UT 46
3.13 The SDO and STEREO-A images of the prominence observed at 16:16 UT . . 47
3.14 Prominence observed by AIA in the He II 304 Å channel at 20:06 (left), 20:16 (middle) and 20:26 UT (right) 48
3.15 Stonyhurst heliographic longitudes and latitudes of the feature tracked at 20:06 (red), 20:16 (blue) and 20:26 UT (green) 49
3.16 A diagram showing the outline of a prominence during the eruption 50
3.17 Altitude of the top of the prominence tracked in IRIS ($*$), SDO/AIA (+) and K-COR ($\diamond$). 51
3.18 POS velocity derived from AIA image pairs 52
3.19 POS velocity derived from AIA image pairs and IRIS image pairs 53
3.20 Some spatially-resolved spectra of Mg II k (blue) and h (red) lines observed by IRIS in the prominence. 54
3.21 The spatial distribution of the 3 groups of profiles in the prominence 55
3.22 Prominence observed by IRIS on May 28, 2014. 56
3.23 The averaged spectra of Mg II k and h lines respectively. 57

3.24 Doppler shifts computed from the extremum-finding of the Mg II k&h line profiles between 15:10 and 15:27 UT. 58
3.25 Mg II k and h spectra derived in the prominence. 59
3.26 Doppler shifts computed from the center of gravity of the Mg II k&h line profiles at different times. 61
3.27 Composite velocity map derived from IRIS spectral and SJI observations between 15:10 and 15:27 UT. 62
3.28 Map of the Mg II k/h intensity ratio in the prominence derived from IRIS spectral observations 63
3.29 Calculation of incident radiation 64
3.30 The derivatives of the full disk average intensity variations close to the limb . . 65
3.31 Composite Carrington map of the solar hemisphere centered on 90° Carrington longitude, with the IRIS mosaic of 2014-05-27 66
3.32 Left: IRIS mosaic image taken on 2017-03-12 in Mg II k line. Right: The mean profile of Mg II k line averaged over the full disk in the left panel. 67
3.33 Radial variation of intensity in k_3 and k_{2v} 68
3.34 Mean profiles of Mg II k derived from IRIS mosaic observation on 2017-03-12. . 68
3.35 Incident Mg II h and k profiles at an altitude of 10 000 km. 69
3.36 How a pair of observed k (in green) and h (in red) line intensities change with pressure and temperature. 69
3.37 Electron density, hydrogen density and temperature in the prominence derived from IRIS spectral observations between 11:24 and 11:42 UT (top) and between 13:08 and 13:26 UT (bottom) 70
3.38 Electron density, hydrogen density and temperature in the prominence derived from IRIS spectral observations between 14:52 and 15:10 UT (top) and between 15:10 and 15:27 UT (bottom) 71
3.39 Electron density, hydrogen density and temperature in the prominence derived from IRIS spectral observations between 15:27 and 15:44 UT (top) and between 15:44 and 16:01 UT (bottom) 72
3.40 Ionization degree in the prominence higher than 10 000 km above the limb . . . 75
3.41 The spatial distribution of the groups of profiles in the prominence from observations and models 76
3.42 Total (hydrogen) mass of the prominence in the FOV of IRIS spectral observation as a function of time, between 11:24 and 16:01 UT. 78
3.43 Mean temperature of the prominence in the FOV of IRIS spectral observation as a function of time, between 11:24 and 16:01 UT. 78

4.1 Schematic diagram showing a parallel slab standing vertically above the surface of the Sun, illuminated by the incident radiation from the surrounding solar atmosphere 82

4.2 Magnesium energy diagram 83
4.3 Integrated Mg II k line intensity as a function of the EM 85
4.4 Integrated Mg II h line intensity as a function of the EM 85
4.5 Integrated Mg II k line intensity as a function of the EM for radial velocities of 0 and $20\,\mathrm{km\,s^{-1}}$ 86
4.6 Integrated Mg II k and h line intensities change with velocities 87
4.7 Integrated Mg II k line intensity as a function of the hydrogen EM for a zero radial velocity, with observed intensities 88
4.8 Integrated Mg II k line intensity as a function of the square of the hydrogen density and the hydrogen EM for three values of the thicknesses 89
4.9 Integrated Mg II k line intensities change with the hydrogen EM. The different colors represent different temperatures and thickesses. 90
4.10 How the k/h ratios change with k line intensities at different temperatures . . . 90
4.11 The variations of k/h ratios with the k line intensities approximated through fitting procedure. 91

5.1 The pointing preview and the derived IRIS SJI image on Dec 15 96
5.2 The pointing preview and the derived IRIS SJI image on April 1st 98
5.3 A STEREO/EUVI full-disk image in 304 Å taken at 16:15 UT on Dec 13 and a IRIS SJI image observed at 07:10 UT on Dec 14 99
5.4 An AR tracked as it crosses the disk. 99
5.5 The monochromatic images in 2795.86 Å derived from the IRIS spectral observations from 06:06 UT to 06:14 UT 100
5.6 OBS ID numbering scheme (ITN 31). 101
5.7 Timeline from 4UT Mar 30 to 4UT Apr 1, 2018. 102
5.8 Timeline from 4UT to 19 UT on Mar 30, 2018. 103
5.9 One IRIS SJI image at 13:08 UT on Apr 1, 2018 in 1330Å. 104

List of Tables

1.1 Key plasma parameters such as electron temperature, electron density, pressure, microturbulent velocity, ionization degree and flow velocities in the prominence core and the PCTR 1

2.1 Key parameters of IRIS (De Pontieu et al., 2014). 23
2.2 Critical parameters of AIA onboard SDO (Lemen et al., 2011). 26
2.3 Critical parameters of EUVI (Howard et al., 2008). 27
2.4 Key parameters of the K-Cor instrument 29

3.1 Summary of observations on May 28th 2014. 38
3.2 The derived ranges of temperature, electron density, total hydrogen density and ionization degree in the prominence. 73

4.1 Grid of 1D-slab models used in this work. 84

Chapter 1

Solar Prominences

1.1 What are solar prominences?

Solar prominences are spectacular magnetic structures in the solar atmosphere. They consist of cool and dense plasma supported and confined in the hot solar corona (Tandberg-Hanssen, 1995; Labrosse et al., 2010; Mackay et al., 2010; Vial and Engvold, 2015). Their temperature ($\sim 10^4$ K) is about two magnitudes lower than that of the corona, and their density ($\sim 10^9$-10^{11} cm^{-3}) is about two magnitudes higher than that of the corona (Tandberg-Hanssen, 1995; Labrosse et al., 2010). Their external envelope is usually called the Prominence Corona Transition Region (PCTR) (Vial, 1990). Similar to the transition region between the corona and the chromosphere, PCTR is an interface region between the corona and the prominence, where the temperature rises from about 7000 K to a million K (Parenti and Vial, 2013). Some of the key parameters of the prominence plasma such as electron temperature, electron density, pressure, microturbulent velocity, ionization degree and flow velocities are listed in Table 1.1.

The plasma in the cool core of the prominence is partially ionized, because of the low temperature. And the plasma is optically thick in most of the resonance lines and continuum of hydrogen and helium, because of the high density (Labrosse and Gouttebroze, 2004). When observed on the disk, they are darker than their surrounding due to the absorption of the

Table 1.1 Key plasma parameters such as electron temperature, electron density, pressure, microturbulent velocity, ionization degree and flow velocities in the prominence core and the PCTR (Labrosse et al., 2010, adapted from Engvold et al., 1990).

Pysical parameter	Core	PCTR
T(K)	4300-10000	10^4-10^6
n_e (cm^{-3})	10^9-10^{11}	10^6-10^8
p (dyn cm^{-2})	$\sim$0.02-1	$\sim$0.2
ξ_t (km s^{-1})	3-20	30
N(H$^+$)/N(H^0)	0.2-0.9	
V (km s^{-1})	$\sim$5	$\sim$10

background radiation, as shown in the bottom panels of Fig. 1.1, in this case they are known as filaments (Zirker et al., 1998). They are called prominences when observed above the solar limb as bright features, as shown in the top panels of Fig. 1.1. Both filaments and prominences are the same phenomenon, and they are observed as bright or dark features seen from different perspectives. The fact that the prominence plasma is two orders of magnitude cooler and denser than its coronal surroundings raises important questions about the prominence, such as how the prominence plasma is supported and confined in the hot corona, and where the prominence material comes from.

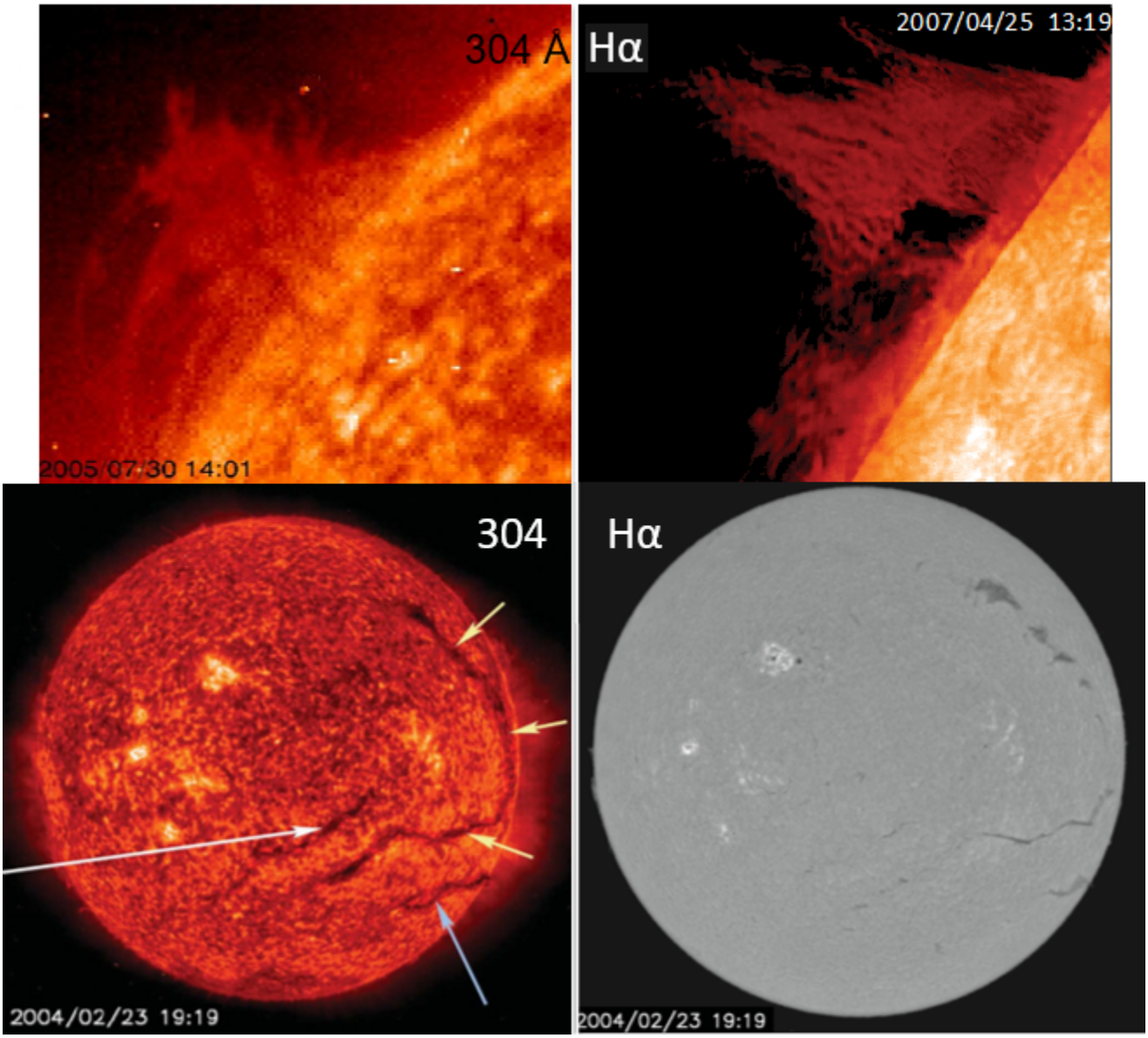

Figure 1.1 Example of prominences and filaments observed in Hα and He II 304 Å by SOHO/EIT (top-left panel and bottom-left panel), Hinode/SOT (top-right panel) and Catania Astrophysical Observatory (bottom-right panel). The filaments are pointed with arrows in the bottom-left panel (Lin et al., 2008a; Heinzel et al., 2008; Parenti, 2014).

1.2 Classifications

Solar prominences have been investigated for many decades. Their formation, stability, and eruption have been very actively studied in recent years. Prominences normally locate along the filament channels. Filament channels are regions in the chromosphere along the Polarity Inversion Line (PIL; Babcock and Babcock, 1955) which separates regions of opposite magnetic polarities. According to the combinations of their various observed properties such as the morphology, the relative locations and the dynamic properties, prominences are divided into many subgroups (Vial and Engvold, 2015). It is very common and practical to divide them into Quiescent Prominences, Active Region Prominences and Intermediate Prominences. Figure 1.2 shows representative examples of different types of prominences.

Quiescent Prominences: Quiescent prominences locate in the quiet Sun. They are quite stable structures and can last from several days to several solar rotations (Kuperus and Tandberg-Hanssen, 1967). Quiescent prominences can be observed as long-lasting vertical sheet-like structures at the limb. A typical prominence has a height of 10 to 100 Mm, a length of 60 to 600 Mm and a thickness of 3 to 10 Mm (Priest, 2014). They have relatively lower magnetic field strengths (3–30 G) than active region prominences (Priest, 2012). The quiescent prominences located at high latitudes (within 30 degrees of the north and south poles) are normally known as Polar Crown prominences.

Active Region Prominences: They usually locate in or around the active regions. Their spines (see Chapter 1.3) are relatively thin and straight, and their barbs (see Chapter 1.3) are in general very few and less conspicuous (Vial and Engvold, 2015). They are shorter in length ($\sim$10 Mm) (Aulanier and Démoulin, 2003) and change more rapidly compared with those that appear in regions away from active regions. Active region prominences are more dynamic than quiescent prominences and usually connected with coronal mass ejections (CMEs) and flares (Tandberg-Hanssen, 1995).

Intermediate Prominences: Intermediate prominences represent the intermediate regime between active region prominences and quiescent prominences. They can be found between decaying active regions (Engvold, 1998). They have a length of about 100 Mm (Vial and Engvold, 2015).

Some prominences with detailed observational motions or shapes can be divided into sub-classes. For example, prominences with tornado-like motions such as rotation around the main axis are usually known as tornado prominences (Pettit, 1950). Coronal cloud prominences are higher (up to 200 Mm) than quiescent prominences (Vial and Engvold, 2015). They usually disappear from drainage within one day.

For the different groups of prominences, although they vary largely in the level of activity or the size, they have the same structure and formation mechanism (Priest, 2014).

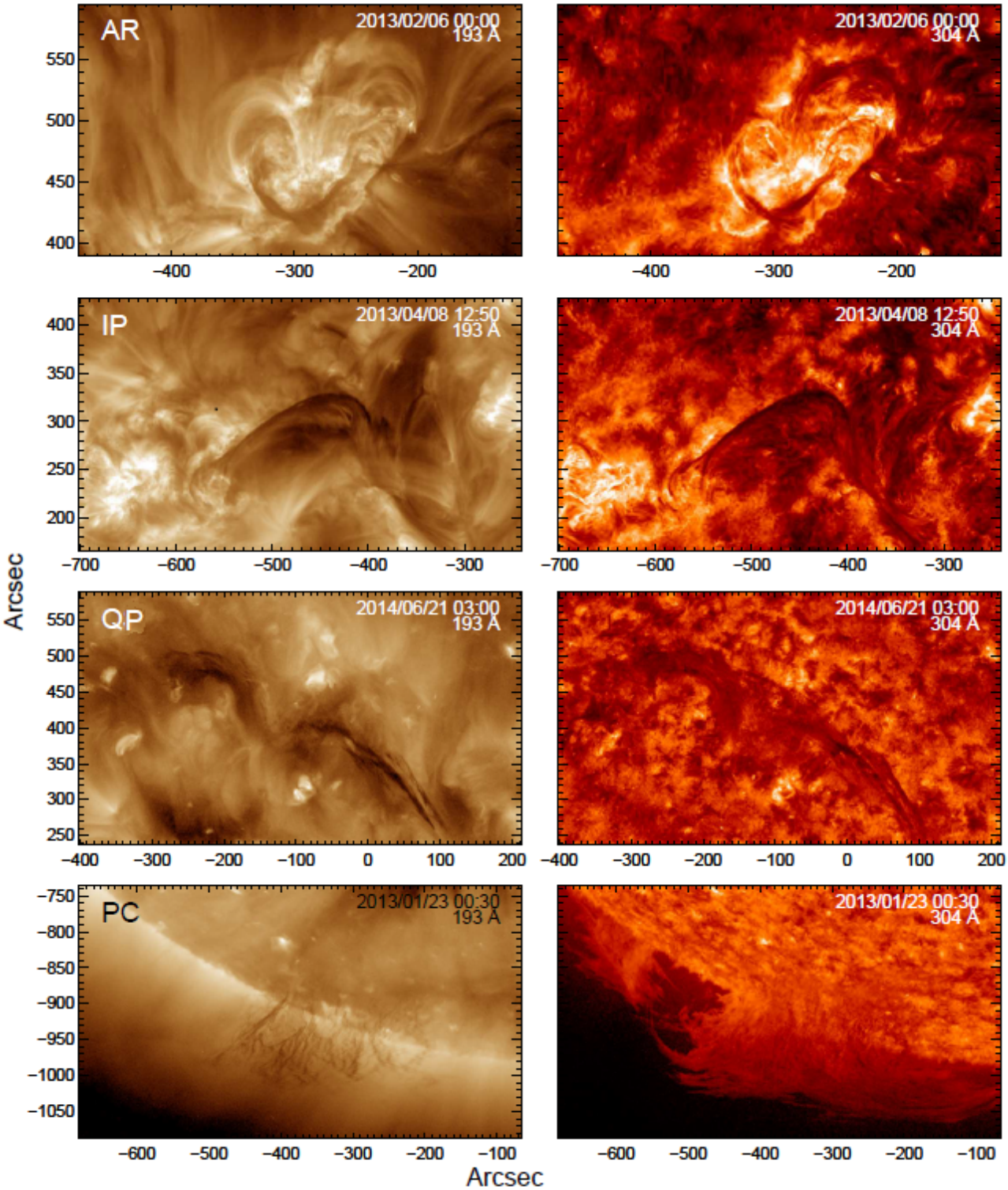

Figure 1.2 Examples of active region, intermediate, quiescent and polar crown prominences (from top to bottom) observed in 193 Å (left) and 304 Å (right) by SDO/AIA (McCauley et al., 2015).

1.3 Substructures of prominences

Recent high temporal and spatial resolution observations from satellites (e.g., the Solar Optical Telescope (SOT) onboard the Hinode satellite, TRACE) and ground-based observatories (e.g., Swedish 1-m Solar Telescope (SST), Dutch Open Telescope (DOT)) have confirmed that the whole prominence body is composed of numerous filamentary fine structures (Vial and Engvold, 2015; Lin et al., 2005a,b). These fine structures known as threads are considered to be the fundamental structures of solar prominences. Threads are rapid changing structures with a lifetime of only a few minutes. They can be seen in the high resolution Hα image as shown in Fig. 1.3, where a multi-thread filament is displayed.

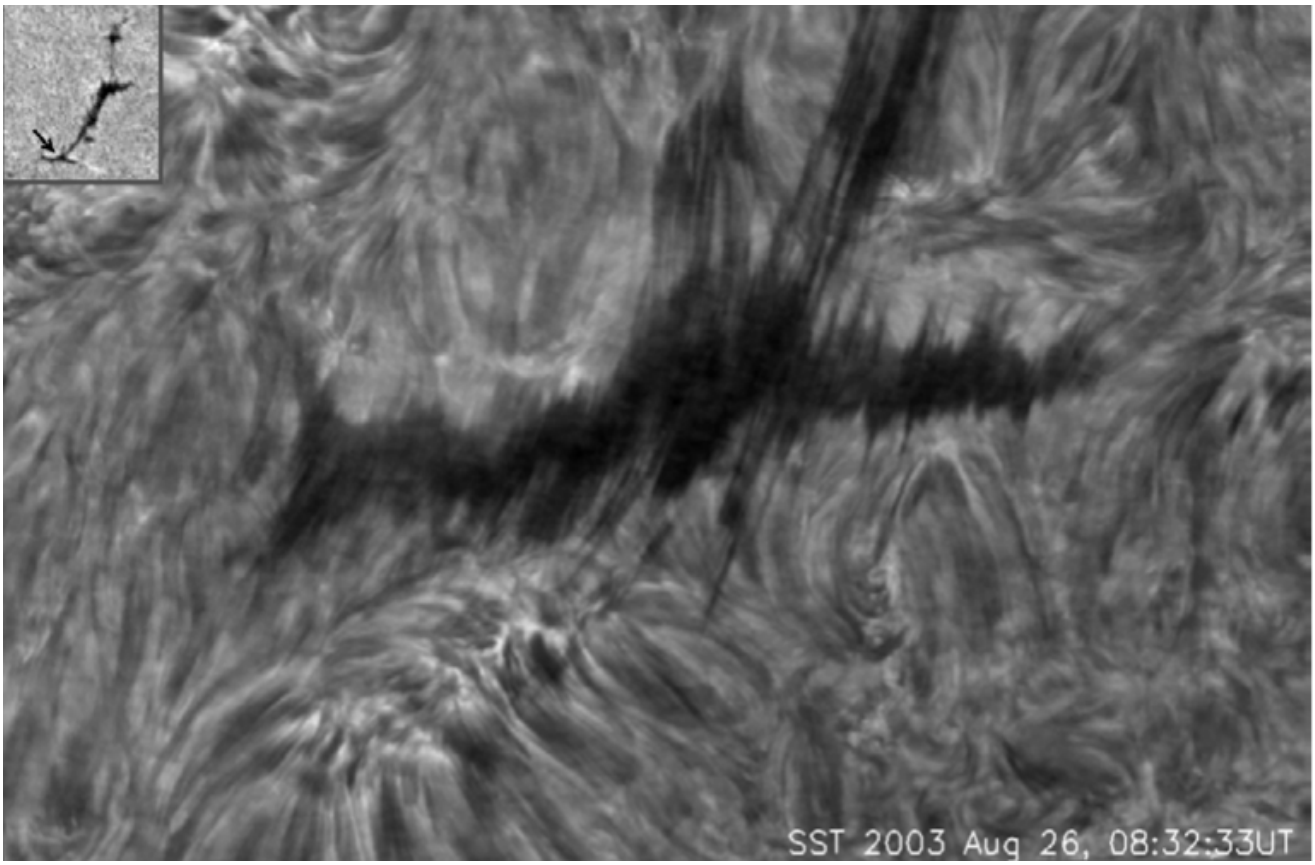

Figure 1.3 High resolution Hα image of parts of the southern end of a multi-thread filament observed by the 1-meter Swedish Solar Telescope (SST) on 26 August 2003 (Lin et al., 2008a).

The size and thickness of the threads vary in different observations, for example, the limb observations compared with disk filaments or quiescent prominences compared with active-region prominences. Lin et al. (2005a, 2008a) found that the widths of the thin threads were no larger than 0.3" in Hα observations. They also mentioned that there were thinner threads whose width was close to the resolution limit ($\sim$0.14") of the present telescopes. In high resolution Hα images, all prominences of different groups are made up of separate thin threads. These thin threads are found to be located in thin bundles of the local magnetic field lines and they are not necessarily aligned with the filament spine (see the following paragraph)

(Lin et al., 2005b, 2007, 2008b, 2009). High-resolution Hα images show that threads have different lengths. In quiescent filaments, thin threads along the spine are commonly short (Malherbe, 1988; Pécseli and Engvold, 2000), while the threads within the barbs (see the following paragraph) or in the active region prominences are relatively longer (Heinzel, 2007). The different lengths may be caused by the different angles between the magnetic field lines and the axis of the filament spine (Mackay et al., 2010). In quiescent prominences they usually appear to be quasi-vertical structures (Berger et al., 2008), while active region prominences usually consist of horizontal threads (Lin et al., 2007, 2008a). Various flows have been reported along the filament spine, as well as in and out of the barbs as unidirectional (Berger et al., 2008) or as bi-directional counter-streaming flows (Zirker et al., 1998; Lin et al., 2003; Berger, 2013).

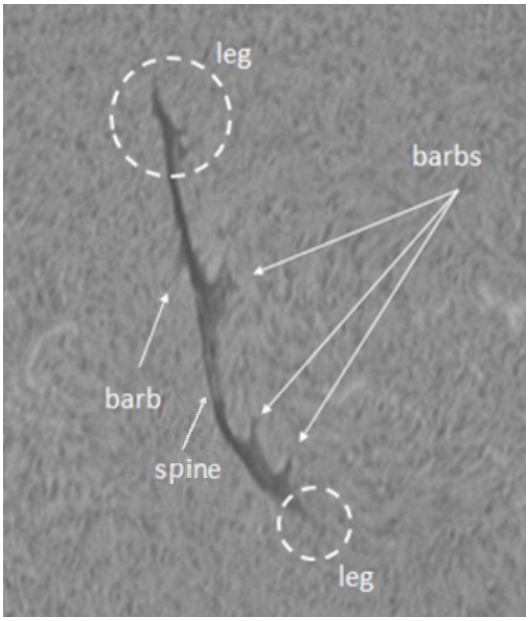

Figure 1.4 Hα image shows three structural components (spine, barbs and two legs) of a filament (Credit: GONG).

A typical solar filament consists of three components : spine, barbs and two extreme ends (also called legs) (Martin, 1998; Mackay et al., 2010), as shown in Figure 1.4. High-resolution Hα images demonstrate that all these structural components are made up of thin threads (Lin et al., 2005a; Mackay et al., 2010; Vial and Engvold, 2015). The spine defines the upper horizontal part of a filament (Lin et al., 2008a). It runs generally along the filament channel and lies above the PIL. The barbs diverge from the spine at an acute angle (Martin et al., 1992; Mackay et al., 2010). When observed at the limb, they extend down towards the chromosphere as inclined structures (Lin et al., 2008a; Mackay et al., 2010). Their association with the underlying photospheric field has been studied for a long time. Martin et al. (1994) and Chae et al. (2005) suggested that the ends of barbs are located between the network elements or in parasitic polarity elements. The extreme ends, also called legs are the beginning and end

points of the filaments. They appear to be a collection of threads that terminate at a single point or multiple points (Lin et al., 2008a).

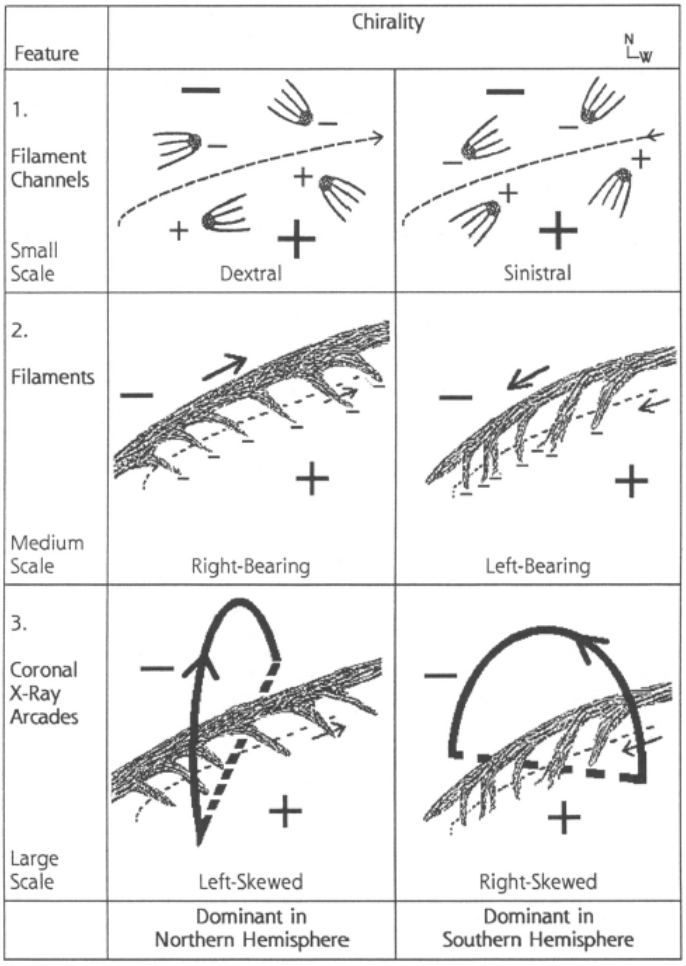

Figure 1.5 The diagram shows schematic representations of the general chirality relations (Martin, 1998).

The extensions of the barbs from the spine reveal the chirality of the filament. This concept was introduced by Martin et al. (1992). Fig. 1.5 shows schematic representations of the chirality relations for different patterns. For the fibril (also known as spicules when observed at the limb) pattern in the upper frame, for a observer standing at the positive polarity side of the filament, the chirality is sinistral when the filament axis directs leftward otherwise, it is dextral. Martin et al. (1994) discovered a tendency in the distribution of the two kinds of filaments. Sinistral Filaments are generally located in the southern hemisphere while dextral filaments are generally located in the northern hemisphere (Martin et al., 1994).

1.4 Prominence models

Various 2D and 3D models have been proposed to answer the critical questions of prominences, such as how do these structures form, how is the dense mass supported and how is the cool

plasma lifted upward (Tandberg-Hanssen, 1995; Mackay et al., 2010). Prominences are observed above the PILs between opposite polarities (Babcock and Babcock, 1955). The configuration of magnetic fields is very important in all these prominence models. In the early works, two major magnetic configurations were proposed to explain the formation of the prominence: the normal-polarity configuration (Kippenhahn and Schlüter, 1957) and the inverse-polarity configuration (Kuperus and Raadu, 1974), as shown in Fig. 1.6. In the normal polarity configuration, the material of the prominence is located in dips of magnetic field lines and is supported by the magnetic tension force against the gravity. In the dips, the directions of the magnetic field lines are the same as those of the underlying photospheric field lines. In the inverse polarity model, the prominence material is supported and isolated from the surrounding corona by a closed magnetic loop. In the dips the directions of the field lines are opposite to those of the photospheric field lines. The existence of the inverse polarity prominences was established on an individual basis for the first time by Leroy et al. (1984). Statistical studies reveal that a large majority (75% - 90%) of prominences belong to the inverse polarity type (Leroy et al., 1984; Bommier et al., 1994; Bommier and Leroy, 1998). The normal polarity prominences are not very commonly observed because the magnetic fields are highly non-potential in the filament channels. Bommier et al. (1994) found that the field strength of the normal polarity prominences is higher than that of the inverse polarity prominences in their study of 14 prominences.

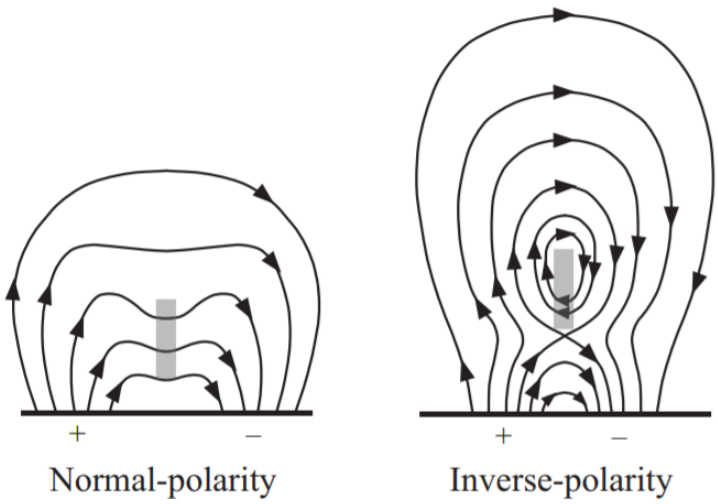

Figure 1.6 Schematic diagram showing the normal-polarity configuration (left panel) and the inverse-polarity configuration (right panel) of a filament. The shaded area represents a filament (Anzer, 1987).

Although the normal polarity and inverse polarity prominence models have been developed to explain the magnetic configuration, the detailed topology of the magnetic fields and the formation of the prominences are still not well understood. These lead to the development of more complex 3D models. All these models can be generally divided into two categories: the sheared arcade model (Antiochos et al., 1994; DeVore and Antiochos, 2000) and the flux

rope model (Kuperus and Raadu, 1974; van Ballegooijen and Martens, 1989; Aulanier and Démoulin, 1998; Chae et al., 2001; Gibson and Fan, 2006). The difference between these two models mainly exists in the height of the prominence formation.

Sheared arcade model

In this model, a sheared magnetic arcade may be formed from initially potential magnetic fields by shearing motions, e.g., the motion of the photospheric footpoints or the differential rotation (Antiochos et al., 1994; DeVore and Antiochos, 2000). In a dipolar region, shearing motions reduce the overlying field and cause the low-lying field lines to rise up at their ends and hence become dipped, as shown in Figure 1.7. The overlying loops are shown in green and the sheared arcade is represented in red. Inverse polarity and normal polarity configurations can both be found in the sheared arcade (Antiochos et al., 1994).

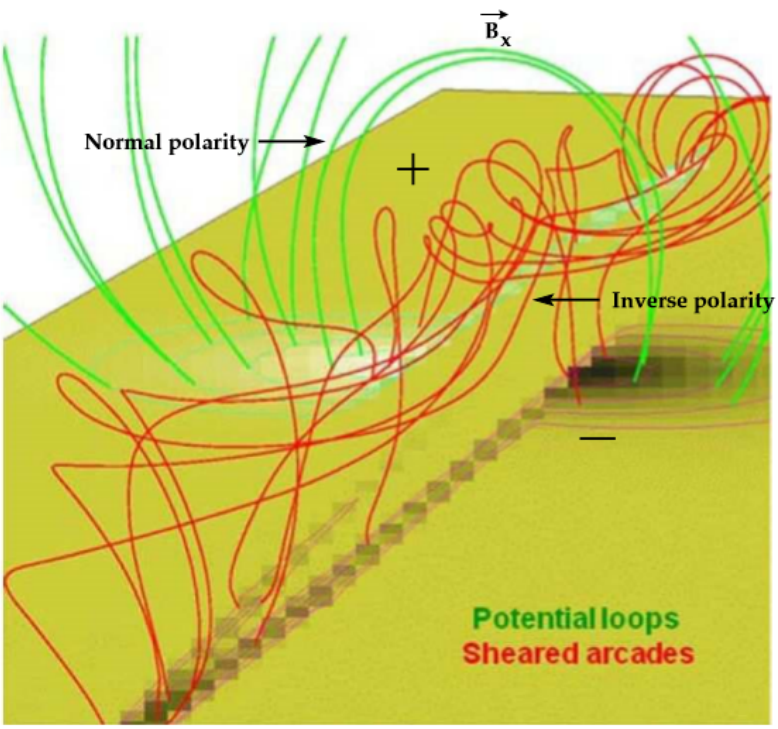

Figure 1.7 Sheared arcade model for a filament channel. The overlying loops are shown in green and the sheared arcade is represented in red (Aulanier et al., 2002) (Adapted from Panesar, 2014).

Flux rope model

In this model, the flux ropes lie horizontally above the PIL and the prominence material lies in the lower part of the rope. In the model proposed by van Ballegooijen and Martens (1989), a flux rope is formed via reconnection at the PIL, as shown in Fig. 1.8. The initially potential

magetic field (Fig. 1.8a) is sheared due to flows along and towards the PIL (Fig. 1.8b,c). One long loop AD and one shorter loop CB are produced by reconnection (Fig.1.8d). The shorter loop CB submerges because of its small radius of curvature (1.8e). A helical loop EH twisted about AD is produced by reconnection between the overlying loops EF and GH in a similar way (Fig.1.8f) and the prominence material can accumulate in the dip of the loop.

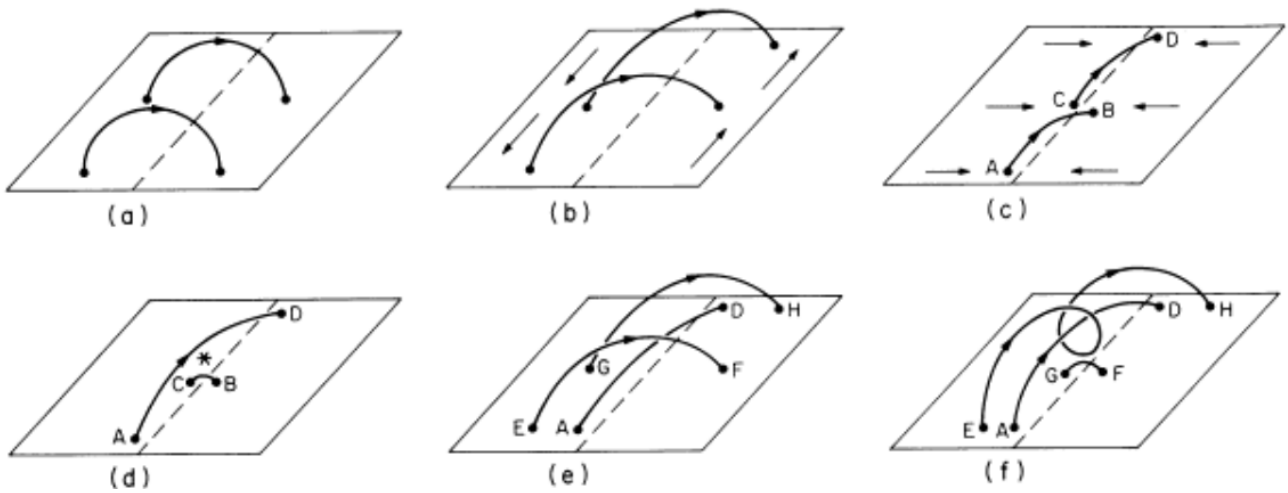

Figure 1.8 The diagram shows the formation of a flux rope. Solid lines are the magnetic field lines and dashed lines show the PIL in each panel (van Ballegooijen and Martens, 1989).

The cool and dense prominence mass must be extracted from the chromosphere, because there is not enough plasma in the ambient corona (**?**Priest and Tandberg-Hanssen, 1989; Zirker et al., 1994). Various models have been developed to understand how the mass comes from the chromosphere, e.g., the injection model (Wang, 1999; Chae, 2001), the levitation model (van Ballegooijen and Martens, 1989; Rust and Kumar, 1994; Litvinenko and Martin, 1999; Deng et al., 2000) and the evaporation-condensation model (Engvold and Jensen, 1977; Serio et al., 1981; Hood and Anzer, 1988; Van Hoven et al., 1992; Antiochos et al., 2000; Karpen and Antiochos, 2008).

Injection model

According to the injection model, cool plasma is ejected upward to typical prominence heights in the flux tubes of a filament channel. The injection of the plasma is generally driven by magnetic reconnection in the solar lower atmosphere. In Fig. 1.9, magnetic reconnection between the filament channel field (black lines) and minority-polarity bipole (blue lines) at one end of a loop leads to the ejection of cool plasma.

Levitation model

In this model, prominence material is levitated by concave upward magnetic field lines as they rise from the lower atmosphere (see Fig. 1.10). Several processes can result in the lifting of

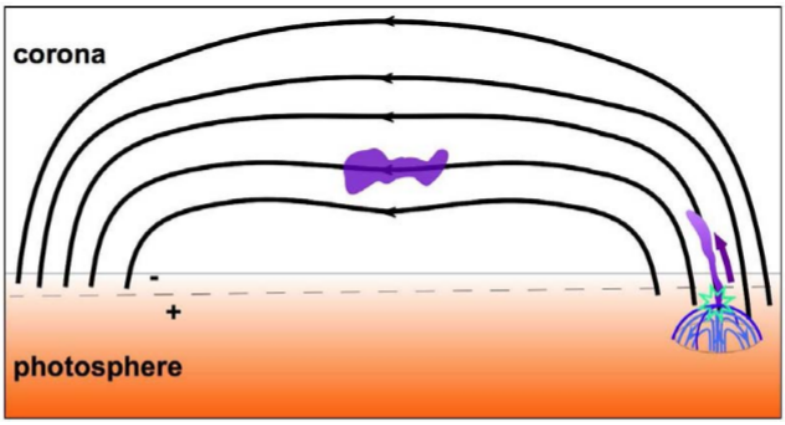

Figure 1.9 In the injection model, the prominence material is in purple. The magnetic field lines of the filament channel are in black. The minority-polarity bipole field lines are in blue (Mackay et al., 2010).

cool plasma, such as the emergence of a highly twisted flux rope that brings up cool plasma (Rust and Kumar, 1994), the emergence of U loops with material trapped in the concave part (van Driel-Gesztelyi et al., 2000; Deng et al., 2000) or the field-line relaxation after magnetic reconnection associated with flux cancellation (Litvinenko and Martin, 1999).

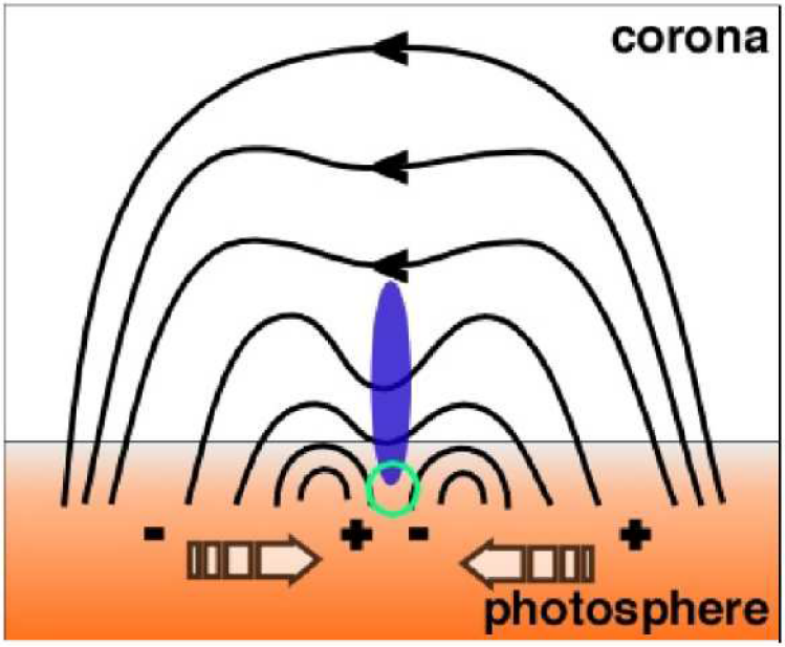

Figure 1.10 A sketch of a levitation model, the plasma is shown in purple. It is lifted by the emergence of U loops. Black lines are the magnetic field lines (Mackay et al., 2010).

Evaporation-condensation model

According to the evaporation-condensation model, concentrating heating in loops leads to the evaporation of the chromospheric plasma, the condensation of the chromospheric mass in

the corona forms the cool plasma in prominences. Different types of heating such as uniform heating, localized heating at the apex (Antiochos and Sturrock, 1978) or the footpoints (Mok et al., 1990; Antiochos, 1998) of the loop have been theoretically analyzed and numerically simulated.

1.5 Prominence eruptions

Although prominences are stable structures, sometimes they can lose their equilibrium and turn into eruptions. Especially the active region prominences are usually accompanied by coronal mass ejections (CMEs) and flares (Webb and Hundhausen, 1987). Figure 1.11 shows the eruption of a long filament on August 31, 2012 observed with the Solar Dynamics Observatory. In most cases, filament eruptions have a common pattern (Sterling and Moore, 2004a,b). The eruption begins with an initial slow-rise phase which may last several hours. In this phase the filament ascends quite slowly (1–15 km s^{-1}) with a very small acceleration. Then there is large acceleration in the following rapid-acceleration phase, and the velocity can increase to 100-1000 km s^{-1} (Schrijver et al., 2008). The combination of the material from the erupting filament and the corona in the launch region forms the bulk of the associated CMEs (Vial and Engvold, 2015). In the final stage the filament reaches a nearly constant speed or may decelerate (Liu et al., 2013, 2016). While the leading front expands outward, some fraction of the core material is observed to return to the Sun (Wang and Sheeley Jr, 2002). (Vial and Engvold, 2015)

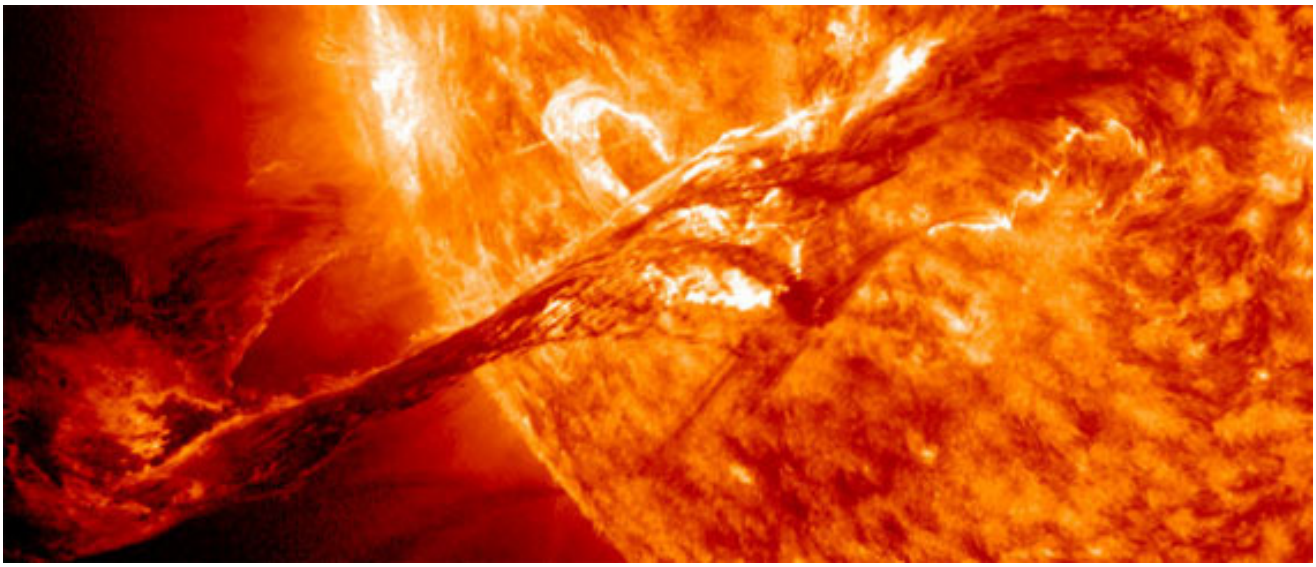

Figure 1.11 On August 31, 2012 a prominence eruption was observed by the Solar Dynamics Observatory at 20:36 UT (Credit: NASA/SDO).

1.5.1 Models for eruptions

Observations suggest that prominence destabilization is in connection with the emergence of twisted magnetic flux (Schrijver, 2009; Mackay et al., 2010). The relation between prominence eruptions and photospheric motions with the change of the magnetic field has been investigated by numerical simulations, modeling as well as observation analysis (Mackay et al., 2010; Magara, 2004; Fan, 2009). Photospheric motions such as the shear and vortical motions can lead to magnetic flux cancellation at the PIL or the formation of sheared magnetic field (Chatterjee and Fan, 2013). They transport magnetic helicity or twist to the corona and cause perturbations in the magnetic field. These perturbations can trigger the loss of the equilibrium and cause the accumulated free energy to release through reconnection (Fan, 2015). An explosive release of the stored magnetic energy can result in the start of PEs, CMEs and flares (Forbes, 2000; Fan, 2015). A possible signature of these shearing and twisting motions is the altitude where the decay index of the potential magnetic field reaches 1.5-1.7 when acceleration takes place (McCauley et al., 2015). The diagram in the right panel of Fig. 1.12 shows the interrelationship between prominence eruptions, flares and CMEs (Kopp and Pneuman, 1976; Shibata, 1998; Forbes, 2000). In the standard model, the current sheet formation and the triggering of magnetic reconnection under the prominence between high sheared field lines lead to the release of the stored energy, resulting in brightening ribbons at the footpoints of the field lines and the eruptions of the coronal plasma, magnetic field and the filamentary material.

There is still the open question of the transition of the prominence from the quasi-equilibrium to the eruption (Fan, 2015). Several different models have been developed to explain the loss of the equilibrium and the triggering of the energy release. Following Fan (2015), the various models can be categorized into two classes: current-aligned (force-free) models with increasing twist, and massive models where gravity no longer counterbalances magnetic pressure. In the first case, flux emergence may be at work and its signature is a magnetic flux rope compatible with the observed PIL. However flux emergence is rather slow and is at odds with the observed fast eruption. This contradiction is removed with two different processes: ideal (kink and torus) instabilities (Démoulin and Priest, 1989; Fan and Gibson, 2003), and reconnection. Considering cylindrically symmetric magnetic flux tubes with both ends tied, the kink instability is initiated when the twist is above a critical value (e.g. 2.49 π according to Hood and Priest, 1981). The torus instability starts when the confinement of magnetic flux rope is not possible (Titov and Démoulin, 1999; Isenberg and Forbes, 2007). It occurs above a critical height of about 15 000 km. In “tether-cutting” models (Moore and Roumeliotis, 1992), reconnection originates underlying the flux rope, followed by the formation of a hot central low-density channel between the flux rope and the vertical current sheet (Fan, 2012). In the “breakout” model, the onset of fast reconnection is the initial trigger, and two current sheets are involved for the onset and acceleration of the CME: break-out current sheet (on top, horizontal) and flare current sheet (at the bottom, vertical) (Antiochos, 1998; Karpen et al., 2012; Kumar et al., 2018).

The combination of the various models can explain most of the observed events. However, the destabilization of the prominence is still not well understood. It is widely accepted that the basic processes responsible for the occurrence of filament eruptions, CMEs and flares are closely related. When prominence eruptions are associated with CMEs, they are often observed as a bright core in white light images and thus can be taken as tracers of the associated CMEs (Sterling and Moore, 2005).

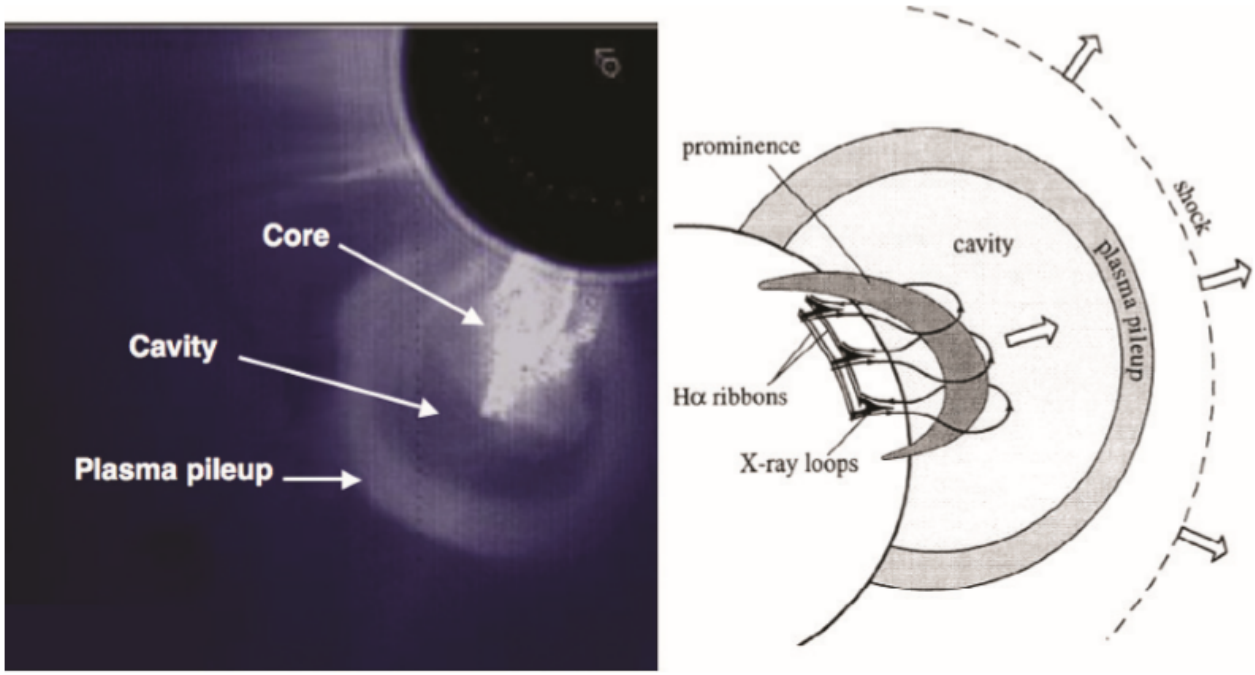

Figure 1.12 Left panel: A white light image of typical CME taken by Solar Maximum Mission (SMM). There are the main features of a CME (van Driel-Gesztelyi et al., 2008). Right panel: Schematic diagram of the CME features (Forbes, 2000).

1.5.2 Observational properties

Before and during the eruption, there are usually a number of observational characteristics, in addition to the ascent of the prominence. Before the eruption, cavities can usually be observed in EUV and white-light and soft X-rays as relatively dark, elliptical regions for prominences. They are taken as the projections of filament channels on the plane of sky (POS). Forland et al. (2013) found that there are eruptions in more than one third of the cavities in their statistical studies. Precursor brightenings in EUV, soft X-rays (SXR), hard X-rays (HXR) and EUV as well as radio burst emission have been reported in previous prominence observations (Sterling and Moore, 2003, 2005). Brightenings in X-ray and EUV are caused by the heating from magnetic reconnection. Coronal HXR sources usually first appear at the top then near the feet of the flaring loops. Loop-top HXR sources have been identified as the reconnection site, and foot point HXR sources are believed as evidence of bremsstrahlung by nonthermal electrons

bombarding the dense chromosphere. Fig. 1.13 shows that the loop-top HXR source rises with the increase of the separation of the ribbons from the PIL (Parenti, 2014). Radio bursts, especially Types II, III and IV are closely associated with prominence eruptions (Webb and Howard, 2012; Parenti, 2014). Type II radio burst is generated by shocks. It usually lasts from a few minutes to several hours. Type III radio bursts often occur at the beginning of flare events, sometimes several hours before the start of the eruption. They are due to nonthermal electron beams propagating along the open magnetic field lines into interplanetary space. Type IV radio bursts are due to synchrotron emission from fast electron beams spiraling in the magnetic field.

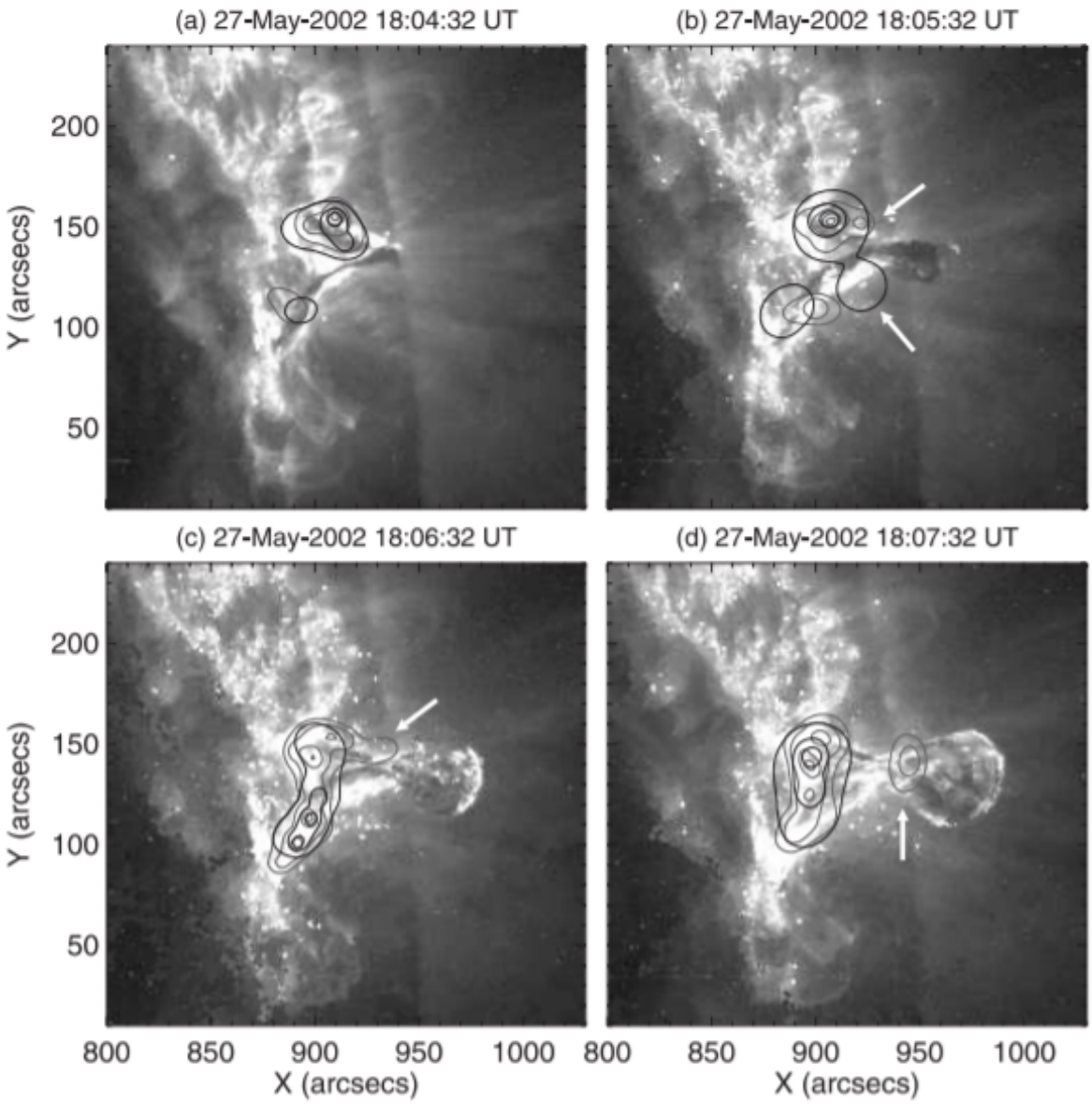

Figure 1.13 RHESSI X-ray contours over plotted on TRACE 195 images. Gray and black contours correspond to the peak intensities of 12-20 keV and 20-40 keV respectively. Coronal sources are marked by white arrows (Liu and Alexander, 2009).

1.6 Spectral Diagnostics

The important physical parameters (e.g., electron temperature, electron density, microturbulent velocity, gas pressure and hydrogen ionization ratio) can be derived from spectral diagnostics. Two approaches are basically used to obtain these quantities. For optically thin plasma, physical parameters can be derived from a direct inversion of the spectra. When the lines become optically thick, non Local Thermodynamic Equilibrium (NLTE) radiative transfer models are required (Labrosse, 2015).

1.6.1 Spectral inversion for optically thin lines

Optically thin plasmas normally produce Gaussian spectral lines. The important plasma parameters (e.g., temperature, pressure, density and ionization degree, etc.) can be derived from the relatively direct inversion of these lines. See more details in Tandberg-Hanssen (1995) and Labrosse et al. (2010).

Temperature and Non-Thermal Velocities

For Gaussian-shaped profiles, line parameters such as the peak intensity I_p, the centroid λ_0 and the width $\Delta\lambda_D$ of the line can be derived following Gaussian fitting procedure, as given by:

$$I_\lambda = I_p\, exp(-(\frac{\lambda - \lambda_0}{\Delta\lambda_D})^2) \tag{1.1}$$

The width of the line mainly consists of the components of thermal broadening and non-thermal broadening. The relation is given by:

$$\Delta\lambda_D = \frac{\lambda_0}{c}\sqrt{\frac{2kT}{m} + \xi^2} \tag{1.2}$$

where m is the ion mass, T is the ion temperature, and ξ is the non-thermal velocity (NTV) component due to turbulence or waves.

Uncertainties can be reduced by analyzing lines from different ions and atoms that have different masses so that the effects of the thermal and non-thermal broadening can be separated (Stellmacher et al., 2003).

Electron Density

Various methods have been used for the computation of the electron density in various prominences, the measured values vary from 10^9 and 10^{11} cm^{-3} (Tandberg-Hanssen, 1995; Labrosse et al., 2010).

Hirayama (1971) derived the electron density in the central part of two quiescent prominences with an upper limit between 1.6 $\times 10^{10}$ and 2.9 $\times 10^{10}$ cm^{-3} from the Stark effect. He used the Stark broadening of hydrogen Balmer series to obtain the electron density. Bommier et al. (1994) measured an electron density between 8.7 $\times 10^{9}$ and 2.1$\times 10^{10}$ cm^{-3} in prominences using the Hanle effect in Hα and He I D_3 lines. Stellmacher et al. (1986) deduced the electron density $n_e \geqslant 2\times 10^{9}$ cm^{-3} for the top of an activated prominence using Thompson scattering in white light. The electron density can also be derived from the raion of line intensities. These lines need to be formed by transitions involving metastable levels. The metastable levels are levels whose de-excitation are sensitive to electron collisions instead of radiation. Assuming that the emitting plasma has a constant temperature, the ratio of density sensitive lines is a function of density so that it can be used to infer the electron density. Previous studies found electron density ranging from 6$\times 10^{8}$ cm^{-3} to 5$\times 10^{11}$ cm^{-3} in quiescent prominences using line ratios in EUV (Labrosse et al., 2010; Parenti, 2015).

For the PCTRs are mostly optically thin and emit in the UV (1000-4000 Å) and EUV (100-1000 Å), the electron density n_e can also be estimated based on the emission measure (EM) computation (Ivanov-Kholodnyi and Nikol'Skii, 1961). Column EM along the LOS is given by:

$$EM = \int {n_e}^2 \, dl \tag{1.3}$$

For each spectral line, all the relevant atomic information are contained in the contribution function *G* (Pottasch, 1963), whose value is collected in atomic database, e.g., the CHIANTI database (Landi et al., 2013). For resonance lines *G* has a slow dependence on electron density and is considered as a peaked function of temperature *G(T)* (Fig. 1.14). It can be approximated as a constant across a small temperature range for optically thin lines. Thus the integrated intensity of a spectra line I_λ can be given by:

$$I_\lambda = \frac{Ab}{4\pi} \langle EM \rangle \langle G(T) \rangle \tag{1.4}$$

Where *Ab* is the fractional element abundance, $\langle G(T) \rangle$ is the averaged contribution function in a temperature interval ΔT, $\langle EM \rangle$ is the averaged column emission measure in the temperature interval ΔT. In this case, EM can be estimated directly from the intensity of a single line (Labrosse et al., 2010).

When there are multi-thermal structures along the LOS, the differential emission measure (DEM) can be used for the diagnostics of the optically thin plasma (Parenti, 2015). The DEM describes the emission measure differential in temperature and is given by:

$$DEM(T) = {n_e}^2 \frac{dl}{dT} \tag{1.5}$$

And the total intensity of a spectral line I_λ can be given by:

$$I_\lambda = \frac{Ab}{4\pi} \int G(T) DEM(T) \, dT \tag{1.6}$$

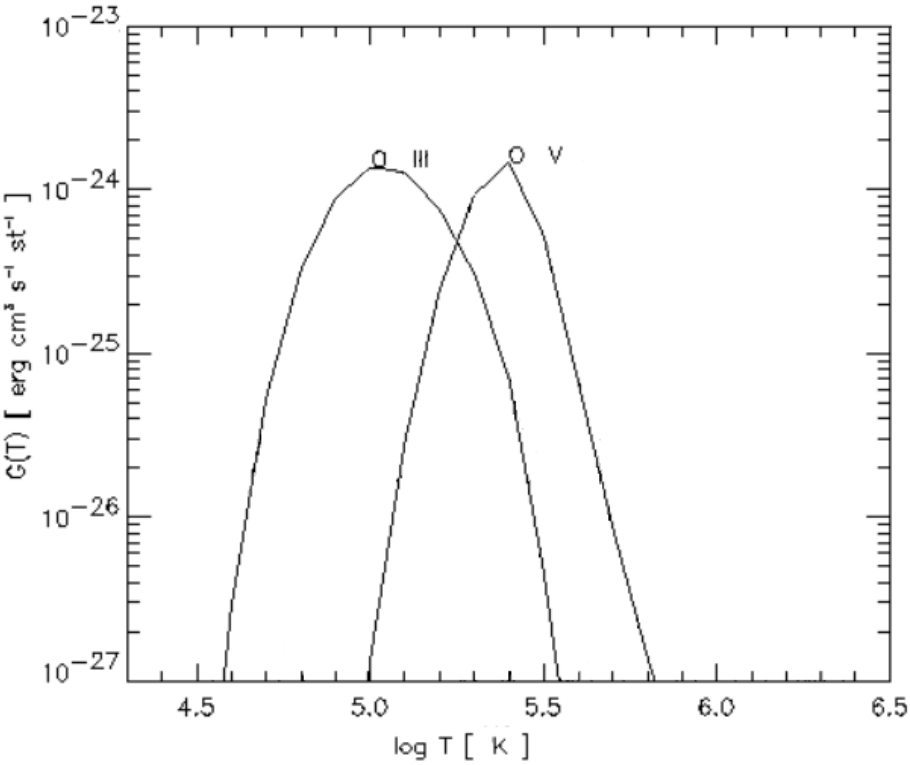

Figure 1.14 Theoretical values of contribution functions for the O III and O IV lines (Del Zanna, 2005).

For the prominence modeling especially for the PCTR, the DEM is very important when there is a large temperature gradient. Parenti and Vial (2007) derived a DEM using spectral lines in prominences from SUMER. They found a strong resemblance between the derived DEM and that of the chromosphere-corona transition region. Chiuderi and Drago (1991) derived the DEM in prominences with UV and radio observations. They found that the angle between the temperature gradient and the magnetic field was a critical factor, and the PCTR thickness varied with the direction of the LOS.

1.6.2 NLTE modeling

For optically thin lines, the physical parameters can be derived from relatively direct inversion of the spectra. When the plasma becomes optically thick, radiative transfer models have to be used. For the plasma in prominences is illuminated and ionized by radiations from the surrounding atmosphere, the local thermodynamic equilibrium (LTE) is not valid in prominence modeling. NLTE modeling becomes necessary and it is a forward method. In the NLTE modeling, the coupled equations of statistical equilibrium, radiative transfer and equation of state need to be solved numerically. The emergent spectra are derived by solving the radiative transfer equation with the determination of the emission and absorption coefficients. The optimum model can be obtained by comparing the derived spectrum with the observed spectrum in an iterative way (Heinzel, 2015).

For prominence NLTE modeling for multilevel atoms, several techniques have been proposed to solve the coupled statistical equilibrium and radiative transfer equations: the Complete Linearization method (CL; Auer and Mihalas, 1969), the Equivalent Two-Level-Atom method (ETLA; Avrett and Loeser, 1987) and the Accelerated Lambda Iteration method (ALI; Rybicki and Hummer, 1991, 1992).

Heasley and co-workers (Heasley and Mihalas, 1976; Heasley and Milkey, 1976, 1983) firstly performed prominence modeling in the form of 1D vertical slabs using a NLTE code based on CL approach. They studied models of solar prominences as isothermal plane-parallel slabs standing vertically above the solar surface, illuminated by the surrounding atmosphere. These 1D codes are proved to be very useful for deriving density, temperature, and other physical quantities.

Heinzel et al. (1987) used detailed incident radiations derived from solar observations in the prominence modeling. They studied the emitted hydrogen spectrum of a 1D isothermal isobaric slab with the use of partial redistribution processes. Later on, Gouttebroze developed another prominence code based on ETLA approach, and one can find references in Gouttebroze and Labrosse (2000). With this code, Gouttebroze et al. (1993, hereafter GHV) built a grid of 140 isotermal and isobaric models and performed a systematic modeling with different pressure, temperature and thickness for hydrogen lines and Lyman continuum. This work and their subsequent modeling (Heinzel et al., 1994, hereafter HGV) not only provided specific signatures but also allowed to derive relations between model parameters and emitted lines and continua. For example, the Hα intensity is proportional to the electron EM, at least for temperatures lower than 15 000 K.

This modeling was not limited to hydrogen but was also extended to other elements such as He I, He II, Ca II, Mg II, etc (Paletou et al., 1993; Labrosse and McGlinchey, 2012; Heinzel et al., 2014). The modeling of hydrogen (and helium) is essential in the prominence modeling for all the elements, because it is necessary to properly treat the ionization and to assign the electron density. In view of the complexity of the geometry of prominences, it was felt necessary to build and use 2D codes (e.g. Vial, 1982b; Paletou et al., 1993) to better describe the boundaries of the structures. Other improvements had been made with grafting a transition region to an isothermal and isobaric layer. The different temperature gradients across and along the magnetic filed lines are taken into account by Heinzel and Anzer (1999) in the magneto-hydrostatic model. They found that the PCTR across the field line is rather thin, while the PCTR along the field line is more extended. But the properties of the PCTR are still not well understood. Another major step was performed with the introduction of Multi-slab models where a layer is replaced by the addition of numerous much smaller layers (Heinzel et al., 2005). The emergent spectrum from all slabs along the LOS is computed with mutual radiative interaction (Zharkova, 1989) or without radiative interaction (Fontenla et al., 1996; Gouttebroze et al., 2002) between the slabs. Such models allow for the comparison with high resolution observations where velocity fields play an important role. However, the results of this modeling

do not contradict the basic 1D modeling. For example, the above-mentioned relation between Hα line intensity and the EM remains valid (Gunár et al., 2011, 2012).

Several non-LTE codes for various types of prominence modeling that are currently used include IAS-code of Gouttebroze, Ondrejov-code of Heinzel, and the code of Paletou (Labrosse et al., 2010).

Chapter 2

Instruments and data analysis techniques

Since the first observations of prominences by Muratori in 1239 (Bhatnagar and Livingston, 2005), major improvements have been made in the instruments. Nowadays there are many sources of data including satellites and Ground-Based observatories. These data can be used in statistical studies of prominences and help understand their general properties. Since 1996 continuous observations have been made by the Extreme ultra-violet Imaging Telescope (EIT) onboard SOHO satellite, which was positioned around the Lagrangian point L1 between the Earth and the Sun. They allow to understand the evolution of prominences during their eruptions. In 2006 two STEREO satellites (STEREO-A and STEREO-B) were launched. They orbit the Sun ahead of and behind the Earth respectively and provide two other viewpoints of the Sun besides the viewpoint at the Earth orbit. In the same year, Hinode mission was launched. The onboard instruments can provide high resolution images of the Sun in Hα and Ca II H line. In 2010 the SDO mission was launched. The imager onboard takes full disk images in different wavelengths and can provide a global prospective of the solar atmosphere. In 2013 the IRIS mission was launched. It provides spectro-imaging in the UV and Near UV with high spatial, temporal and spectral resolution. While the space instruments are limited to small apertures, ground based telescopes have a better spatial resolution. For example the Dutch Open Telescope (DOT) can provide images with a spatial resolution of 0.3". And adaptive optics (AO) are now used in ground based observatories such as Swedish Solar Telescope (SST) and New Solar Telescope (NST) to correct the image distortion from the Earth's atmosphere. In the thesis, we mainly rely on the data from IRIS, SDO/AIA, EUVI/STEREO and Ground-Based COSMO/K-COR. And there is a brief description of these instruments as follows.

2.1 IRIS

The Interface Region Imaging Spectrograph (IRIS) spacecraft was launched on 27 June 2013 (De Pontieu et al., 2014). It orbits the Sun in a Sun-synchronous orbit and can provide solar observations all the year round except when its view of the Sun is blocked by the Earth from

November to January. IRIS has an onboard memory of 48 Gbits and a downlink data rate of 0.7 Mbit/s, allowing more data-intensive observations.

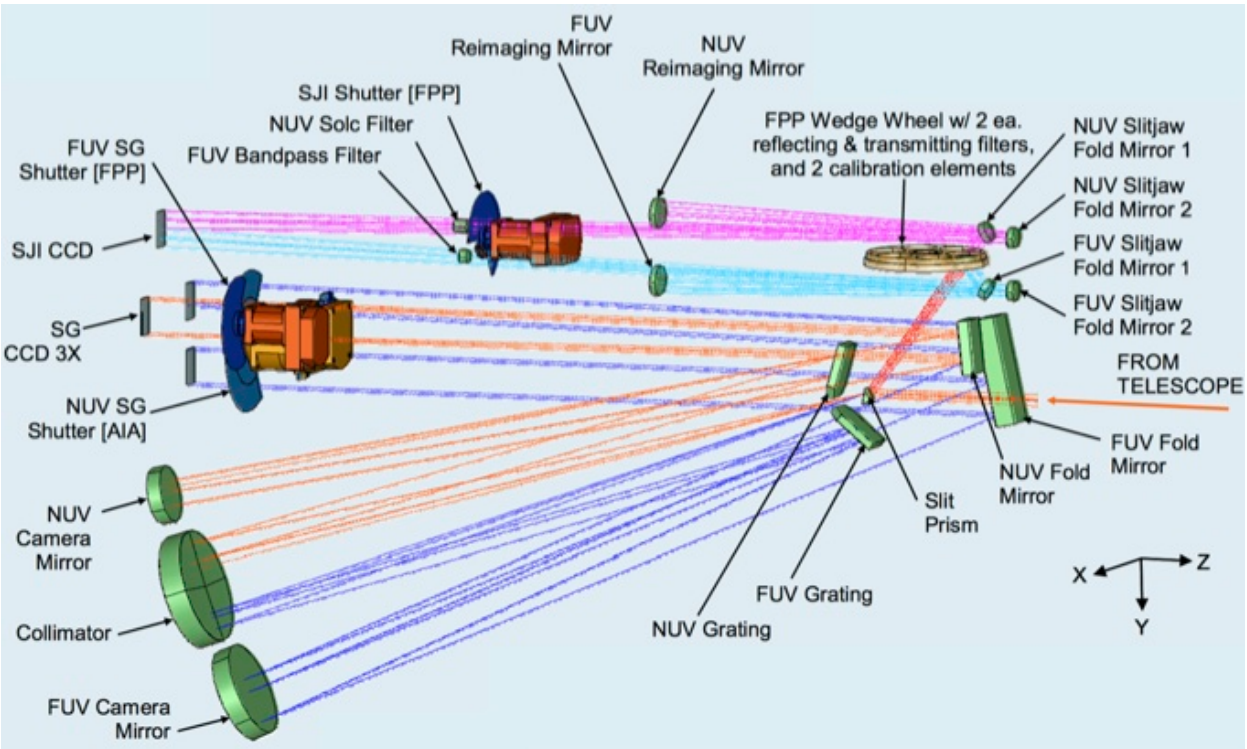

Figure 2.1 Schematic diagram of the light path in the IRIS instrument. The light path of FUV spectrograph is in dark blue, the light path of NUV spectrograph is in orange, the light path of FUV slit-jaw is in light blue and the light path of NUV slit-jaw is in purple (De Pontieu et al., 2014).

The main objective of this mission is to study the transportation of energy and heat from the lower solar atmosphere to the corona through the interface region (the chromosphere and transition region). To achieve these goals, IRIS provides simultaneous spectra and slit-jaw images in various wavelengths, sensitive to the cool and hot plasma in the solar atmosphere. The spectra are taken in two passbands: far ultraviolet (FUV): 1331.56-1406.79 Å and near ultraviolet (NUV): 2782.56 - 2833.89 Å, including the Mg II k and h, Si IV and C II lines (De Pontieu et al., 2014). The images are taken simultaneously with spectral rasters in four different passbands including the Mg II k&h, C II and Si IV lines. The schematic diagram of the light path of the IRIS instrument is shown in Fig. 2.1.

In this diagram, the incident light is first focused on an assembly that is composed of a slit and the surrounding reflective coating. The slit corresponds to a width of 0.33" and a length of 175". In Fig. 2.1, the light paths of the FUV and NUV spectrographs (SG) are shown in dark blue and orange respectively. The light passes through the slit onto a grating, then onto two FUV CCDs and one NUV CCD to record spectra. The light paths of the FUV and NUV slit-jaw (SJI) are shown in light blue and purple respectively. The incident light is first reflected off the

Table 2.1 Key parameters of IRIS (De Pontieu et al., 2014).

Key parameters	
Field of view	175"×175" (SJI)
	0.33"×175" (SG – slit)
	130"×175" (SG – raster)
Spatial scale (pixel)	0.167"
Spatial resolution	0.33" (FUV)
	0.4" (NUV)
Spectral scale (pixel)	12.8 mÅ (FUV)
	25.6 mÅ (NUV)
Spectral resolution	26 mÅ (FUV SG)
	53 mÅ (NUV SG)
Pixel size	0.6"
CCD detectors	2061×1056 pixels
Typical exposure times	0.5 to 30 s

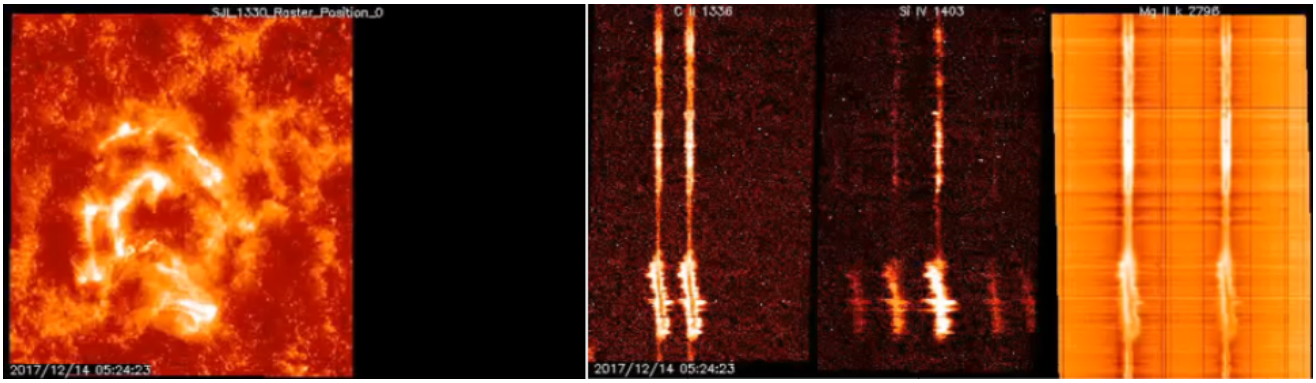

Figure 2.2 IRIS SJI image observed at 05:24 UT on Dec 14 in 1330Å is shown in the left panel. The slit at the center of the image is crossing the flare region at this time, and the corresponding spectra of C II, Si IV and Mg II k lines are shown in the right panel.

reflective coating of the assembly, then is reflected or passes through the filters, and finally is focused onto a CCD to produce images (De Pontieu et al., 2014).

IRIS provides simultaneous spectral rasters and SJI images with a spatial resolution of 0.33" – 0.4", a temporal resolution of 2 seconds and a velocity resolution that can reach 1 km/s over a FOV of 175" × 175". The left panel in Fig. 2.2 shows an IRIS SJI image observed at 05:24 UT on Dec 14 in 1330 Å. The slit is located at the center of the image and the corresponding spectra of theMg II k, C II and Si IV lines are shown in the right panel. Key parameters of IRIS are listed in Table 2.1.

IRIS also allows for flexible rastering schemes. Based on the extremely variable nature of the different targets, there are three main rastering modes: dense raster, sparse raster and fixed slit ("sit-and-stare") modes (ITN[1] 1), as shown in Fig. 2.3. The step size can be equal to or smaller than the width of the slit in the dense raster mode. It is fit for rapid scans of small

[1]http://iris.lmsal.com/documents.html

regions. The sparse raster mode is fit for rapid scans of large regions such as active regions with a step size larger than the slit width. There is no rastering in the fixed slit mode.

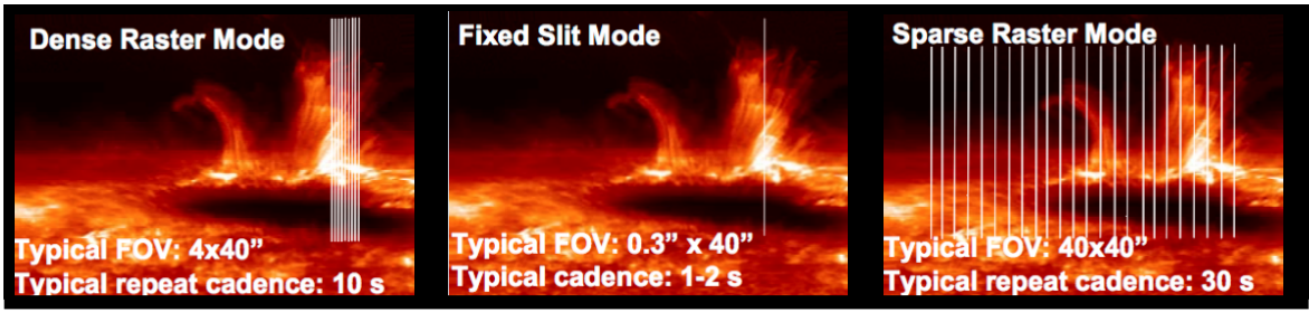

Figure 2.3 Examples of three raster modes of IRIS: dense raster (left), sparse raster (middle) and fixed slit (right) modes. With typical exposure times of 1 s, the cadence and the corresponding FOV are shown in each panel (Credit: ITN 1).

The capabilities of IRIS mission represent remarkable advances over previous instruments. The high temporal and spatial resolution images and simultaneous spectra allow scientists to investigate the highly dynamic solar atmosphere with direct connection between processes observed in the SJI images and spectral features. The IRIS spectral lines in UV provide very useful tools for the investigation of the prominence fine structures. For example, the C II and Si IV lines are sensitive to the temperature of the plasma in the PCTRs. The Mg II lines are usually formed in the cool core of prominences. Using IRIS spectro-imaging observations in these lines, we are able to get a better understanding of the properties, dynamics and evolution of prominences.

2.2 SDO

The Solar Dynamic Observatory (SDO) was launched into a geosynchronous orbit on 11 February 2010 (Pesnell and Chamberlin, 2012). The main objectives of SDO are to study the generation and release of the magnetic energy in the solar atmosphere and to investigate how the solar activities drive variability in the Earth's environment. There are three instruments onboard SDO, including the Heliospheric and Magnetic Imager (HMI), the Atmospheric Imaging Assembly (AIA) and the Extreme Ultraviolet Variability Experiment (EVE) (see Fig. 2.4) (Pesnell and Chamberlin, 2012).

HMI is built to measure the oscillations of the solar photospheric field (Scherrer et al., 2012). It provides high resolution Doppler velocity, LOS magnetic flux and vector magnetic field maps that can be used to figure out what is going on inside and at the surface of the Sun. EVE is built to measure the solar spectral irradiance in the range of 0.1 - 105 nm as well as 121.6 nm with a cadence of 10 seconds and a spectral resolution of 0.1 nm. It allows scientists to study the solar irradiance in EUV and the long term variability. It also helps to understand how and

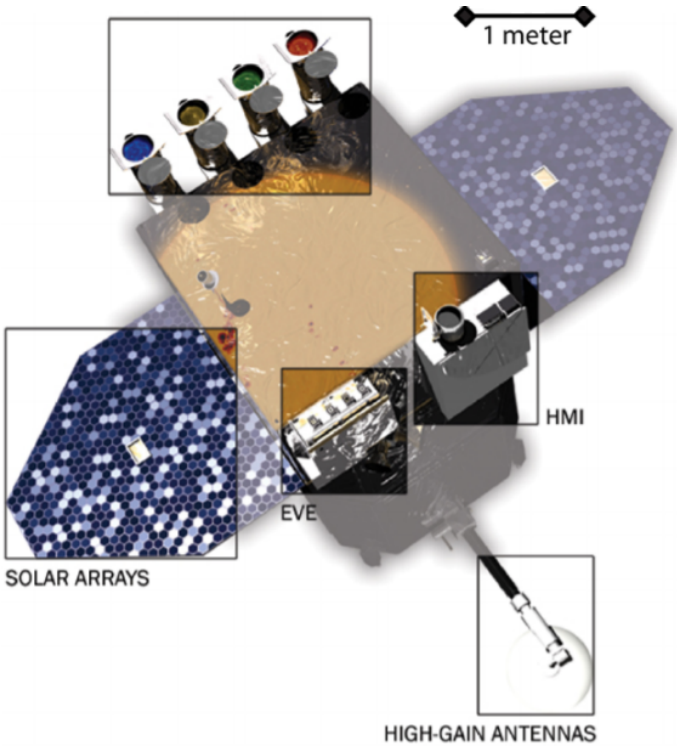

Figure 2.4 The SDO satellite with the three instruments onboard (AIA, HMI and EVE). The high-gain antennas and solar arrays are also highlighted (Pesnell and Chamberlin, 2012).

why the EUV spectral irradiance varies and the response of the geospace environment in order to forecast the geospace disturbances (Woods et al., 2010).

In the thesis, we mainly use the data from AIA, so we give a brief description of AIA.

2.2.1 AIA

The main objectives of AIA are to investigate the evolution of the magnetic environment and to understand the changes of the temperature in the corona (Lemen et al., 2011). It is comprised of four generalized Cassegrain telescopes in order to take images of the transition region and corona in ten different EUV and UV channels: seven in EUV (94 Å Fe XVIII), 131 Å (Fe VIII, XXI), 171 Å (Fe IX), 193 Å (Fe XII, XXIV), 211 Å (Fe XIV), 304 Å (He II) and 335 Å (Fe XVI)), two in UV (near 1600 Å (C IV) and 1700 Å) and one in the visible for the coalignment with other instruments (Lemen et al., 2011). The AIA instrument provides simultaneous high resolution full-disk images with a spatial resolution of 0.6", a temporal resolution of 12 seconds and a field of view (FOV) of 41 arcmin^2 in different channels (Lemen et al., 2011). The high-cadence, full-disk, multi-temperature observations from AIA allow scientists to understand the evolution of structures in the corona with temperatures from 6×10^4 to 2×10^7 K. Critical parameters of this instrument are listed in Table 2.2.

Table 2.2 Critical parameters of AIA onboard SDO (Lemen et al., 2011).

Key parameters	
Field of view	41×41 arcmin
Pixel size	0.6"
CCD detector	4096×4096 pixels
Cadence (Full-frame readout)	10 to 12 s
Typical exposure times	0.5 to 3 s

2.3 STEREO

The Solar TErrestrial RElations Observatory spacecraft (STEREO) was launched on October 26, 2006 (Howard et al., 2008). It consists of two identical spacecraft orbiting around the Sun, one is STEREO Ahead (STEREO-A) and the other is STEREO Behind (STEREO-B). The revolution periods of A and B spacecraft around the Sun are about 18 days shorter and 22 days longer than that of the Earth. Their separation angle between each other increases by about 45° per year. The main goal of the mission is to understand physical properties of the CME phenomenon including the initiation mechanisms and their propagation through the heliosphere in 3-dimensions (3D). These two STEREO spacecraft can provide simultaneous observations from two other different directions than from the Earth (see Fig. 2.5 (Kaiser et al., 2008), it provides the opportunity to study the 3D geometry and evolution of solar structures. In this thesis, we analyze the 3D structure of a prominence by combining the STEREO images with the SDO images taken at the same time using stereoscopic techniques (see Chapter 2.5.2).

The STEREO spacecraft consists of four main instrument packages (Kaiser et al., 2008). In-situ Measurements of Particles and CME Transients (IMPACT) measures the 3D distribution of solar wind plasma and the local magnetic field. STEREO/WAVES (SWAVES) tracks CME-driven shocks from the Sun to the Earth. Sun Earth Coronal and Heliosphere Investigation (SECCHI) tracks the evolution of CMEs from its onset. PLAsma and SupraThermal Ion Composition (PLASTIC) provides the in situ measurements of the particle characteristics. In this thesis, I mainly analyze the data from SECCHI/EUVI, so I give a brief description about EUVI in the following.

2.3.1 SECCHI/EUVI

The Sun-Earth Connection Coronal and Heliospheric Investigation (SECCHI) is a telescope package onboard the STEREO spacecraft (Wülser et al., 2004). Its primary objective is to study CMEs as well as other structures in the solar atmosphere from the center of the disk to beyond 1 AU (Howard et al., 2008). SECCHI is comprised of the following five instruments: two coronagraphs in white light- COR1 that observes the inner corona with a field of view of 1.1 to 3 $R_\odot$ and COR2 that observed the outer corona with a field view of 2 to 15 $R_\odot$ (Thompson et al., 2003), two heliospheric imagers - HI1 and HI2 that are built to study the evolution of

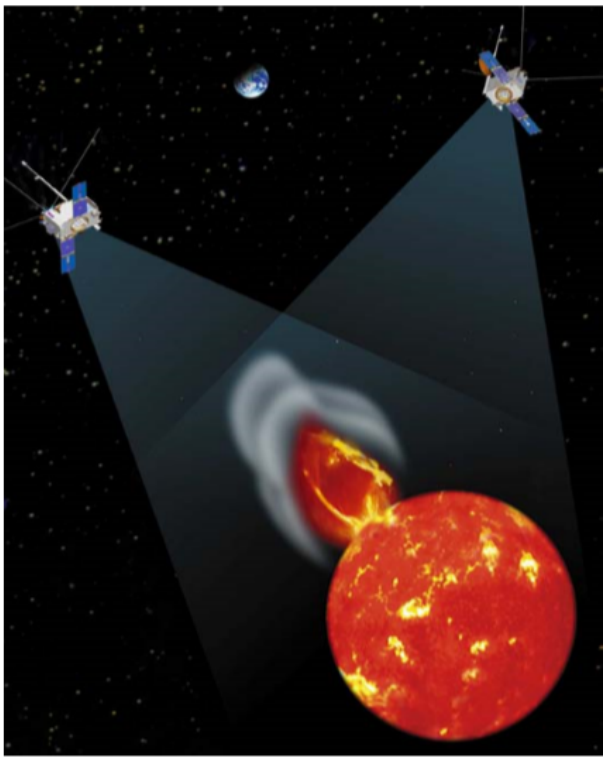

Figure 2.5 In this image the Sun is observed by STEREO A and B spacecraft from two other different directions than from the Earth.

Table 2.3 Critical parameters of EUVI (Howard et al., 2008).

Key parameters	
Wavelengths	He II 304 Å, Fe IX 171 Å, Fe XII 195 Å, Fe XV 284 Å
Field of view	0-1.7$R_\odot$
Pixel size	1.6"
CCD detector	2048×2048 pixels

the solar wind and CMEs in the inner heliosphere, and the Extreme Ultraviolet Imager (EUVI) (Wülser et al., 2004).

The main objective of the twin EUVI telescopes onboard the two STEREO spacecraft are to investigate the solar corona in 3D, especially to understand the initiation and early evolution of CMEs (Wülser et al., 2004). EUVI provides observations of the chromosphere and lower corona at four wavelengths centered at 171 Å, 195 Å, 284 Å and 304 Å that cover a temperature range of 70 000 to 2 MK out to 1.7 $R_\odot$ (Wülser et al., 2004). Key parameters of the EUVI instrument are listed in Table 2.3.

2.4 COSMO

The COronal Solar Magnetism Observatory (COSMO) is a ground-based facility located on a mountaintop in the Hawaiian Islands (Burkepile et al., 2007). COSMO is built to observe

chromospheric and coronal magnetic fields using the Hanle effect and Zeeman effect in scattering polarization. To achieve this goal, the COSMO suite comprises three elements: the main instrument–1.5-m aperture Large Coronagraph (LC) and two additional instruments–chromospheric and prominence magnetometry (ChroMag) and K-coronagraph (K-Cor). LC measures coronal magnetic fields. ChroMag observes the polarization signatures of magnetic fields. In the thesis, I only analyze the data from K-Cor, so we give a brief description of the K-Cor instrument in the following.

2.4.1 K-COR

K-Cor is an internally occulted refractive coronagraph [2]. It is built to understand the initiation, evolution and propagation of CMEs from their onset in the low corona to the heliosphere. Figure 2.6 is a schematic diagram of the K-Cor instrument. The primary objective lens is installed near the front of the K-Cor instrument and illuminated by light from the Sun. The back end of the telescope consists of the occulter, field lens, polarization modulator and imaging assembly. The unwanted light from the disk can be blocked by the occulter and only the polarized light formed by Thompson scattering of the electrons in the corona enters the imaging assembly at the end of the telescope.

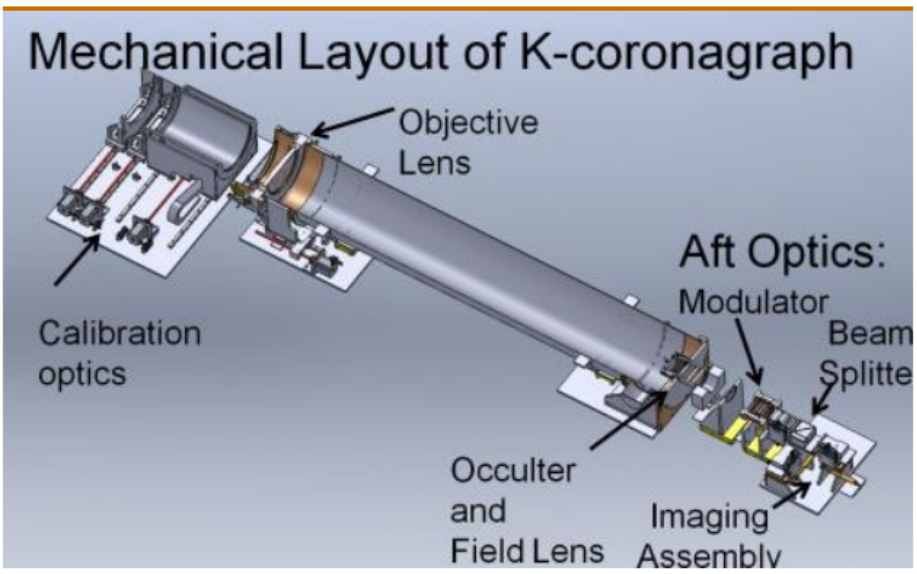

Figure 2.6 Schematic diagram of K-COR [2].

To achieve the science goals, K-Cor is designed to provide unprecedented high time cadence white light images with a FOV of 1.05 to 3 $R_\odot$ and a cadence of 15 seconds. It records the polarization brightness formed by Thomson scattering of the electrons in the corona. Key parameters of the K-Cor instrument are listed in Table 2.4.

[2]https://www2.hao.ucar.edu/mlso/instruments/mlso-kcor-coronagraph

Table 2.4 Key parameters of the K-Cor instrument[2].

About telescope	
	4-state polarization modulation Dual beam polarization
Pass band	∼720 to 750 nm
Field of view	1.05 to 3$R_\odot$
Pixel size	5.5"
Normal cadence	15 s

2.5 Data analysis techniques

In this thesis, we mainly study the properties of the prominences with IRIS spectro-imaging observations and simultaneous observations from SDO/AIA, STEREO/EUVI and K-Cor.

2.5.1 Data archives

IRIS We used the Mg II k&h spectral observations and SJI images obtained simultaneously from IRIS. The IRIS data are available on the webpage of the IRIS mission [3]. Calibration of the IRIS data is described in detail in IRIS Technical Note[4] (ITN) 11. There are five levels of data processing:

Level 0 - Raw spacecraft telemetry.

Level 1.0 - Level 1.0 data are compressed Flexible Image Transport System format (FITS). They have been rotated so that wavelength increases from left to right.

Level 1.5 - Level 1.0 data are calibrated into Level 1.5 by using `IRIS_PREP.pro` in the SolarSoftWare (SSW) package. For the Level 1.5 data, darks and pedestal offsets are removed, flat-field is corrected and cosmic ray spikes that are caused by the effect of high energy particles are removed. Geometric and wavelength corrections are also applied (Wülser et al., 2018).

Levels 2.0 and 3.0 - Level 2 data are derived by assembling rasters of Level 1.5 data. They consist of sets of 3D images stored as (λ,x,y). Level 3 data have a configuration of (x,y,λ,t). This kind of 4D datasets only exist for spectral rasters.

SDO/AIA We used the full disk images in 304 Å from SDO/AIA. They are available from the mission operations center at Joint Science Operations Center (JSOC) of Stanford University. They are redistributed through the Net Data Record Management System (DRMS), of which MEDOC is a node. We have then used the AIA data archived from MEDOC [5]. There are three levels of processing for the AIA data. More details can be found in Boerner et al. (2011).

Level 0 - Raw spacecraft elementary.

[3]http://iris.lmsal.com/data.html
[4]http://iris.lmsal.com/documents.html
[5]http://medoc-sdo.ias.u-psud.fr/

Level 1.0 - For the data belonging to this level, bad pixels are removed, flat-field is corrected and cosmic ray spikes are removed.

Level 1.5 - The data belonging to this level are computed from Level 1.0 data with the use of `aia_PREP.pro` in the SSW package.

STEREO/EUVI We used the full disk images in 304 Å from STEREO/EUVI. The EUVI data are available from the STEREO Science Center [6] and from MEDOC [5]. There are three levels of processing for the EUVI data.

Level 0.5 - Raw spacecraft elementary

Level 1.0 and 2.0 - For the Level 1.0 and 2.0 data, the roll angle is calibrated, bad pixels are removed, and flat-field is corrected by using `SECCHI_PREP.pro` in the SSW package.

K-COR We used the white light images from K-Cor. The K-Cor data are available on the webpage of the HAO observatory [7]. There are three levels of processing for the K-Cor data.

Level 0 - Raw data.

Level 1.0 - Level 1 data contain nearly fully calibrated polarization brightness data. These data are in scientific units - $10^{-6}\ B/B_{sun}$, where B_{sun} is the brightness of the solar disk. The high contrast Level 1.0 data are derived by using the normalized radially-graded filter that can maximize the contrast by subtracting the background (Morgan et al., 2006). The high contrast Level 1.0 data are not in scientific units and are used for identifying the location of coronal structures (e.g. CMEs).

Level 1.5 - Level 1.5 data are fully calibrated polarization brightness intensity in units of B/B_{sun} compared with Level 1.0 data in units of $10^{-6}\ B/B_{sun}$.

2.5.2 3D reconstruction

In order to perform the 3D reconstruction of the prominences, I used `SCC_MEASURE.pro` of the STEREO package of the Solar Software library. This routine was developed by Thompson (2006). It uses a technique called “tiepointing” which uses triangulation to determine the 3D coordinates of the tie point. The tie point is the point at which the LOS from different perspectives to the same solar feature meet. The routine works as a widget based application that allows the user to select with a cursor the same feature in both images from STEREO-A and STEREO-B (Gosain et al., 2009). It is also possible to substitute data from SOHO, SDO or other observatories for one of the STEREO satellites. Once the user selects a point on one image, the corresponding epipolar line is immediately displayed on the other image. The epipolar lines are the projection on both observer’s images of the epipolar plane (Fig. 2.7) which contains the selected point and the two observer positions (Inhester, 2006). The epipolar

[6] https://stereo-ssc.nascom.nasa.gov/

[7] https://www2.hao.ucar.edu/mlso/instruments/mlso-kcor-coronagraph

line on the second image represents the LOS from the first image and constrains the placement of the tiepoint. After the feature is identified in both images of a simultaneous pair according to the emission characteristics, the 3D coordinates are then calculated as Stonyhurst heliographic longitude, latitude, and radial distance from the center of the Sun.

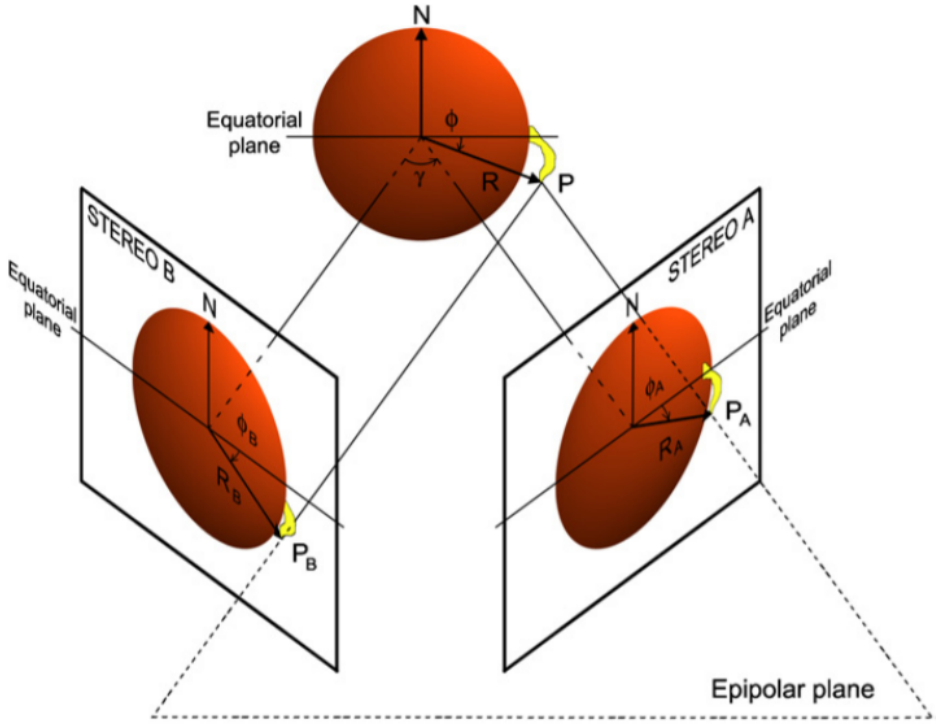

Figure 2.7 Schematic diagram of the geometry of a prominence observed with STEREO A and B. R_A and R_B are projected altitudes, ϕ_A and ϕ_B are latitudes of the point P. γ is the separation angle between STEREO A and B. P, P_A and P_B define the epipolar plane (Bemporad, 2009).

In this thesis work, we performed 3D reconstruction of an erupting prominence with the routine SCC _MEASURE from two pairs of different spacecraft (e.g., STEREO-A and STEREO-B; STEREO-A and SDO). Because the spacecraft are at different distances from the Sun, we first co-center the images from different satellites and scale them to the same size using World Coordinate System (WCS) routines in the Solar Software Tree (Thompson, 2006). Both images are taken at the same time taking into account the STEREO-A 304 Å temporal cadence of 10 minutes to 2 hours in our observations. I used the tiepointing technique to compute the exact coordinates of the prominence features from widely separated vantage points, e.g., observed by STEREO -A and SDO/AIA using He II 304 images, as shown in Fig. 2.8. For each point, this routine is repeated for 10 times and the most optimal one is chosen to ensure the accuracy of the reconstruction. A series of “tiepoints” along the prominence are identified manually in each image to reconstruct an extended object.

It should be noticed that the tiepointing technique relies on the ability to select the same feature in two images from different views. This limiting factor can easily lead to an unknown error in excess of one pixel. The data we used in reconstructing prominences are in He II 304 Å

which is optically thin for much of the corona, and there is an integration effect along the line of sight at each pixel (Gosain et al., 2009). The difficulty to distinguish dark filamentary features from dark patches on disk in 304 Å images makes it impossible to reconstruct the entire length of a filament (Liewer et al., 2009). In this thesis, I only focused on the 3D reconstruction of the prominence above limb. Moreover, the accuracy of this method may also be affected by the projection effect that the same feature may appear different from different views. Liewer et al. (2009) estimated the error of this technique as an error caused by the displacement of a tiepoint on the image. A displacement of one pixel results in an uncertainty in the height as Δh $\approx \Delta$x/sinϕ, where Δx is the error in locating the same feature and ϕ is the separation angle of the spacecraft. During our prominence observations on 28 May 2014, the separation angle between the two STEREO spacecraft is about 36°, the separation angle between STEREO-A and SDO is about 159°. The plate scale of the Sun is about 600 pixels for SECCHI/EUVI images, thus the displacement of one pixel in EUVI images results in an uncertainty in the height (Δh/$R_{\odot}$) of about 0.3% for reconstruction with the image pairs of STEREO A and B and about 0.5% for reconstruction with a pair of STEREO-A and SDO frames.

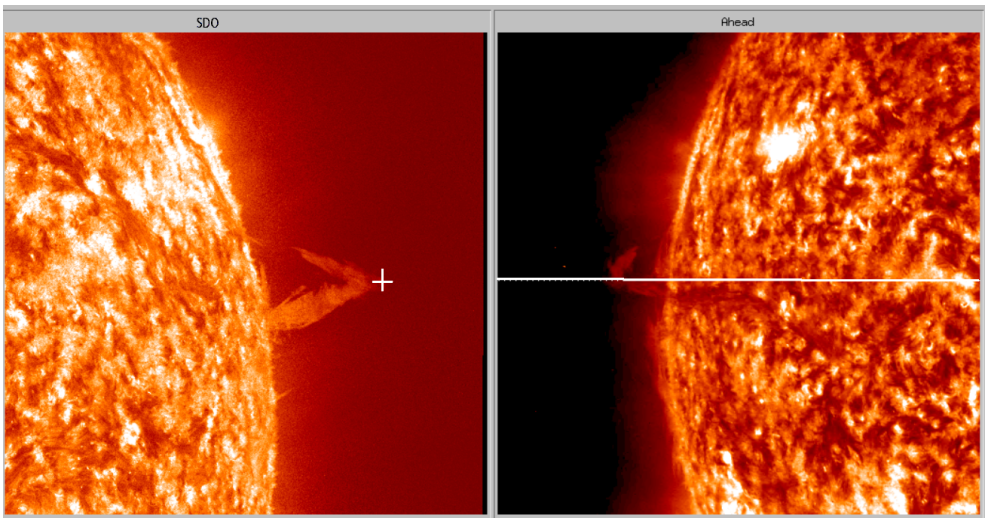

Figure 2.8 A prominence was observed by STEREO-A (left panel) and SDO (right panel) at 16:16 UT on 28 May 2014. The solid line in white in the right panel represents the epipolar line. It corresponds to the top of the prominence marked with '+' in the left panel.

2.5.3 The Radiometric calibration

In this thesis, we used IRIS level 2 data with various calibrations performed, such as the removal of the dark current and the correction of the flat field, as well as the geometric and wavelength calibration (see Chapter 2.5.1). The IRIS level 2 data are in Data Number units (DN). We need to derive the absolute intensity of the Mg II k&h profiles using photometric calibration. However, it is very difficult to perform photometric calibration for Mg II k&h lines because it requires a stable source (Huber, 2013). It is also difficult to measure the in-flight

sensitivity degradation. Considering the importance of deriving the absolute values of the intensity for modeling, for example a factor of 2 in Mg II h and k line intensities can result in a factor of 5 in thickness for low-temperature and pressure models (Heinzel et al., 2014), we performed two calibration procedures to have a better knowledge of the uncertainty of radiometric calibration as in Vial et al. (2016).

First we performed a radiometric calibration using `iris_get_response.pro` (version 4) on all data of the prominence observation and converted them into absolute intensities (e.g. $\mathrm{erg\,s^{-1}\,sr^{-1}\,cm^{-2}\,Å^{-1}}$). This routine is based on the pre-flight calibrations in the laboratory (De Pontieu et al., 2014). Then in-flight verification was performed using cross-calibrations between SOLSTICE and IRIS (Wülser et al., 2018). The in-flight sensitivity degradation of the IRIS NUV spectrograph is shown in Figure 2.9. Colored diamonds indicate the cross-calibrations with SOLSTICE. The curve in green shows how the fitted sensitivity changes with time. The results of this calibration procedure are labeled as IRESP.

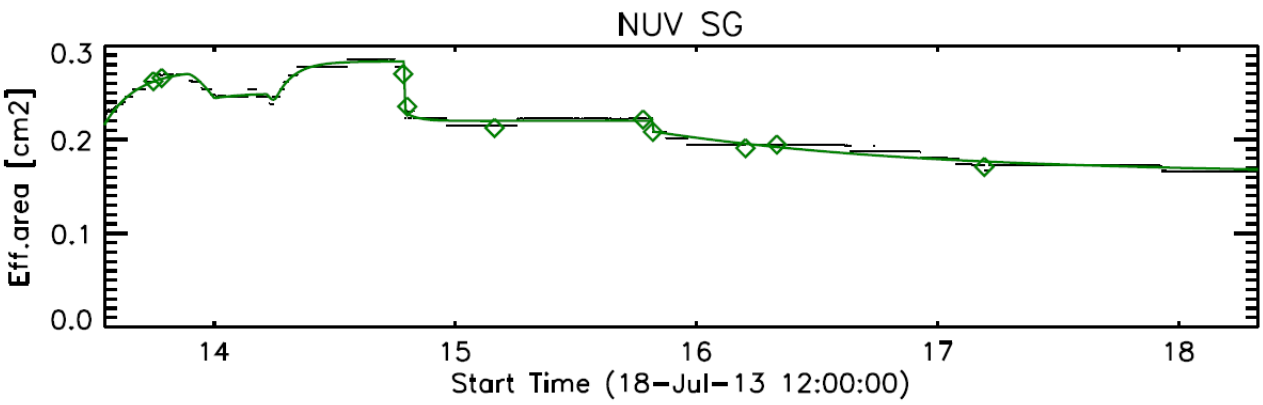

Figure 2.9 The in-flight sensitivity degradation of the IRIS NUV spectrograph. The cross-calibration results between IRIS and SOLSTICE are marked by diamonds. The curve in green shows the fitted sensitivity changes with time (Wülser et al., 2018).

The second procedure uses the quiet Sun as a reliable source for calibration and has been used by Staath and Lemaire (1995) as well as Vial et al. (2016). We compared the integrated intensities (in DN) of the Mg II k and h profiles taken by IRIS on disk and in the prominence with the calibrated k and h total line intensities of Kohl and Parkinson (1976) (see Figure 2.10) at two solar positions (Sun center and $\mu = 0.23$) during a minimum of solar activity.

The disk Mg II profiles are central-reversed with three main components. For the k line, k_3 corresponds to the central reversal, k_{2v} and k_{2r} represent the violet and red emission peaks respectively, and k_{1v} and k_{1r} correspond to the violet and red minima respectively, as shown in the left panel of Fig. 2.12. The components of the h line are similarly named.

We chose to use the IRIS full disk mosaic observations in our calibration [8]. When IRIS is not in eclipse season, once a month, IRIS mosaic observations in 6 spectral windows surrounding the strongest spectral lines (e.g., Mg II k and h, C II 1335 and 1334 Å, and Si IV

[8] https://iris.lmsal.com/mosaic.html

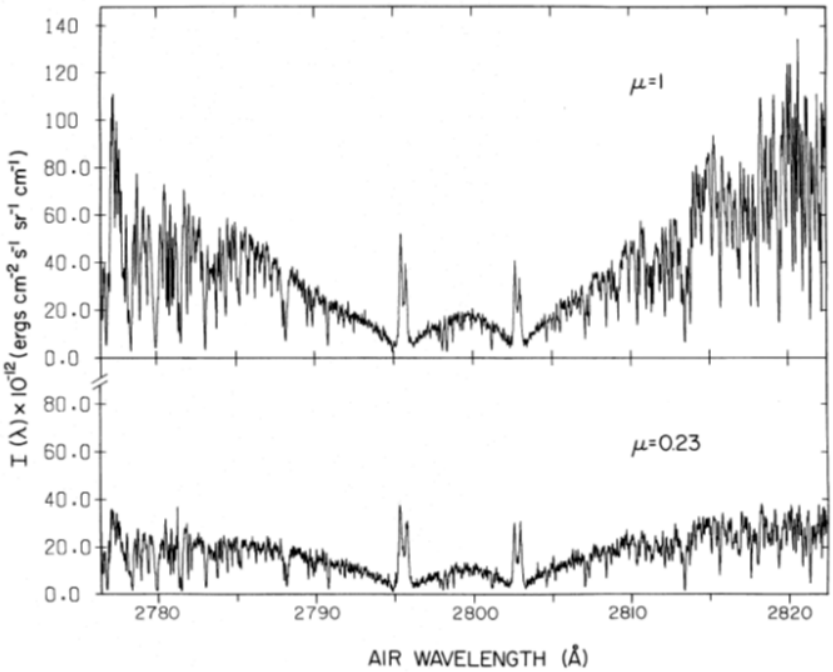

Figure 2.10 Spectra of Mg II k and h lines at disk center and $\mu = 0.23$ (Kohl and Parkinson, 1976).

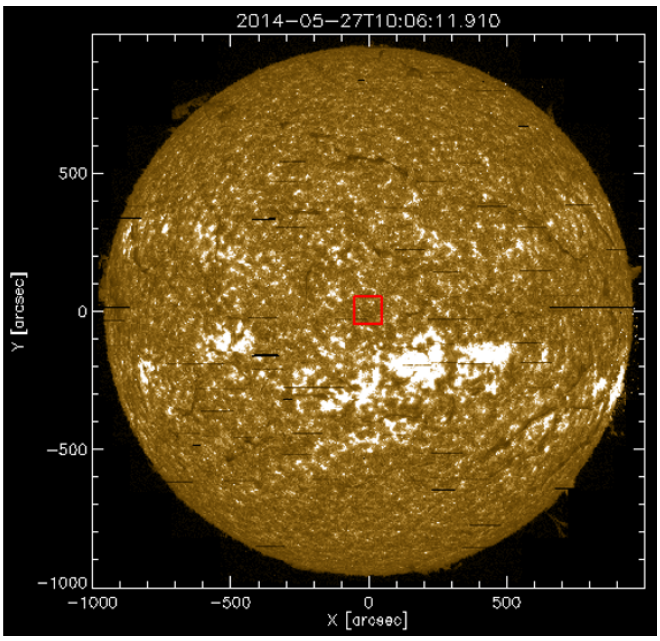

Figure 2.11 IRIS mosaic observation made on May 27, 2014.

1393 and 1403 Å) are built from a series of rasters taken at different pointing locations that cover the full disk. At each pointing, IRIS runs a 64-step raster with a raster step of 2", a FOV of 180"×128" and an exposure time of 1-2 seconds. Our prominence observations (see Chapter 3) took place on 28 May 2014 which was during a (weak) peak of solar cycle 24. We compared the measurements from the mosaic observation on May 27, 2014, which is one day before our observation of the prominence eruption, with those of Kohl and Parkinson (1976). The results from this calibration procedure are labeled as KP. The mosaic full disk image is shown in Figure 2.11. Figure 2.12 shows the averaged Mg II k and h profiles over the region of 100"×100" at the center of the disk which corresponds to the red box in Figure 2.11.

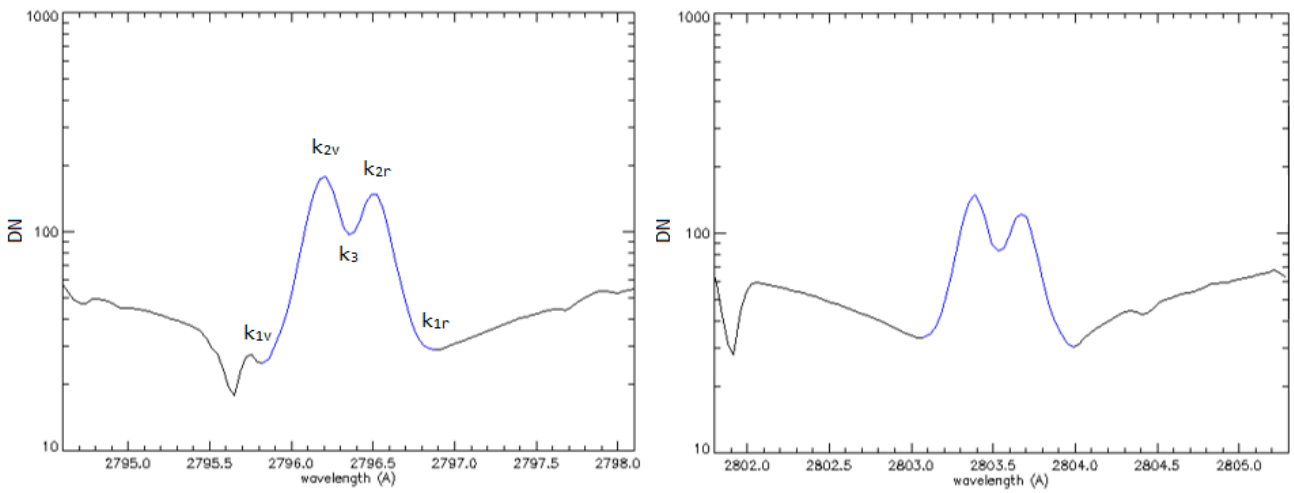

Figure 2.12 Averaged Mg II k (left) and h (right) profiles over a region of 100"×100" at the center of the Sun which corresponds to the region inside the red box in Figure 2.11, with the k_1, k_2 and k_3 components shown in the left panel.

Assuming the Mg II k and h intensities are the same in the quiet Sun at different observing times, a pair of conversion factors were derived for k and h lines by comparing the integrated intensities (in DN) from our mean profiles with values from Kohl and Parkinson's measurements. Then the absolute intensities for k and h lines can be derived from DN.

Fig. 2.14 shows the comparison between the prominence spectra calibrated with both methods (IRESP and KP). The spectra are obtained at the position in red in Fig. 2.13. They show that the IRESP values and the KP values are consistent with each other: The IRESP values are a bit higher than the KP values, but the difference is less than 5% across the whole spectral range. The integrated intensities derived from IRESP values are 3.5×10^4 and 2.5×10^4 erg s^{-1} sr^{-1} cm^{-2} for the Mg II k and h lines respectively. Vial et al. (2016) found in their work that the second method yields calibrated data whose values are on average 28 % higher than the results of the first method. Considering that Kohl and Parkinson' values are accurate to +12 % and -20 % for k_1 and h_1 points, and to ±12 % for other data we used, the IRESP value is within the combined KP and IRIS error bars, with the assumption that there is a $\sqrt{N}$ statistical

uncertainty on IRIS uncalibrated data. In this thesis, we use the calibrated Mg II k and h profiles of the IRESP method.

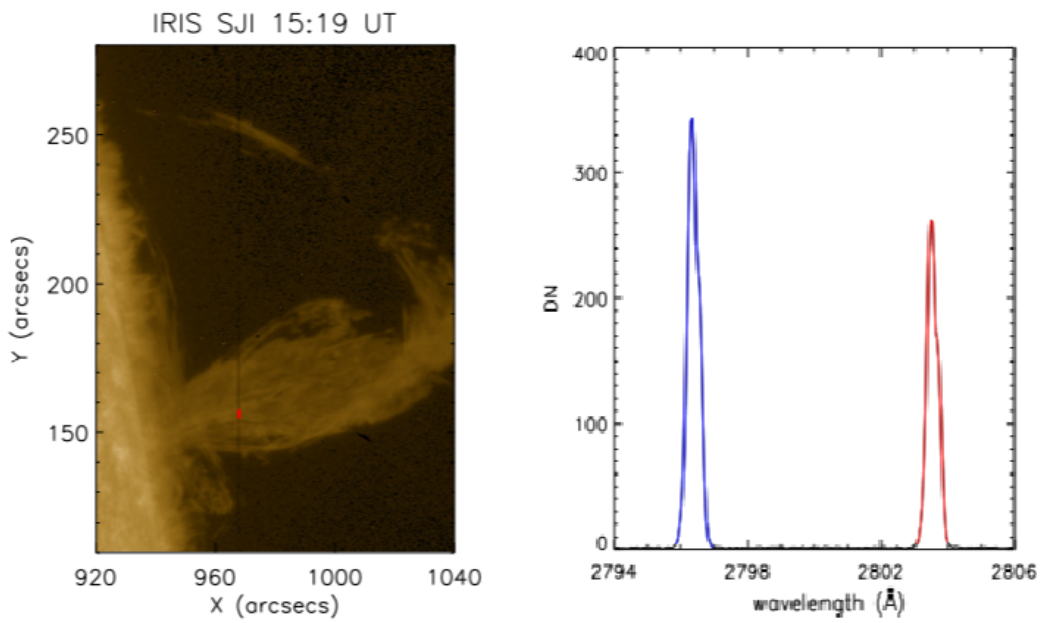

Figure 2.13 (a) IRIS slit-jaw image in 1400 Å, the dark line in the center corresponds to the position of the slit. (b) Mg II k&h spectra observed at the position marked in red on the slit in the SJI image.

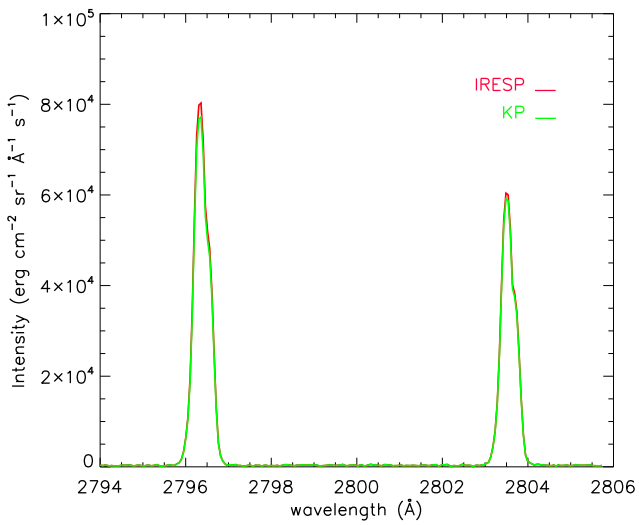

Figure 2.14 Calibrated profiles obtained at the position in red in Fig. 2.13. Red curve: IRESP calibration method. Green curve: calibration method using the quiet-Sun values of Kohl and Parkinson (1976) as references.

Chapter 3

Launch of a CME-associated eruptive prominence as observed with IRIS and ancillary instruments

3.1 Introduction

We analyzed a rather complete set of observations of an eruptive prominence on 28 May 2014 at the West limb, which involves IRIS, SDO, STEREO, SOHO and ground-based observatories (such as K-COR). We give an brief introduction of the used observations from different instruments in Chapter 3.2. Chapter 3.3 details our computation and analysis of the velocity pattern in the prominence. Chapter 3.4 contains the diagnostics of the prominence plasma and the distributions of density and temperature in the prominence. In Chapter 3.5 we present the results of the mass flows in the prominence. Chapter 3.6 contains our conclusion on the analysis of the eruptive prominence.

3.2 Observations

On 28 May 2014, an erupting prominence occurred near the North-West limb of the Sun. Slow rising motions started around 14:00 UT, the prominence eruption started around 18:00 UT, with a leading edge speed of 30 km s^{-1}. During the eruption, there were untwisting motions, and material was ejected upwards and at the same time was observed to return to the Sun. The front of a CME was observed by SOHO/LASCO C2 at 21:36 UT, with a maximum plane-of-sky (POS) velocity of 330 km s^{-1}. No flare was observed around this region during the activation and eruption of the prominence. Table 3.1 shows the summary of observations.

IRIS. IRIS was running very large sparse 64-step rasters with a spatial resolution of 1" perpendicular to the slit, 0.33" along the slit, a temporal resolution of 16.2s and a maximum

Table 3.1 Summary of observations on May 28th 2014.

		Observation time			Radial distance ($R_\odot$)	
Instrument	Data	Start	End	Cadence	Minimum	Maximum
IRIS (SJI)	1400 and 2796 Å	11:24	16:01	32s	0.9	1.18
IRIS (spectrum)	Mg II, C II and Si IV	11:24	16:01	16.2s	0.99	1.09
SDO/AIA	304 Å	11:00	21:00	12s	0	1.3
SoHO/LASCO C2	WL	21:00	22:50	12min	1.5	6
STEREO/SECCHI	304 Å	12:16	21:26	10min-2h	0	1.7
COSMO K-COR	WL	19:22	21:01	15s	1.05	3

FOV of 230"×175". The observation of the prominence started at 11:25 UT and lasted about four and a half hours. It covered the activation of the prominence which started around 14:00 UT. The IRIS slit was oriented almost perpendicular to the central axis of the eruption, and covered the lower portion of the prominence, as shown in the left panel of Figure 3.1. Simultaneous spectra in Mg II k and h lines, C II doublet at 1334 Å and 1336 Å, and Si IV doublet at 1394 and 1403 Å (exposure time 15s) were taken along the slit, seen as a dark line at the center of the SJI images. The signal being weak for the C II and Si IV lines, we computed the average profiles in the region marked in red along the slit in the left panel in Figure 3.1 to have a better signal-to-noise ratio (S/N). The corresponding mean spectra of the Mg II and C II lines are shown in the middle and right panels respectively. Both the profiles of the Mg II and C II lines are single-peaked in this region. The S/N is larger than 100 for the Mg II lines and is larger than 10 for the C II lines. The integrated intensities derived from IRESP values are 3.51×10^4 and 2.50×10^4 erg s^{-1} sr^{-1} cm^{-2} for the Mg II k and h lines and 4.0×10^2 and 5.6×10^2 erg s^{-1} sr^{-1} cm^{-2} for the C II 1334 and 1336 lines. The time variations of the integrated DN of the Mg II (divided by 25.0) and C II lines are shown in Figure 3.2. The correlation coefficients between the Mg II lines are 0.995, between the C II lines are 0.825. The correlation coefficients between the Mg II lines and the C II lines are larger than 0.75 for each combination. These values are similar to those derived by Jejčič et al. (2018) in a quiescent prominence, and indicate that the time variations do not result from the noise.

The signal for the Si IV lines is even weaker than for the C II lines with a S/N less than 5. The C II line at 1336 Å consists of two blended components and the Si iv lines are too noisy, so we mainly focus on the the profiles of Mg II in our analysis.

SDO/AIA. Simultaneous full-disk He II 304 Å observations with 1 min cadence were made by SDO/AIA, together with 6 other EUV spectral channels. The He II 304 Å channel was chosen as being sensitive to the chromosphere and transition region temperatures, thus most representative of the cool prominence plasma. The observed prominence was located at the NW limb and crossed the limb before the activation. The top of the prominence went out of the FOV during the eruption at 19:20 UT. Figure 3.3 shows AIA images observed in He II 304 Å at different times before and during the eruption.

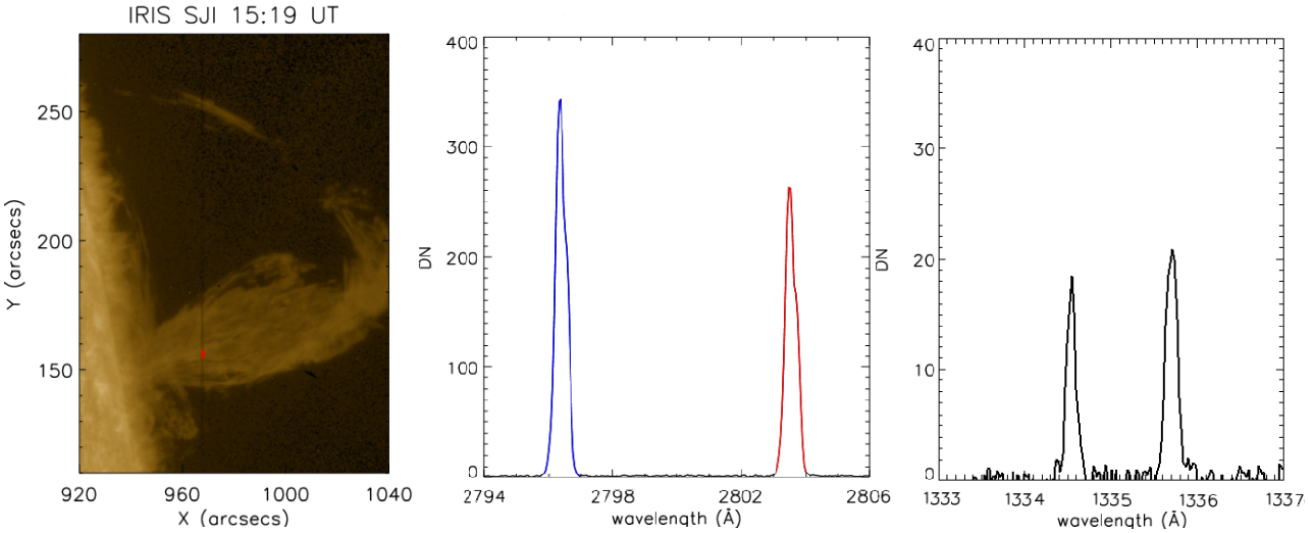

Figure 3.1 The middle and right panels are the spectra of the Mg II and C II lines respectively averaged over the region marked in red along the slit in the left panel observed at 15:19 UT.

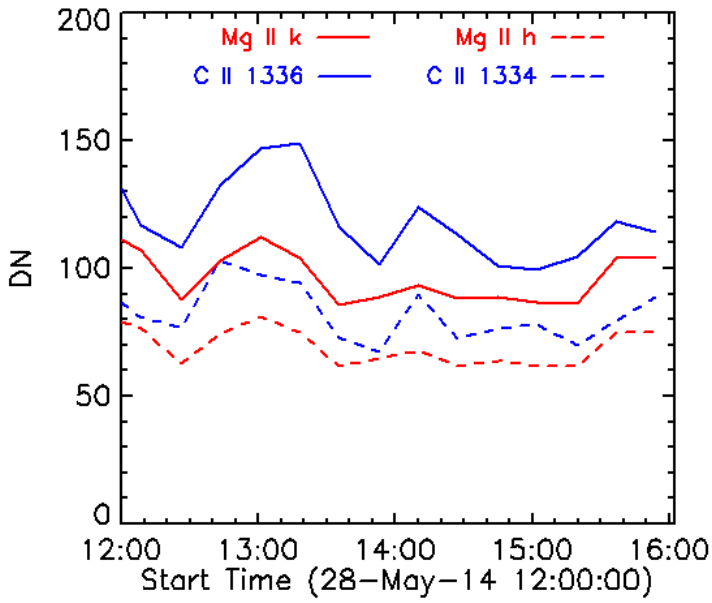

Figure 3.2 The time variations of the integrated DN of the Mg II (divided by 25.0) and C II lines.

PROBA2/SWAP. When the top of the prominence goes beyond the SDO/AIA FOV at 19:20 UT, its hotter counterpart remains visible in emission for about an hour in the 171 Å channel of PROBA2/SWAP (Seaton et al., 2013).

STEREO/SECCHI. We also analyzed images from the EUVI onboard STEREO A and B spacecraft. The observations in He II 304 Å are derived with a cadence of 10 min to 2 hr. On 28 May 2014, the separation angles with Earth were 164.7°and -159.2 °for STEREO A and B spacecraft respectively (see Figure 3.4), thus they provide observations of the prominence from different viewpoints, as shown in Figure 3.5.

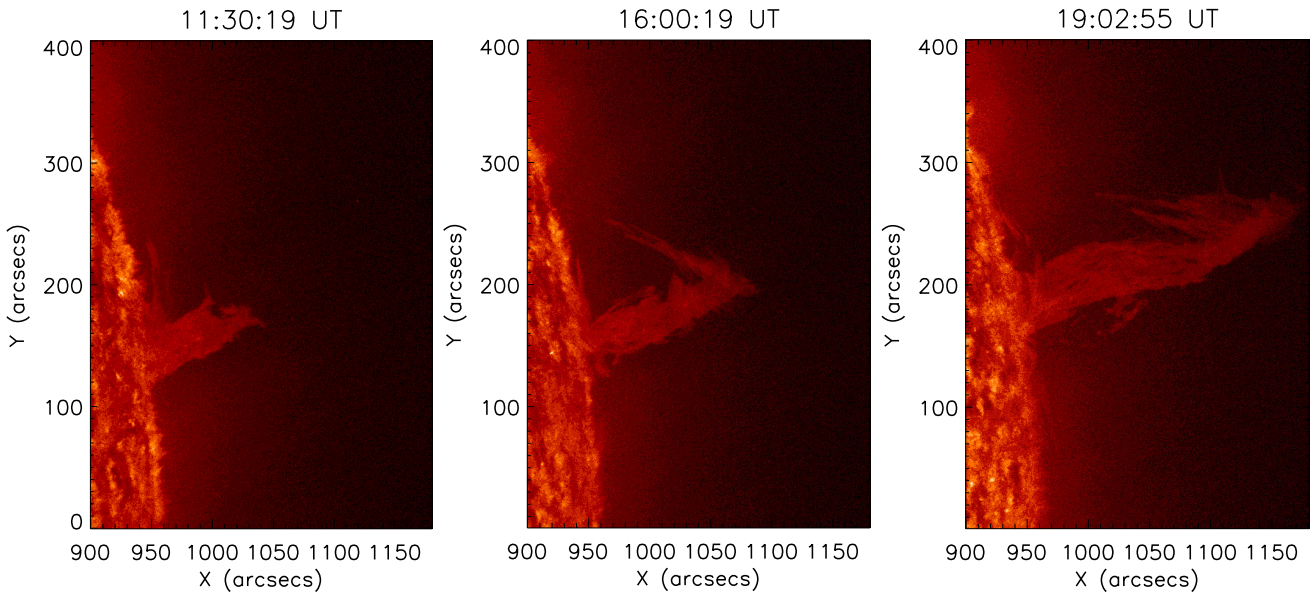

Figure 3.3 Images obtained by SDO/AIA in the He II 304 Å line at different times before (left) and during the prominence eruption (middle, right).

COSMO/K-COR. We also analyzed ground-based observations from the K-Cor. The prominence and subsequent CME was observed by K-Cor between 17:14 and 21:18 UT with a spatial resolution of 5.5" and a cadence of 15 s. For identifying the location of coronal structures, high contrast data (see Chapter 2.5.1) were derived by Joan Burkepile who applied a normalized radially graded filter (Morgan et al., 2009, adapted by S. Fineschi and S. Gibson for K-Cor), as shown in Fig. 3.6. In this way we can track the twisted prominence while it moves outward. And a narrow cavity was observed after 19:40 UT, as shown in Fig. 3.6b.

SoHO/LASCO. We also obtained observations from the Large Angle and Spectrometric Coronagraph (LASCO)/C2 onboard SoHO. The FOV extends from 2 to 6 $R_\odot$ (Brueckner et al., 1995). The front of a CME was detected by LASCO C2 from 28 May 21:36 UT to 29 May 01:25 UT (Fig. 3.7), and the maximum velocity of the CME reached 332 km s^{-1} according to the CACTus[1] catalog (Robbrecht et al., 2009).

3.3 Data analysis

3.3.1 Prominence morphology and geometry evolution

This filament is part of the remnant of active regions AR 12017 and AR 12018 (see Figure 3.9). It had been visible nearly throughout the disk passage of the active regions, which were in their decaying stage, and it disappeared on the other side of the Sun based on STEREO A and B observations. The observed prominence was close to disk center on May 21. Figure 3.10

[1] http://sidc.oma.be/cactus/catalog/LASCO/2_5_0/2014/05/CME0163/CME.html

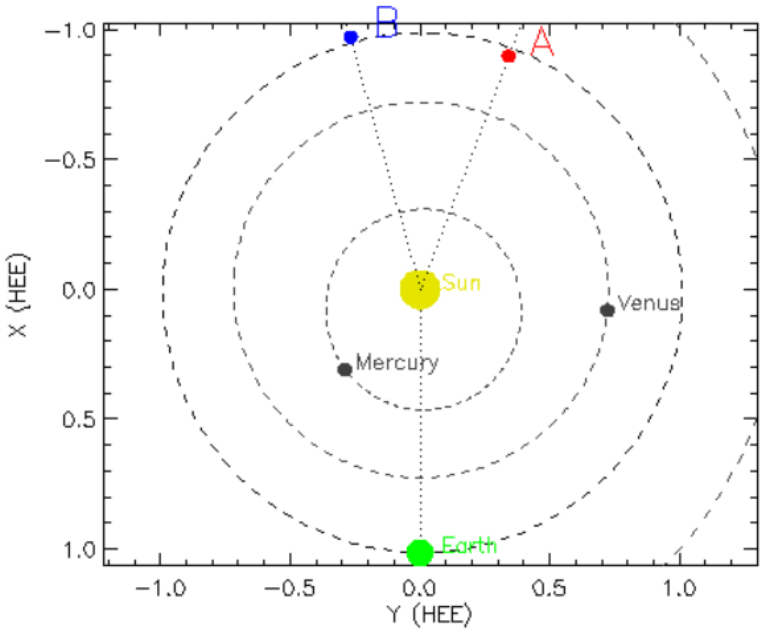

Figure 3.4 The positions of the Sun, Earth and STEREO-A/B satellites for 2014-05-28 16:00 UT.

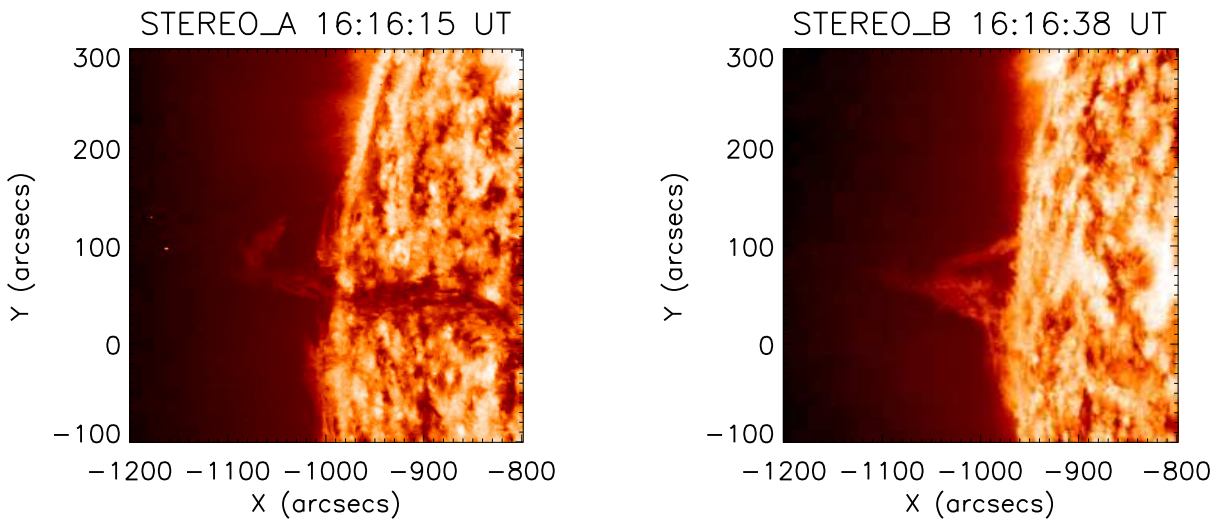

Figure 3.5 Images obtained by the EUVI instrument on board STEREO A at 16:16:15 UT (a) and STEREO B at 16:16:38 UT (b) in the He II 304 Å channel.

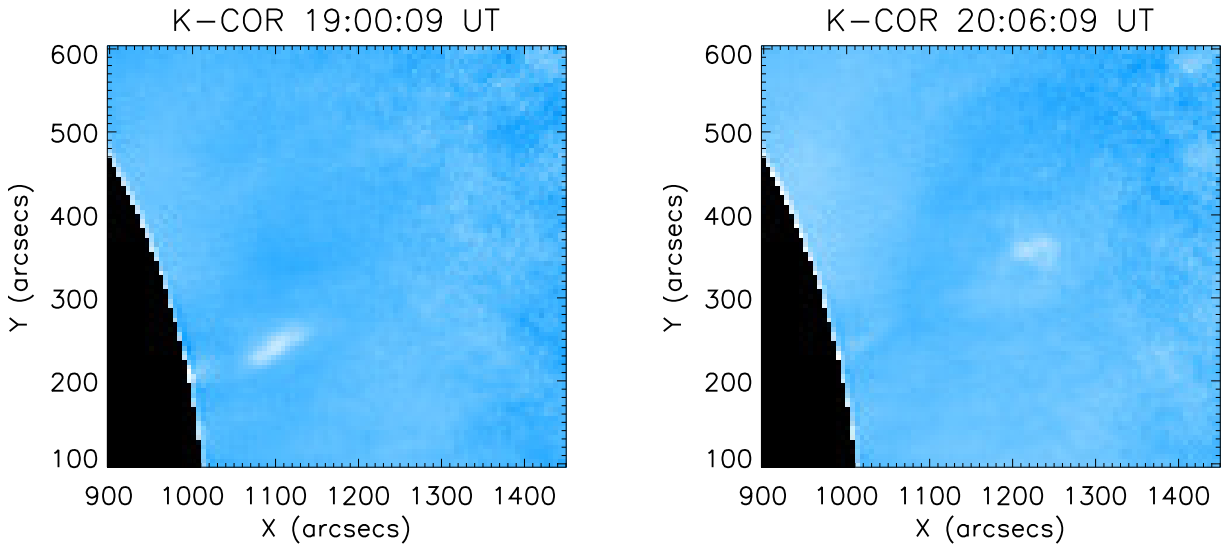

Figure 3.6 High contrast images taken by K-COR at 19:00 UT (a) and 20:06 UT (b) on May 28 2014, provided courtesy of J. Burkepile.

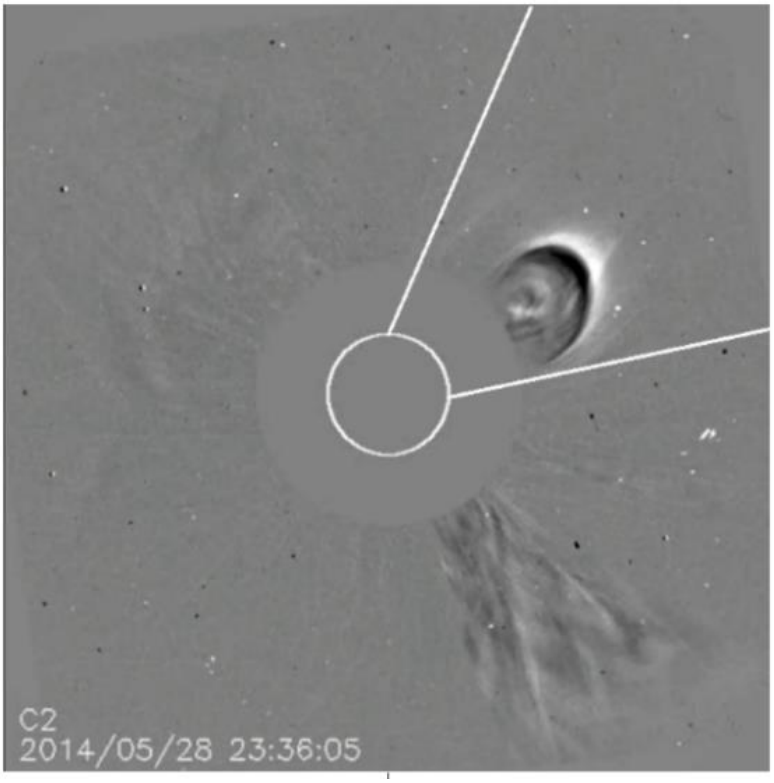

Figure 3.7 SOHO LASCO C2 difference image from the CACTus database at 23:36 UT, showing the CME as it is ejected into space.

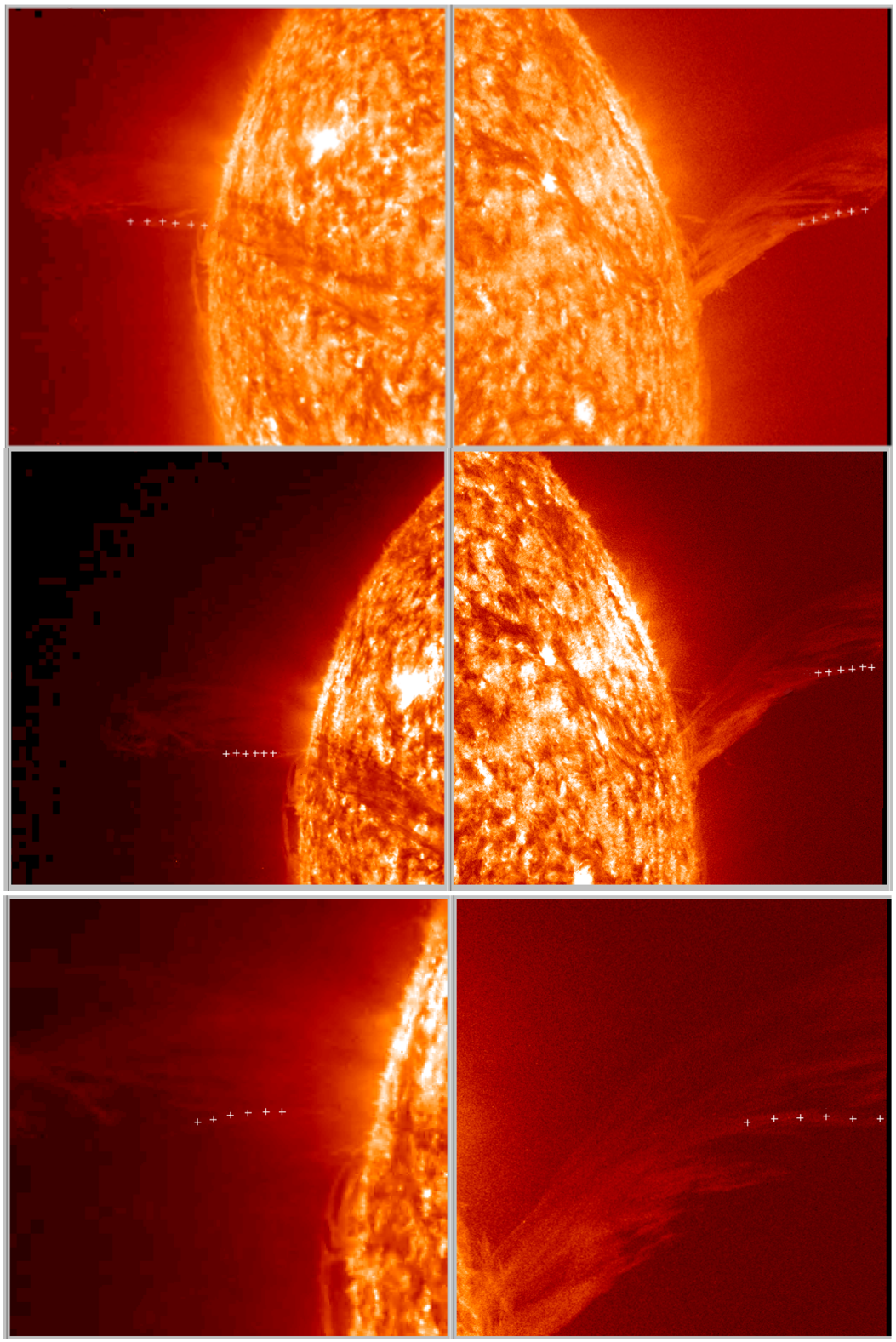

Figure 3.8 The STEREO-A image (left of each panel) and SDO image (right of panel) show the prominence observed at 20:06 UT (top), 20:16 UT (middle) and 20:26 UT (bottom) in different FOV. The feature tracked is marked with '+' sign on all the images.

shows the prominence observed in Hα (Fig. 3.10a) and He II 304 Å (Fig. 3.10b). Because it has a larger opacity in 304 Å than in Hα, it has a more extended S-shape in 304 Å, and the main direction was along parallels of solar latitude in the central part. Then the prominence rotated towards the NW limb and crossed the limb several days before the onset of the eruption. Since we roughly see the prominence "head-on" before the eruption, it is difficult to distinguish its small-scale structures, such as plumes, blobs and cavities. During the activation and eruption of the prominence, there is material falling down from the top of the prominence as shown in Fig. 3.3, probably along the magnetic field lines considering the low speeds and low heights of such material. The observed downflows are first at South of the main part, then at North of the main part; this could be a projection effect of the S structure at the limb. In the AIA movie of the eruption, we see an apparent anticlockwise untwisting motion of the filament body from 18:30 UT until around 21:00 UT. At the same time, the eruption appears to propagate inclined by 9 to 20° from the radial direction toward North. The inclination makes it difficult to discern rotational motions based on images from only a single viewpoint.

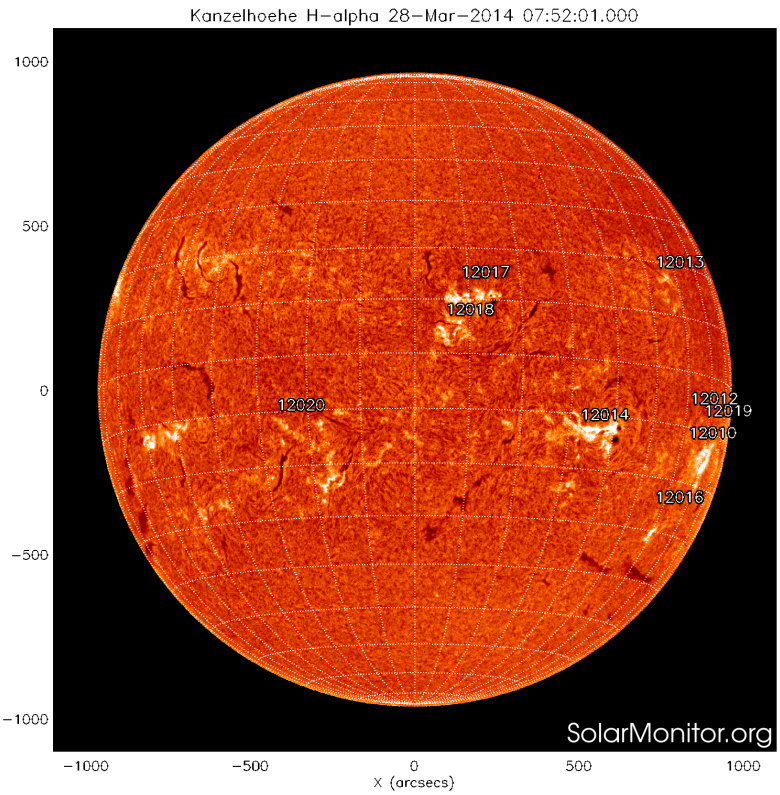

Figure 3.9 Full disk Hα image on 28 March 2014 taken by GONG.

EUVI onboard STEREO A and B spacecraft provide observations of the prominence from different viewpoints, as shown in Fig. 3.5. Using the 3D reconstruction method mentioned in Chapter 2.5.2, we reconstructed the 3D coordinates of the prominence. Considering the difficulty in identifying the corresponding features, we performed 3D reconstruction multiple times with both STEREO A and AIA image pairs and STEREO A and B image pairs to get a better understanding of the uncertainty. Figure 3.11 shows the derived prominence spine

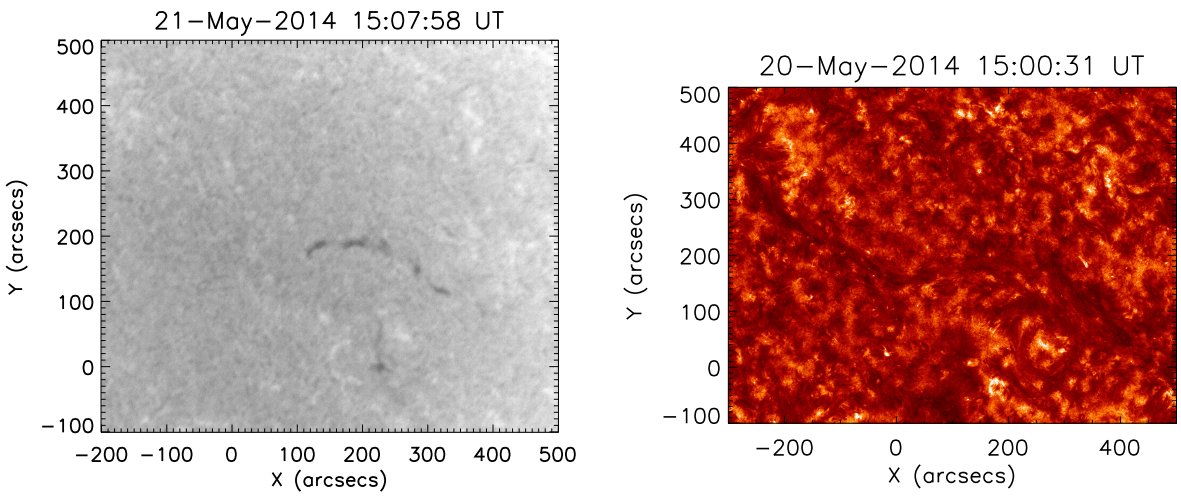

Figure 3.10 (a) Hα image of the filament on 21 May 2014 taken by Big Bear Solar Observatory (BBSO). (b) He II 304 Å image of the filament on 21 May 2014 taken by SDO/AIA.

viewed from above (left panel) and the side (right panel). The results from the STEREO A and AIA image pair (in red) and the STEREO A and B image pair (in green) are generally consistent. It is difficult to compute the systematic uncertainties for this 3D reconstruction. Depending on the size and the sharpness of the prominence observed in 304 Å, it is reasonable to take a displacement of the tiepoints less than 10 pixel, which will lead to uncertainty of 5% on height (see Chapter 2.5.2).

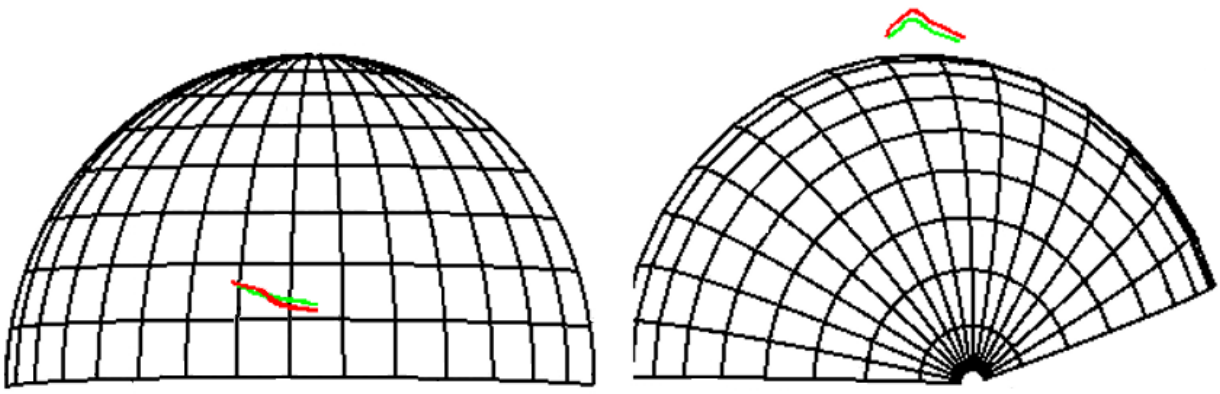

Figure 3.11 3D reconstruction with STEREO A and AIA image pairs (in red) and STEREO A and B image pairs (in green).

The 3D geometry of the prominence derived from the STEREO A and B image pair at 16:16 UT is shown in red in Figure 3.12. A and B correspond to the main body and the falling part of the prominence shown in the AIA image. The top of the prominence is marked with '+' sign and the semicircular plane in gray represents the POS. We find that the main body of the prominence is behind the limb seen from the Earth, as evidenced by Fig. 3.5. The top of the prominence is close to the POS (Stonyhurst longitude 90.3° West, and latitude 10.5° North). The inclination angle between the prominence axis and the POS is around 60° close to the top

of the prominence at 16:16 UT. The separation angle between the two STEREO spacecraft was 36° at this time, but the cadence of the observations especially for STEREO B (2 hours) is insufficient to follow the eruption in 3D.

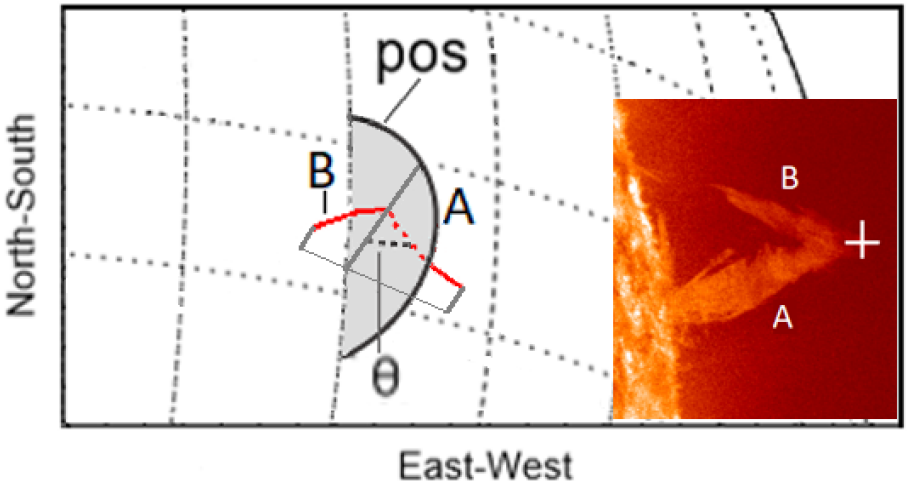

Figure 3.12 The 3D geometry of the prominence at 16:16 UT is shown in red. A and B correspond to the main body and the falling part of the prominence shown in the AIA image. The top of the prominence is marked with '+' sign and the semicircular plane in gray represents the POS.

According to the 3D reconstruction results from the image pair of SDO and STEREO A at 16:16 UT, the top of the prominence is close to the POS (Stonyhurst longitude 90° West, and latitude 10.5° North, see Fig. 3.13). It is the same as the results derived from STEREO A and B observations. The falling part from the top of the prominence is in front of the POS, and the Stonyhurst longitude and latitude at the bottom (marked with '+' in Fig. 3.13) are 80.3° West and 13.5° North respectively.

The separation between SDO and STEREO-A was 159° at this time. Co-identification of features in both views is quite difficult with such a large separation. However, it is possible to determine several identical features in pairs of simultaneous images during the eruption. Figure 3.14 shows the tracked features marked in white as seen in 304 Å of SDO/AIA. The plots in Fig. 3.15 show the Stonyhurst heliographic longitudes and latitudes of the feature tracked at each time step, as derived from SDO and STEREO A. Indices 1 and 6 correspond respectively to the top and bottom of the feature. The tracked feature evolved around Stonyhurst longitude 100° West, and 15° North. The primary alignment of the 20:06 UT plot is along parallels of constant latitude, west to east from bottom to top. However, in the later plots the tracked feature distinctly inclines towards higher latitude. The plot at 20:16 displays a slope of 15°, and the plot at 20:26 UT displays a slope of 120° in Fig. 3.15. An anticlockwise rotation in this plot (corresponding to an anticlockwise rotation of the structure as seen from above) can be perceived from 20:06 to 20:26 UT. We also tracked the threads falling from the top of the prominence by this method, and the radius of a bunch of threads is about 5000 km if the threads are assumed to be cylindrical.

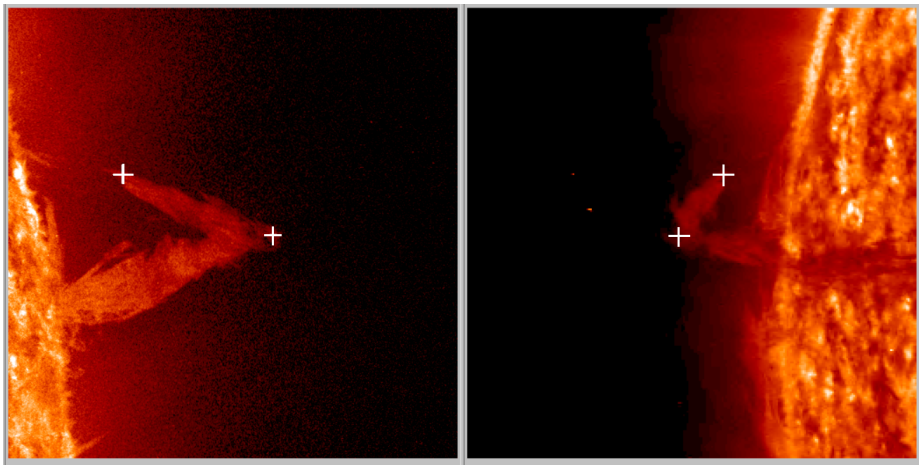

Figure 3.13 The SDO (left panel) and STEREO-A images (right panel) show the prominence observed at 16:16 UT. The top of the prominence and the bottom of the falling parts are marked with '+' sign on the two images.

3.3.2 Velocities in the prominence

Velocity of the top of the prominence

The prominence heights above the solar surface are tracked as the position of the top along the main axis of the prominence. Take the sketch in Fig. 3.16 as an example. The black line represents the position of the limb, the green, blue and yellow lines show the outline of the prominence during the eruption. The '+' in red shows the top of the prominence we track in our analysis. Figure 3.17 shows how the prominence heights observed in the IRIS SJIs, AIA images and K-COR images change with time. The time evolution of the height begins with prominence activation, then follows an eruption with acceleration. The prominence activation begins around 14:00 UT, when it is observed by IRIS and AIA. The heights of the top tracked in AIA and IRIS images are consistent with each other at the same time. Then the top of the prominence moves out of IRIS FOV at 15:26 UT, and IRIS observation stopped around 16: UT. The activation phase duration is about 4 hours with an average slow-rise velocity of $\sim 3.2\,\mathrm{km\,s^{-1}}$. McCauley et al. (2015) derived similar results (an average activation phase duration of about 4.4 hours and an average slow-rise velocity of $\sim 4.1\,\mathrm{km\,s^{-1}}$ for Intermediate Prominences) in their quantitative study of different types of PEs. The eruption acceleration begins around 18:00 UT when a sudden increase occurs in the height. The top of the prominence reaches the FOV boundary of AIA around 19:10 UT. Afterwards it is continuously tracked in K-COR images in white light, although this doesn't necessarily correspond to the same features as seen in the 304 Å channel. We can track the top of the prominence in K-COR images until around 21:00 UT, when the top of the prominence is too diffuse to track. The acceleration phase can be fitted with an exponential function (shown in green in Figure 3.17), and the rise of the top reaches a velocity of $42\,\mathrm{km\,s^{-1}}$ at 21:00 UT. The front of a CME is detected by LASCO C2 around 21:30 UT, it

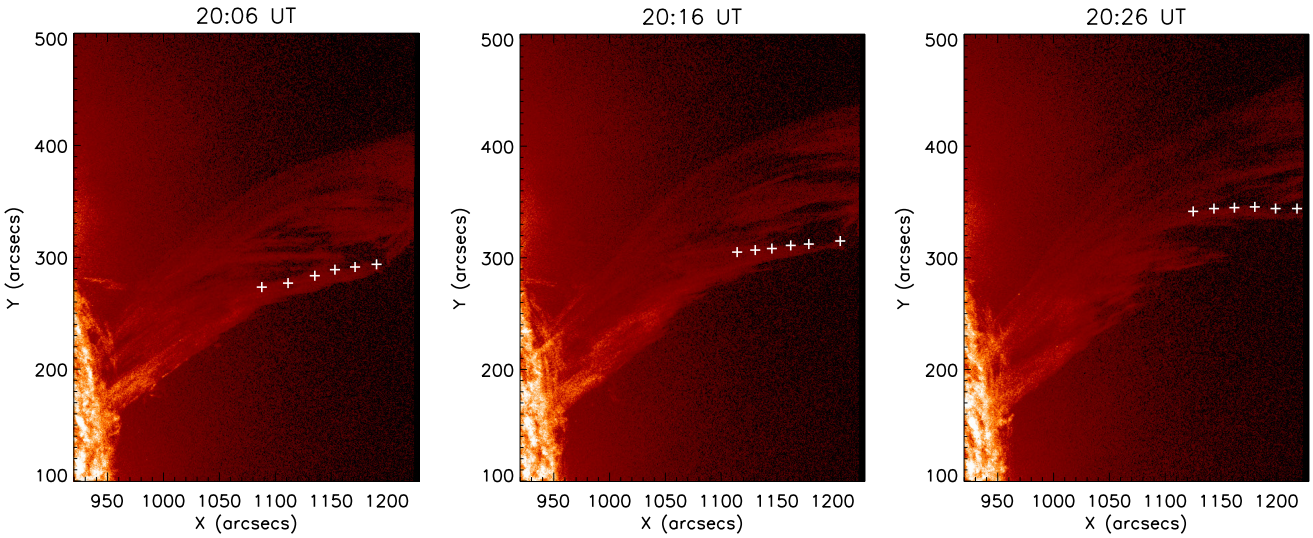

Figure 3.14 Prominence observed by AIA in the He II 304 Å channel at 20:06 (left), 20:16 (middle) and 20:26 UT (right). The '+' symbols indicate the features tracked at different times and matched to features seen with STEREO A.

crosses the FOV of C2 and reaches the maximum velocity of 332 km s^{-1} at 01:25 UT on May 29.

Plane of sky velocities

We obtained the velocities in the plane of sky (POS) by using the Farnebäck (2003) optical flow algorithm provided by the OpenCV library (Bradski, 2000) through its Python interface. The results of this code are affected by the choice of the different parameters as follows.

- pyr_scale: This parameter defines the image scale (<1) of the pyramids. For a chosen image, the corresponding pyramid is comprised of different layers. We use pyr_scale=0.5 in our computation. It specifies that for each layer in the pyramid the preceding one is twice larger than the following one.

- levels: This parameter defines the number of the layers in the pyramid. When it is set to be 1, there is only the initial image included in the pyramid without extra layers. We use levels=4 in our computation.

- winsize: This parameter specifies the averaged size of the window. Choosing a larger value of the winsize can alleviate the effect of the noise and improve the robustness of the velocity computation especially when there are motions with large velocities. But it should be noted that the larger value of the winsize is chosen, the more blurred motion

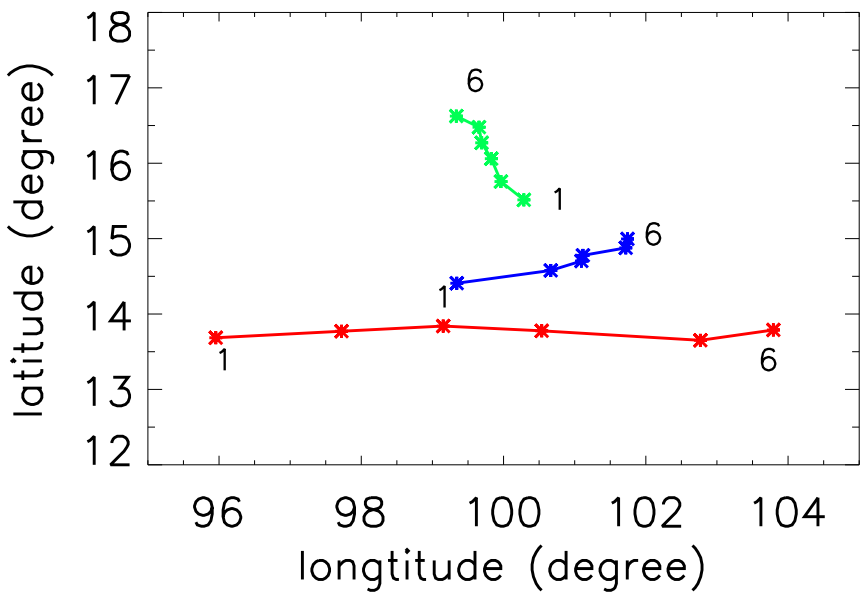

Figure 3.15 Stonyhurst heliographic longitudes and latitudes of the feature tracked at 20:06 (red), 20:16 (blue) and 20:26 UT (green). Indices 1 and 6 correspond respectively to the top and bottom of the feature in Fig. 3.14.

field is derived. We use winsize=20 in our computation.

- iterations: This parameter defines the number of iterations in the computation of each layer of the pyramid. We use iterations=4 in our computation.

- poly_n: This parameter defines the size of the neighborhood pixel that is used for the detection of polynomial expansion. When a larger item is chosen, a smoother surface will be used for the approximation of the image, thus improving the robustness of the algorithm and increasing the blurriness in the velocity field. Typical values of this parameter are 5 or 7. We use ploy_n=7 in our computation.

- poly_sigma: This item specifies the standard deviation of the Gaussian. It is used for smoothing the derivatives that are basic for the polynomial expansion [2]. Typical values are 1.1 for poly_n=5 and 1.5 for poly_n=7. We use poly_sigma=1.5 in our computation.

[2]https://kyamagu.github.io/mexopencv/matlab/calcOpticalFlowFarneback.html

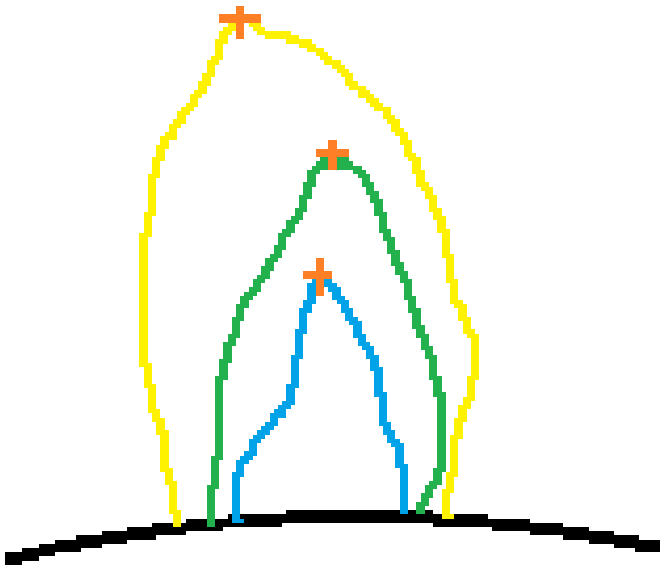

Figure 3.16 The black line in the sketch represents the position of the limb, the green, blue and yellow lines show the outline of a prominence during the eruption. The '+' in red shows the top of the prominence we track in our analysis.

The algorithm assumes a slowly varying displacement field and it may cause discontinuities if the variations are sharp. Consequently some smoothing is necessary and consequently it is difficult to detect velocities at small spatial scales.

Figure 3.18 shows the POS velocity streamlines (right of each panel) derived by applying the optical flow algorithm on AIA images (left of each panel) at 15:17 (top) and 19:34 UT (bottom) respectively. At 15:17 UT, downward motions with a velocity smaller than 5 km s^{-1} are generally observed in the lower part of the prominence, while in the upper part of the prominence upward motions are derived with a velocity in the order of 8 to 15 km s^{-1}. At 19:34 UT horizontal motions parallel to the solar surface towards high latitude are observed in the body of the prominence with a velocity between 5 and 10 km s^{-1}. They indicate that the prominence propagates inclined from the radial direction toward higher latitudes. The velocities of the prominence top at 15:17 and 19:34 UT are in the order of 5 to 20 km s^{-1}. They are consistent with the results of prominence top tracking (Chapter 3.3.2).

We also apply the optical flow algorithm on IRIS SJI images. In Figure 3.19, the right panel shows the POS velocity streamlines derived from IRIS image pairs between 15:16:57 UT and 15:17:30 UT, and the left panel shows the POS velocity streamlines in the same FOV derived from AIA image pairs between 15:16:43 UT and 15:17:43 UT. We find that the velocity patterns in the two panels are generally consistent with each other in the prominence, except that in some regions the velocity in the right panel are several km s^{-1} larger than the velocity in the left panel. Away from the prominence body, in the region around 950" in x direction and 180" in y direction, we find motions parallel to the limb with a velocity around 10 km s^{-1} in the right panel,

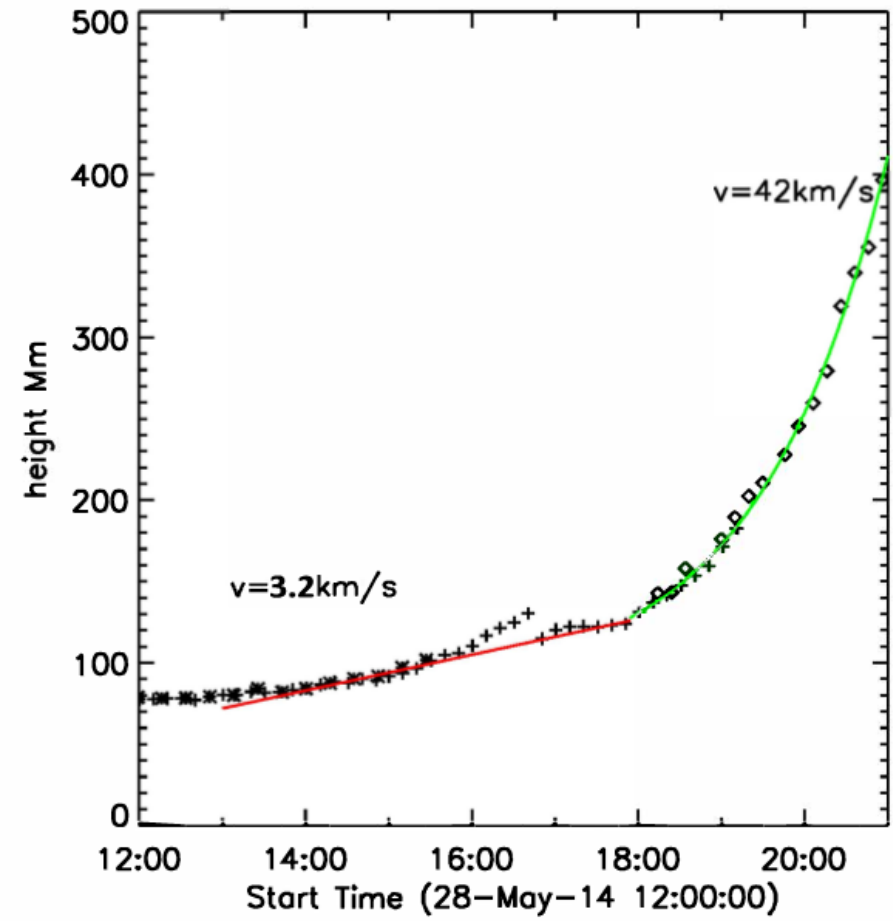

Figure 3.17 Altitude of the top of the prominence tracked in IRIS (∗), SDO/AIA (+) and K-COR (⋄).

while in the left panel there are motions in different directions with a velocity less than 5 km s^{-1}. This may be caused by the difference between the characteristic emission temperatures of the He II 304 Å and Mg II k&h lines and the moving features are consequently more visible in IRIS images than in AIA images.

Doppler velocities

Mg II line profiles. The spatially-resolved spectra of Mg II k&h lines show a wide range of profiles in the prominence, as shown in Figure 3.20. The profiles of the Mg II k&h lines from the main body of the prominence are mainly non-reversed (see Figure 3.20a), while in the lower part of the prominence there are reversed profiles with distinct red and blue peaks (see Fig. 3.20bcd). In the prominence, we also find profiles which have more than two peaks (see Figure 3.20ef), that indicate a combination of different structures moving with different velocities along the LOS. Based on the main characteristics of the profiles, we divide the profiles from the prominence into 3 groups: A) single-peaked profiles, B) central-reversed profiles, and C) complex profiles that may have more than two peaks, or that have two peaks and the distance

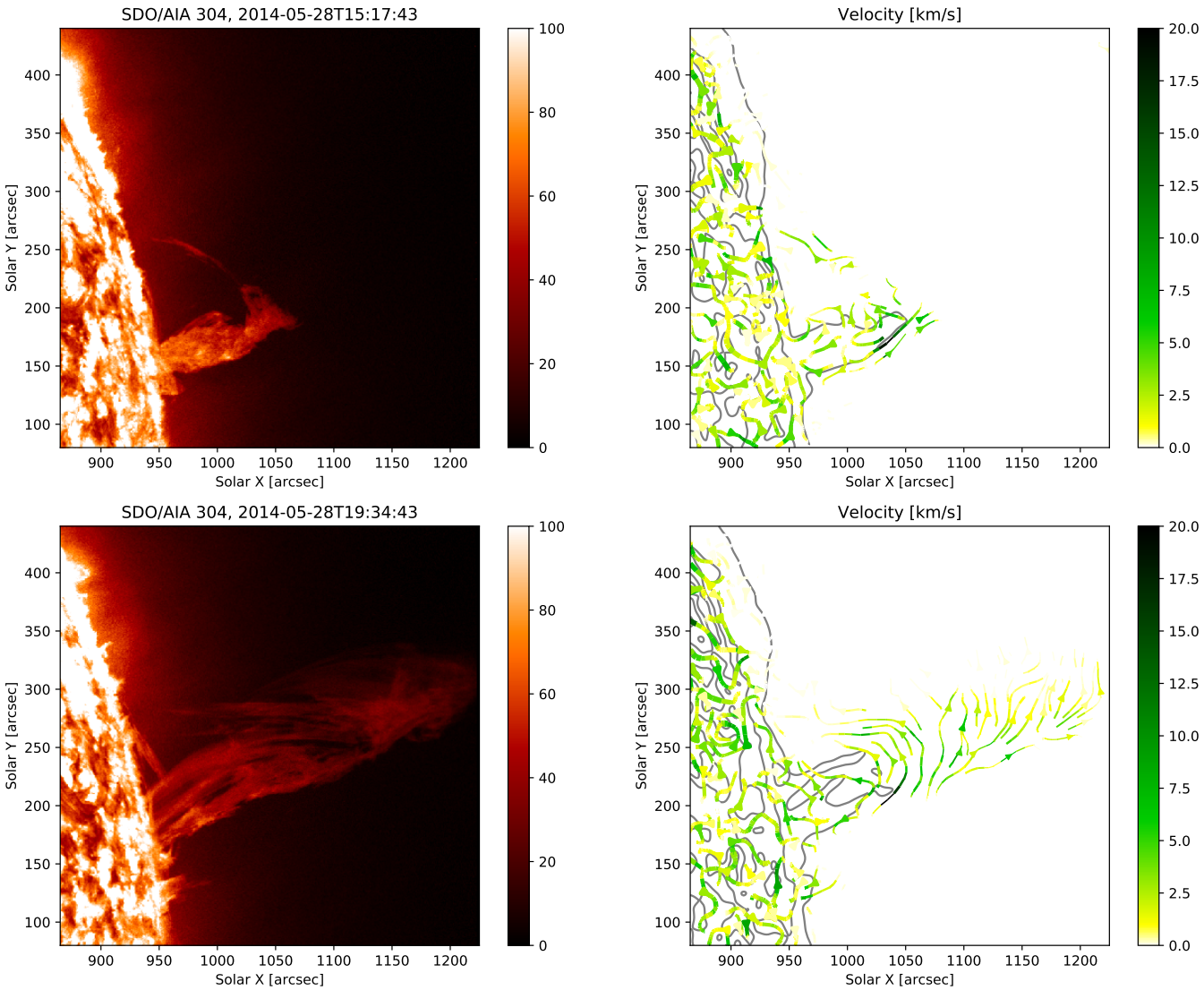

Figure 3.18 POS velocity (right of each panel) derived from AIA image pairs (left: first image of each pair) using the Farnebäck optical flow algorithm at 15:17 (a) and 19:34 UT (b). The color indicates the value of velocity, the arrows indicate its direction, and the thickness is related to the observed intensity in AIA.

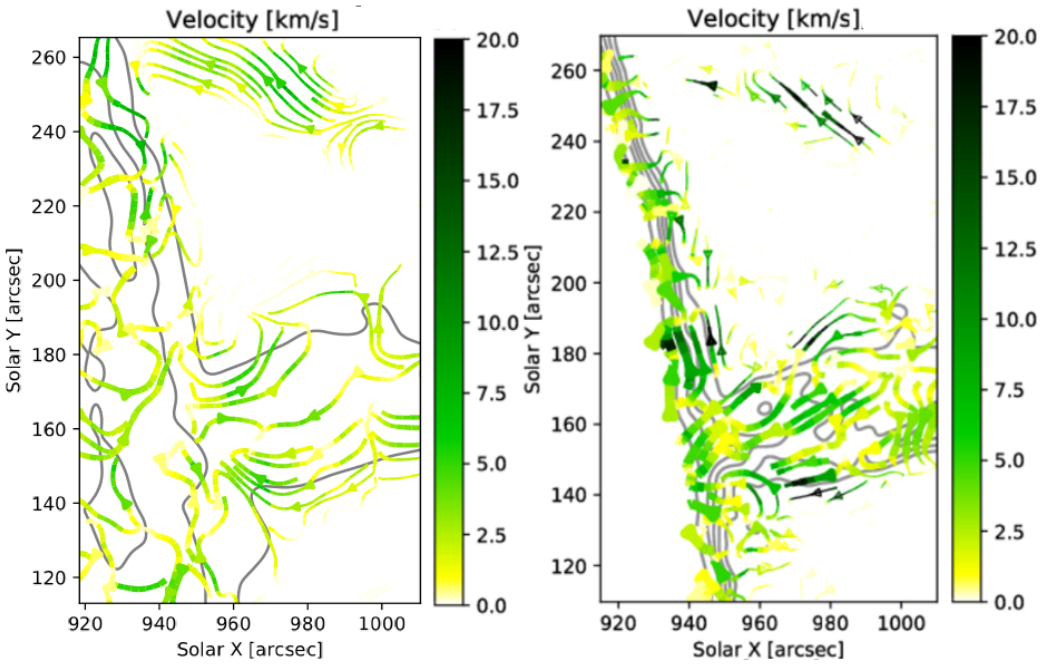

Figure 3.19 POS velocity derived from AIA image pairs between 15:16:43 UT 15:17:43 UT (left panel) and IRIS image pairs between 15:16:57 UT and 15:17:30 UT. The color indicates the value of velocity, the arrows indicate its direction, and the thickness is related to the observed intensity in AIA.

between the two peaks is larger than 0.5 Å. The criterion of 0.5 Å is set based on statistical observations of Mg II profiles, and this separation is too large to be explained by opacity for central-reversed profiles. The classification of the Mg II k&h profiles is similar to that used by Levens et al. (2017), except that one peak profiles that are away from the line center (at a distance larger than 0.4 Å) are also taken as complex profiles in their classification.

Figure 3.21 shows the spatial distribution of the three groups of profiles in the prominence, as derived from IRIS spectral observations between 15:10 and 15:27 UT, with pixel size degraded to 1"$\times$ 1". Out of all the profiles of the prominence in the left panel of Figure 3.21, about 60 % belong to group A, 14 % belong to group B, and 26 % belong to group C. This result is different from the statistics derived by Jejčič et al. (2018). They found that about 80% of Mg II k profiles and 65% of Mg II h profiles in a quiescent prominence were reversed. The right panel of Figure 3.21 shows a sample set of Mg II k spectra obtained by averaging the profiles in regions marked with the 'X' symbols and in colors corresponding to these groups in the left panel of Figure 3.21. We note that the single peaked profile (A) has a Full Width at Half Maximum (FWHM) of 0.2 Å, indicating a turbulence velocity less than 8 km s^{-1}, considering that the instrumental broadening is about 50 mÅ for the spectra in NUV passband. The central-reversed profile (B) is redshifted compared with the single peaked profile. It has a larger red peak and a FWHM of 0.45 Å. The complex-type profile (C) is taken close to the boundary of a region with POS vortical-type motions; it is mainly composed of three independent components, among which the blue-shifted component centers at about 22 km s^{-1} and the two red-shifted

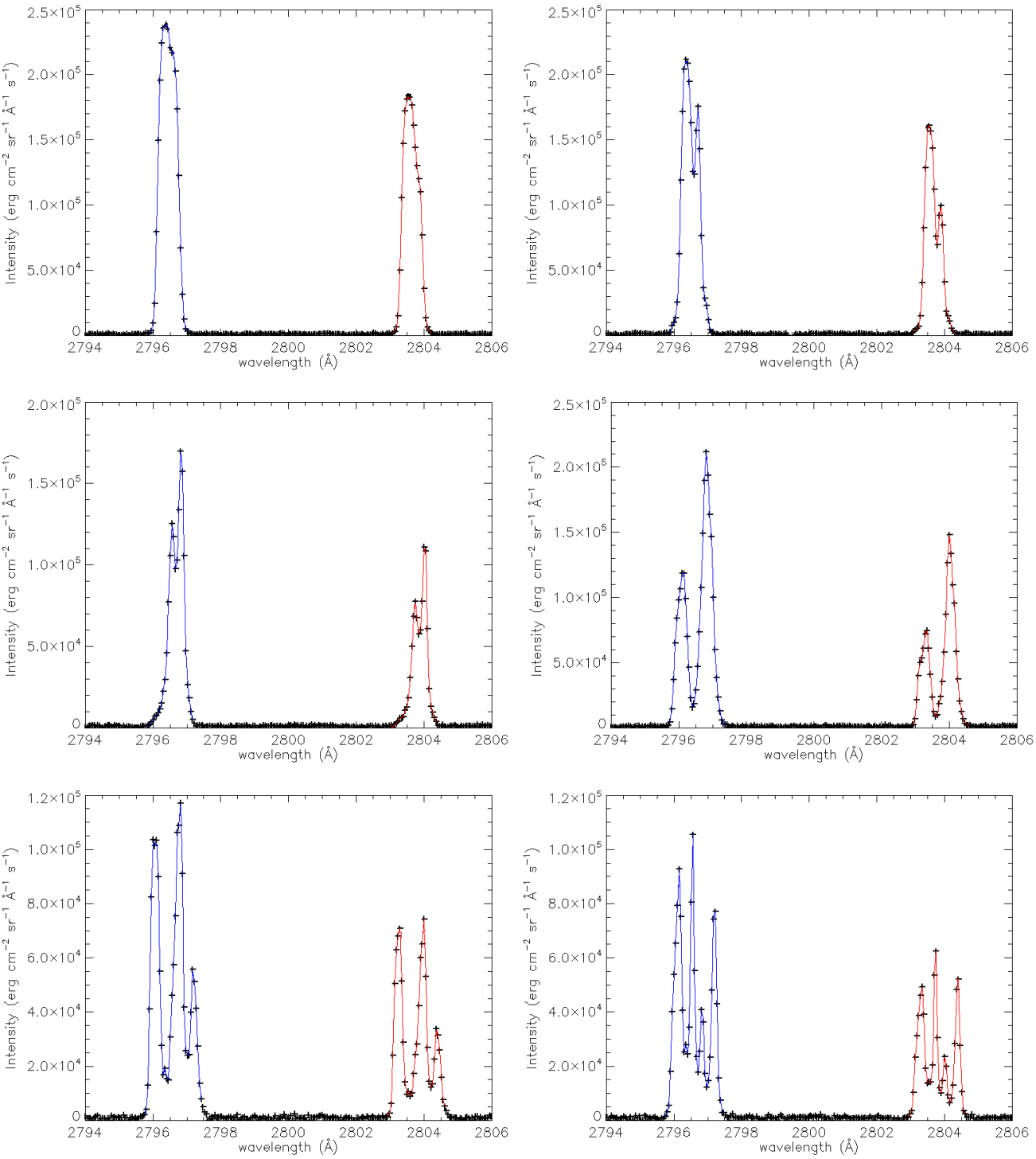

Figure 3.20 Some spatially-resolved spectra of Mg II k (blue) and h (red) lines observed by IRIS in the prominence.

components center at about 42 km s^{-1} and 82 km s^{-1} respectively. The combination of the different structures moving with opposite-sign velocities along the LOS forms a pattern of counter-streaming flows. Both the red-shifted and blue-shifted components still exist in the original profiles (before averaging), possibly indicating a pattern of counter-streaming motions in this region (see Zirker et al., 1998).

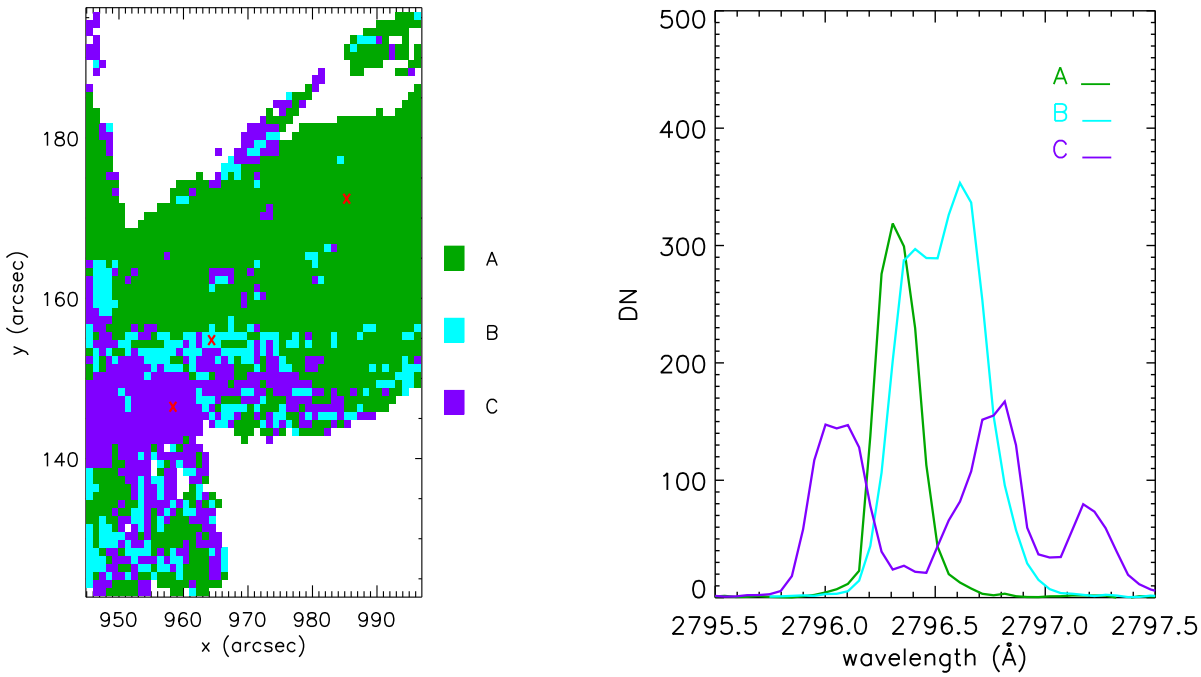

Figure 3.21 Left: The spatial distribution of the 3 groups of profiles in the prominence in different colors derived from IRIS spectral observations between 15:10 and 15:27 UT. Right: A set of samples of Mg II k spectra obtained by averaging the profiles of pixels marked with red × symbols in the areas with corresponding colors in a).

Determination of Doppler velocities We derived the Doppler velocity in the prominence by comparing the core of the line profiles with an off-limb reference wavelength for Mg II k&h lines. The reference wavelength was obtained by averaging the line profiles measured in a large quiet region above the West limb (see Figure 3.22, inside the white box). In this region the spectral line is expected to be close to its rest wavelength, because there we measure the convolution of the whole disk emission by the instrumental profile. The method was used by Lemaire et al. (1998) to derive a full Sun profile using the Solar Ultraviolet Measurements of Emitted Radiation (SUMER) observation off-limb (800 arcsec above the solar surface) that was scattered by the telescope. Figure 3.23 shows the averaged spectra of Mg II k&h lines above the limb in black. The Mg II k&h profiles averaged over the region on disk inside the red box close to the limb in Figure 3.22 are scaled and over plotted in red. Based on the positions of the line core of Mg II k&h lines, we derive a redshift velocity of about 2 km s^{-1} from the profiles

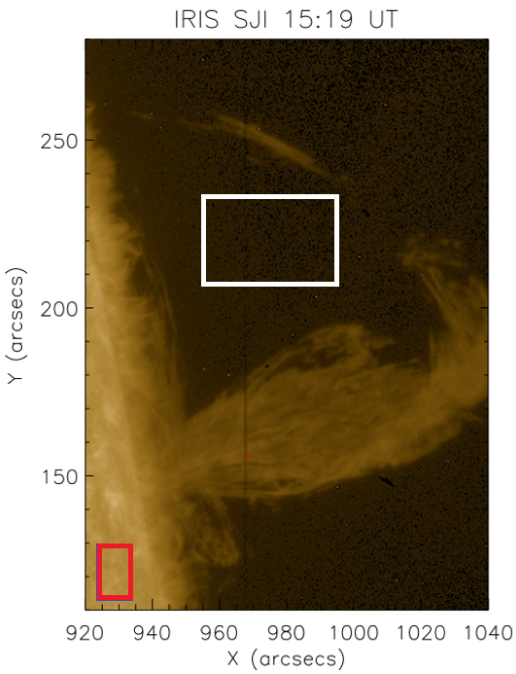

Figure 3.22 Prominence observed by IRIS on May 28, 2014. The reference wavelength was obtained by averaging the line profiles measured in the region inside the white box.

on disk close to the limb compared with the rest wavelength. This is consistent with the redshift velocity of 1.9 km s^{-1} caused by solar rotation close to the equator.

Considering the complex profiles in the prominence, it is difficult to extract the positions of the line core automatically. At first we used the method developed by Leenaarts et al. (2013), which is designed for single or double-peaked profiles. This method uses an extremum-finding algorithm to derive the wavelengths of the maxima and minima in a small spectral region ($-40 < v < 40$ km s^{-1}) around the reference wavelength. If there is an odd number of minima (this is the case for most of the profiles), the middle minimum is then used. Otherwise the minimum with the lowest intensity is used. If no minima are found, a default value of 5 km s^{-1} is used as the velocity shift (Leenaarts et al., 2013). Afterwards a parabolic fit is performed to the spectral points around the estimated line center position to derive the line center velocity and intensity. The profiles with results that are too far from the starting estimate (i.e., an erroneous fit) will be taken as outliers (Leenaarts et al., 2013).

Figure 3.24 shows a map of the Doppler velocities obtained from IRIS spectral observations between 15:10 and 15:27 UT, while the slit scans the lower part of the prominence in 64 steps. Positive velocities correspond to redshifts and indicate horizontal motions (parallel to the solar surface) moving away along the LOS. We find that the central part of the prominence, where mainly single peak profiles (A) are located, is dominated by red-shifted strands. The velocity in the central part of the red-shifted, elongated strands, whose size normal to the main axis is between 5 and 8", is between 10 and 20 km s^{-1}. Several blue-shifted cells, whose cross-sections are around 2", are distributed between the red-shifted strands. In the central

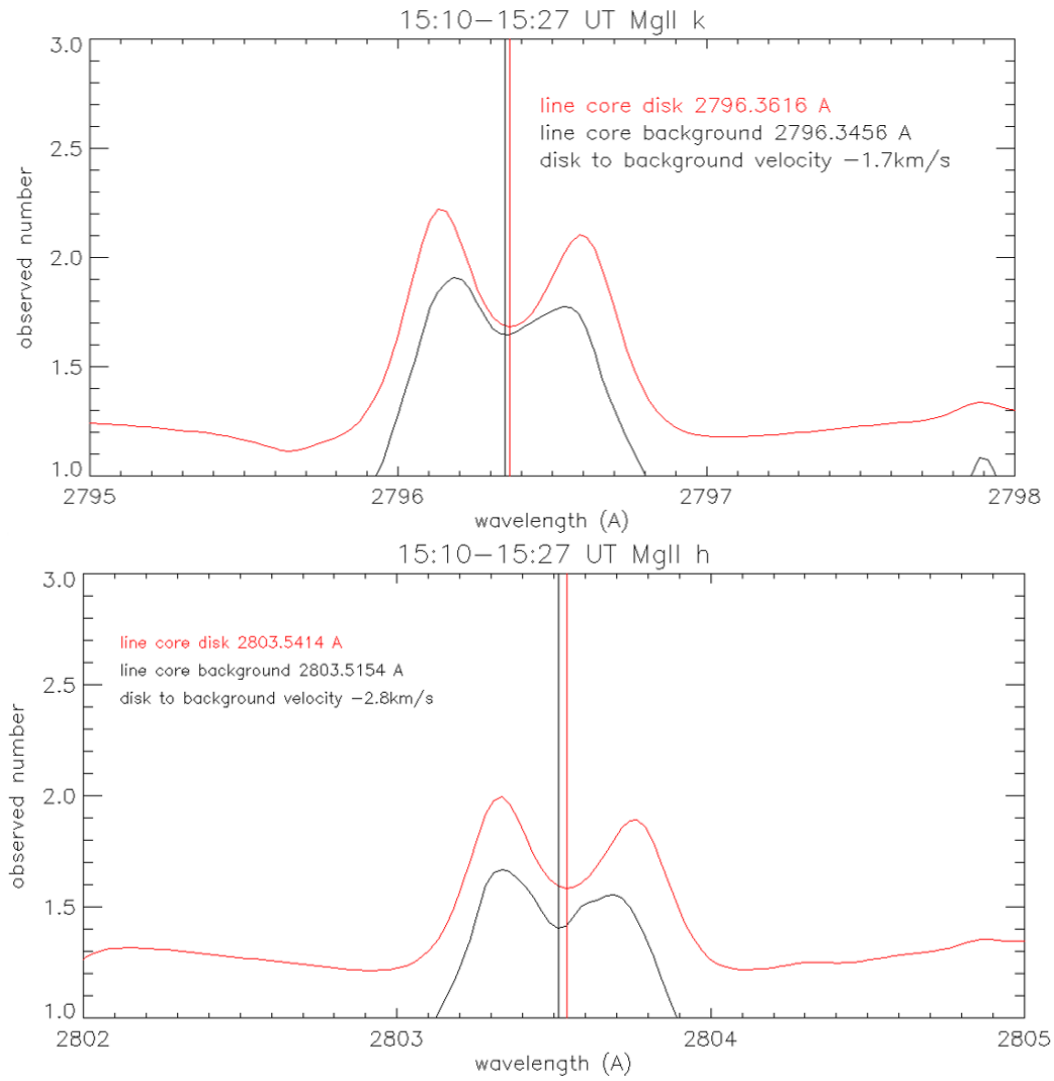

Figure 3.23 Upper and lower panels are the averaged spectra of Mg II k and h lines respectively. The red lines show the profiles averaged over the red box on disk in Figure 3.22. The black lines show the profiles averaged over the white box above limb in Figure 3.22.

part of these blue cells, the velocity is between 5 to 10 km s^{-1}. Most of the complex profiles (C) are located in the boundary region of the prominence. This region is dominated by blue shifts, as shown in Fig. 3.24, with a velocity between 15 to 25 km s^{-1}.

However, the large variation of the complex shapes of the C type profiles introduces uncertainties when applying the extremum-finding algorithm in our analysis, especially when the profile is composed of several independent components caused by the presence of different structures moving with different velocities along the LOS, as shown in Fig. 3.25. The black lines show the positions of the line centers of Mg II k and h lines derived by the extremum-finding method. We find that only two of the four main components are taken into account using the extremum-finding algorithm, because it works on a small spectral region ($-40 < v < 40$ km s^{-1}) around the reference wavelength. The red lines show the positions of the gravity centers of

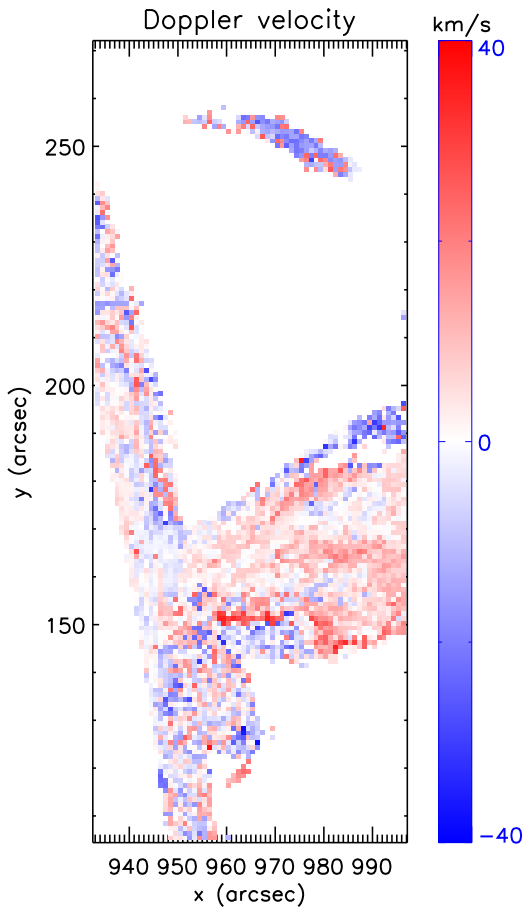

Figure 3.24 Doppler shifts computed from the extremum-finding of the Mg II k&h line profiles between 15:10 and 15:27 UT. The pixel size in the y direction has been degraded to 1" to have square pixels.

Mg II k and h lines which could represent better all the components of the profile. Furthermore, in the regions close to the edges of the prominence, where the signal is lower and line profiles are noisy, it is difficult to get robust features in the spectra with the extremum-finding method. In these cases, the center of gravity of the whole profile could represent better the mean velocity of all the components of the profile.

Figure 3.26 shows the Doppler shift map computed from the center of gravity of the Mg II k&h line profiles at different times during the observation. Between 15:10 and 15:27 UT the velocity pattern is similar to the one derived with the extremum-finding method (see Fig. 3.24) in the central part of the prominence, where there are three long red-shifted strands and several small blue cells in between. While at the north and south edges, red shifts are derived instead of blue shifts. The velocity is between 25 and 65 km s^{-1} in these regions. Such values seem to be typical of prominence edges, as derived from Hα by Mein (1977) or Mg II h&k by Vial et al. (1979). The difference between these two methods at the southern edges where C type profiles dominate mainly comes from the complex shapes of the profiles. For instance, from the type C profile in Fig. 3.21, which is composed of one blue-shifted and two red-shifted components as

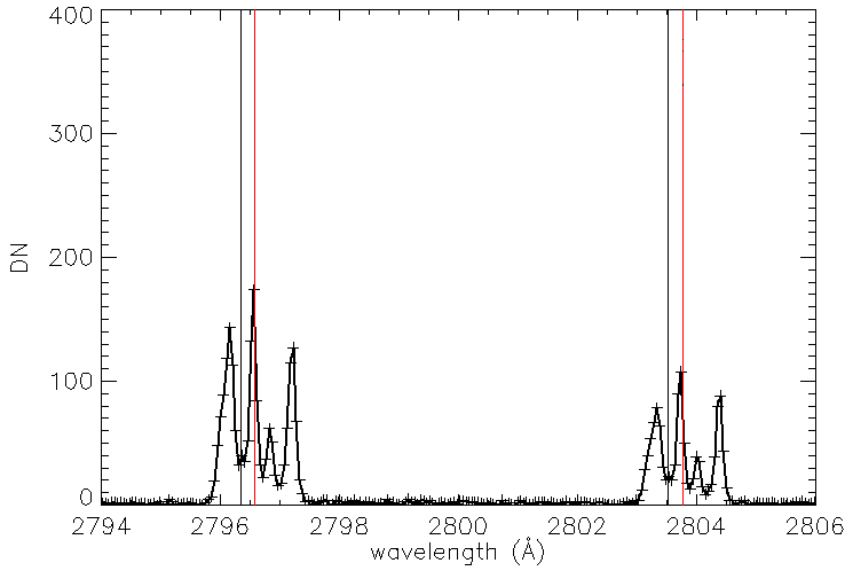

Figure 3.25 Mg II k and h spectra derived in the prominence. The black lines show the positions of the line cores of Mg II k and h lines derived by the extreme-finding method. The red lines show the positions of the gravity centers of Mg II k and h lines.

an example, a blue shift of 22 km s^{-1} is derived with the extremum-finding method, as only the blue component close to the rest wavelength is taken into account; in contrast, a red shift of 25 km s^{-1} is derived from the gravity center of the whole profile. We computed the Doppler shift from gravity centers for all the 16 consecutive IRIS rasters. As shown in Figure 3.26, during the whole observation time of IRIS, the derived trend of velocity pattern evolves only slightly in the central part of the prominence, except when several small red-shifted cells become blue-shifted, and vice versa. At the beginning of the observation, red shift and blue shift cells with a velocity value less than 15 km s^{-1} are found at the south edges. Later on they change into red shift strands with a velocity between 20 and 70 km s^{-1}. Between 14:52 UT and 15:44 UT, a red shift strand with a velocity between 20 and 50 km s^{-1} is observed at the north edge of the prominence. In the upper part of this panel, blue-shifted strands can be observed moving away from the prominence body during the observing time. It should be mentioned that it is difficult to get reliable velocity from multi-peak profiles (Group C). However, we only computed the mean velocity of all the components of the profile to derive an average mass flow in the present work.

Velocity vectors from IRIS

We also derived the POS velocity maps from IRIS SJI images and combined them with the Doppler velocities derived from IRIS spectral observations. For IRIS observations between 15:10 and 15:27 UT, only one raster observation is performed while there are 32 SJI images.

First we applied the optical flow algorithm mentioned above on IRIS SJI images and derived the POS velocity for the 32 SJI images. Afterwards we combined the velocities from different SJIs taken at times corresponding to different slit positions to obtain a POS velocity map which is consistent with the Doppler velocity map in time and space. The streamlines of the derived POS velocity are overplotted in Fig. 3.27, giving a visualization of 3D velocity vectors in the prominence. Doppler velocity is shown in the background with the red-blue colorbar. Positive velocities indicate horizontal motions moving away along the line of sight (redshifts). Streamlines show the direction of the POS velocity. The color gives the value of the velocity, the arrow shows the direction of the velocity and the thickness is proportional to the observed intensity.

We find that downflows dominate the lower part of the prominence with a velocity smaller than 20 km s^{-1} during the whole observing time of IRIS. Since from the 3D reconstruction (Sect. 3.3.1) the observed prominence body is located behind the POS, and the inclination angle between the prominence axis and POS is around 60°at 16:16 UT, the redshift in the prominence may be caused by downward motions. In Fig. 3.27 we find that Doppler red-shift strands are roughly coincident in space with POS downflows and the ratios of Doppler velocities to POS downflow velocities vary from 1 to more than 3 in the red-shifted strands. This result is consistent with the 3D geometry of the prominence. Besides, it is found that some red-shifted cells became blue-shifted, and vice versa over the period of observation. This may indicate untwisting motions of the structure. In the upper part of this panel, away from the prominence body, there is a blue-shifted strand away from the prominence body with a POS velocity of 25 km s^{-1}. Considering the low heights and low speeds, it could correspond to a clump of coronal rain material falling from the prominence along the field lines, towards the observer.

3.3.3 Mg k/h ratio

We also computed the intensity ratio of the Mg II k and h lines by identifying the corresponding components in both lines and integrating their intensities. The intensity ratio is a simple and useful tool for plasma diagnostics and can be used to investigate their opacity. Under the optically thin assumption in a collision-dominated plasma, the k/h ratio is simply the ratio of the oscillator strengths, 2:1 (Mathioudakis et al., 1999; Çelik et al., 2011). In the optically thick case, this ratio is smaller. The six panels in Figure 3.28 show maps of Mg k/h ratio in the prominence derived from the IRIS spectral raster scan at different times. We find that the k/h ratio is larger than 1.35 in the prominence and it is generally around 1.4 in its main body. This value matches well with model results (Heinzel et al., 2014) and previous observations (Vial, 1982a; Schmieder et al., 2014; Levens et al., 2016). It roughly corresponds to the ratio of the incident intensities (1.28 at the line core position), and it further indicates that the medium is optically thick and radiation-dominated. Similar values have been reported in previous observations. Heinzel et al. (2014) and Schmieder et al. (2014) derived 1.33–1.35 in quiescent prominences with IRIS observations. Liu et al. (2015) found a wide range of k/h ratios in an erupting prominence, the

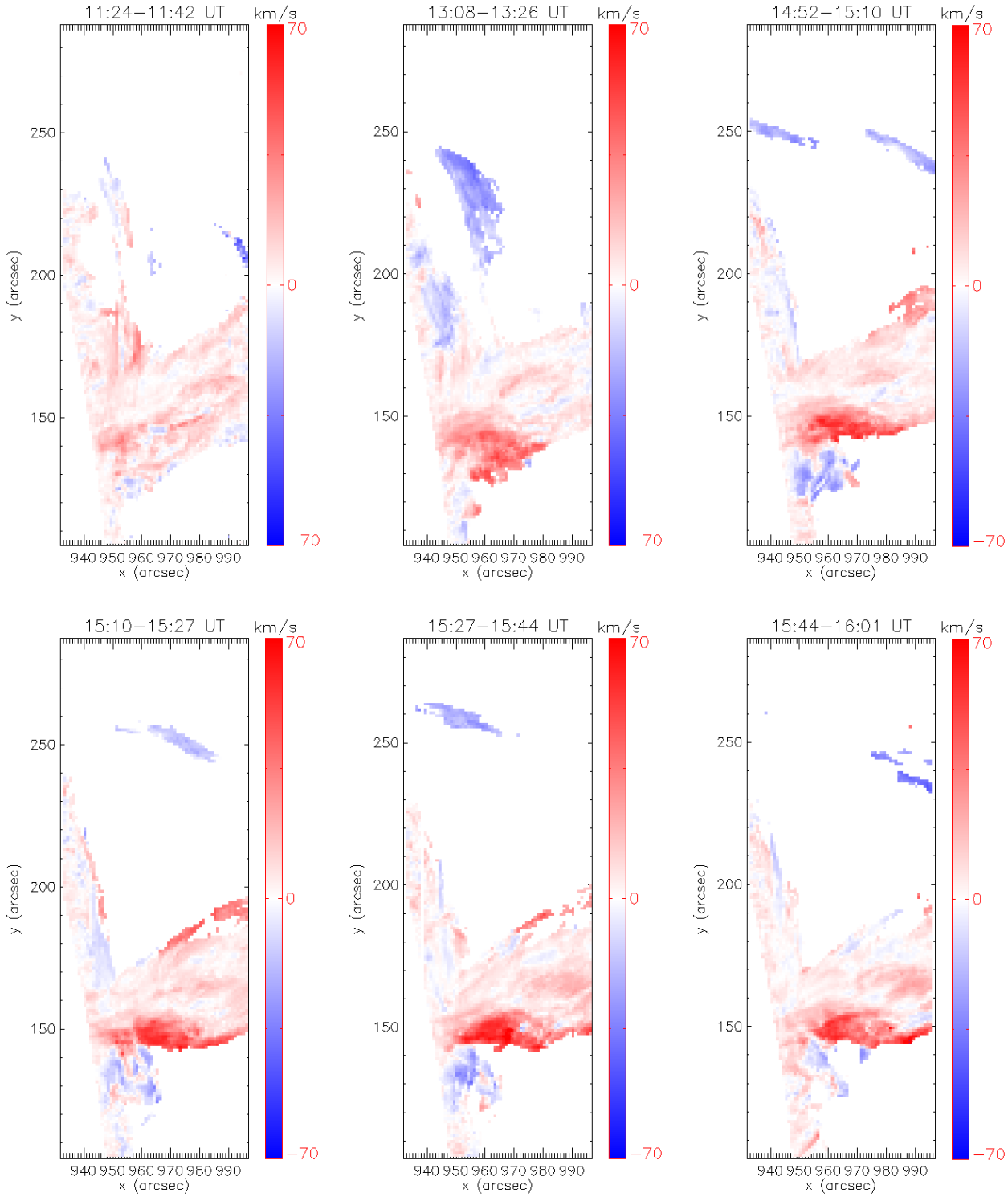

Figure 3.26 Doppler shifts computed from the center of gravity of the Mg II k&h line profiles at different times. The pixel size in the y direction has been degraded to 1" to have square pixels.

median value of 1.17 that is the lowest ever-reported value, corresponds to material falling back while a higher value of 1.63 was found in the coronal rain nearby. The intermediate values (1.41 and 1.53) were found in two components of the eruptive prominence. We also derived

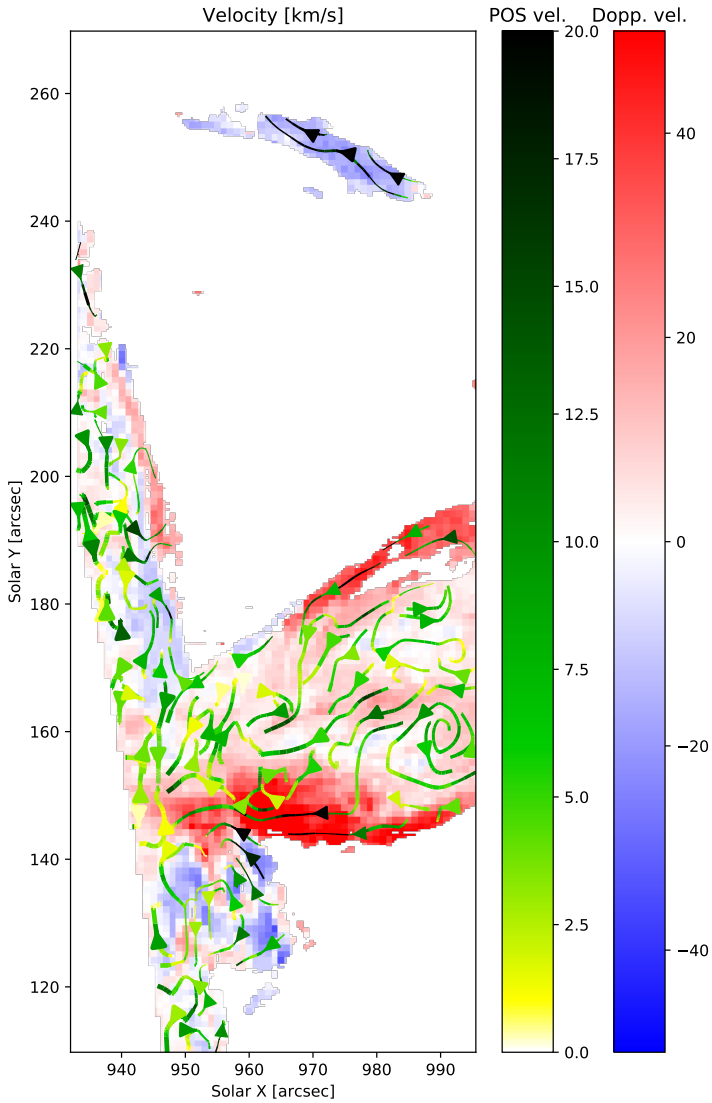

Figure 3.27 Composite velocity map derived from IRIS spectral and SJI observations between 15:10 and 15:27 UT. Doppler velocity is shown in the background with the red-blue colorbar. Positive velocities indicate horizontal motions moving away along the line of sight (redshifts). Streamlines show the direction of the POS velocity. The color gives the value of the POS velocity, the arrow shows the direction of the velocity and the thickness is proportional to the observed intensity in IRIS SJI.

k/h ratios up to 1.7 to 2.0 in regions close to the edges, where Doppler redshifts are relatively larger. This is perhaps an indication that the medium is not so thick in these regions and there is a higher (relative) collisional contribution resulting from a higher temperature close to the edges.

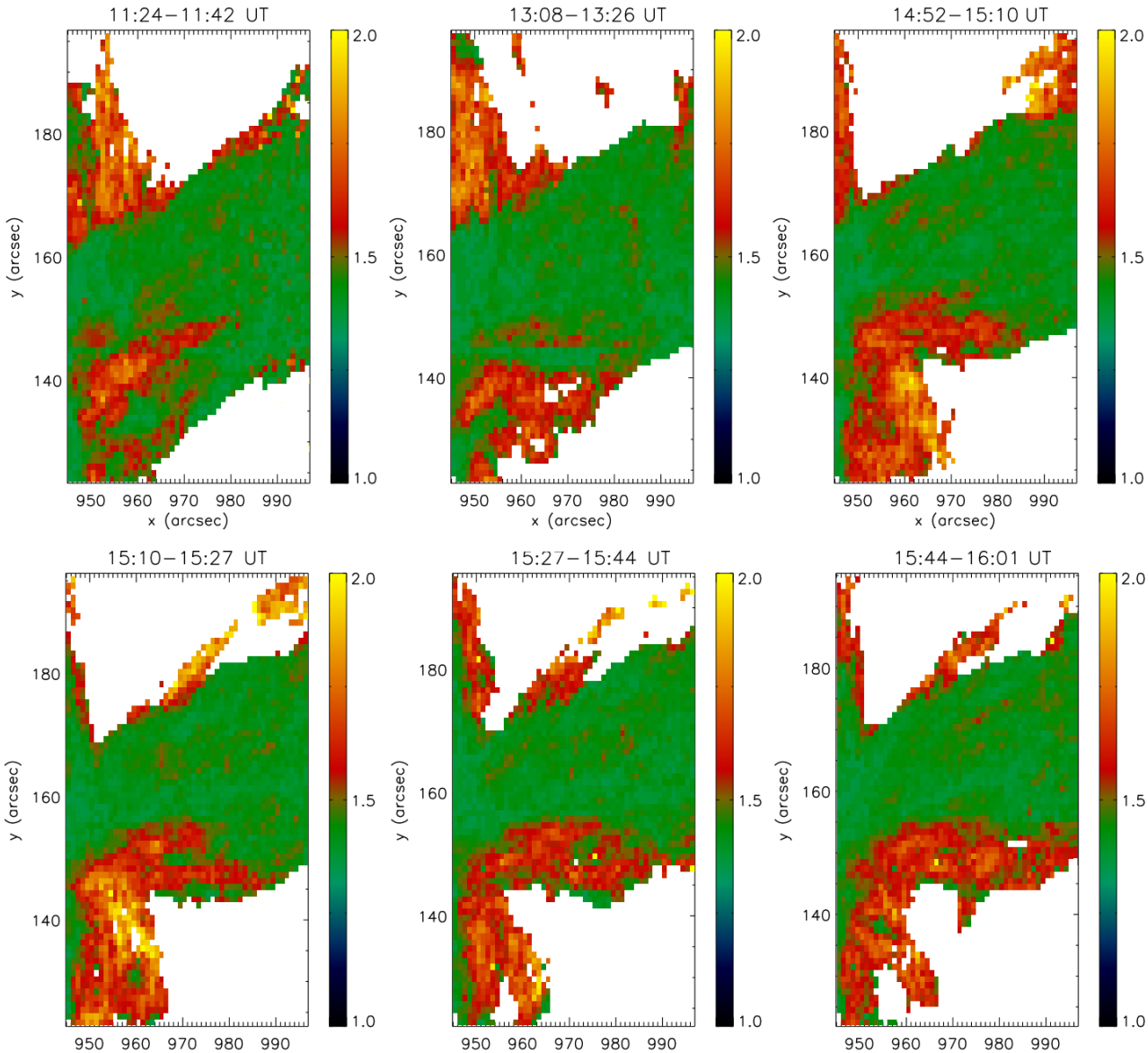

Figure 3.28 Maps of the Mg II k/h intensity ratio in the prominence derived from IRIS spectral observations. The observation duration of each panel is shown at the top.

3.4 Diagnostics of density, temperature, and ionization degree

We performed plasma diagnostics by comparing Mg II h&k integrated intensities from IRIS observations and from the NLTE radiative-transfer code PRODOP_Mg (see more details in Chapter 4). The prominence structure in this model consists of one-dimensional (1D) isothermal and isobaric plasma slabs standing vertically above the solar surface and illuminated by the radiation from the surrounding solar atmosphere. The input parameters of this code include gas pressure, temperature, the height above the solar surface, the thickness of the slab, and the microturbulent velocity. The outputs include physical parameters such as electron density,

hydrogen density, Mg I, II, and III ground state populations, and optical quantities such as the total intensity of Hydrogen lines and Mg II lines, and the optical thickness in hydrogen and Mg II lines.

Incident radiation In the case of solar prominences modeling, the incident radiation intensity is a key boundary condition (Heinzel, 2015). At a chosen point above the solar surface in the prominence, the incident radiation is computed by integrating all the radiation received at the point over all of the atmosphere that are visible to the chosen point (Brown and Labrosse, 2018), as seen in Fig. 3.29 (Sahal-Brechot et al., 1986). We compute the mean local intensity (in $\mathrm{erg\,s^{-1}\,sr^{-1}\,cm^{-2}\,Å^{-1}}$) and take into account the effect of the geometry, the active regions on the solar surface, and the radial variation of the solar brightness.

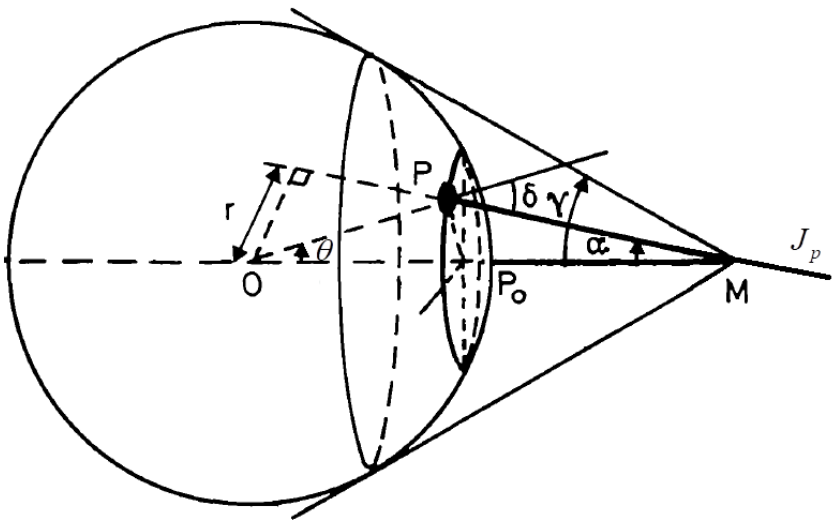

Figure 3.29 Coordinates of the region on the solar surface. P_o is the center of the observed region, M is the scattering point which is located in the prominence. P_oM is the height over the limb (Sahal-Brechot et al., 1986).

The chromosphere being optically thick for Mg II k&h lines, we simply assume that the incoming radiation mainly comes from the solar surface. We set the surface to be in the upper chromosphere, 3800 km above photosphere, which is the position of the Mg II limb. It is derived from the full disk average radial intensity variations of the Mg II k&h line cores, based on the analysis of the IRIS mosaic observation on May 27 2014. The inflection point where the derivative has a local minimum is taken as the position of the Mg II limb (the position of the black line in Figure 3.30), which is 5.4" above the visible solar surface.

The prominence is illuminated by radiation from the solar surface in all directions, and the incident radiation varies in different directions. The mean intensity coming from all directions is derived by averaging over the solid angle Ω which limits the solar horizon of the point M in the

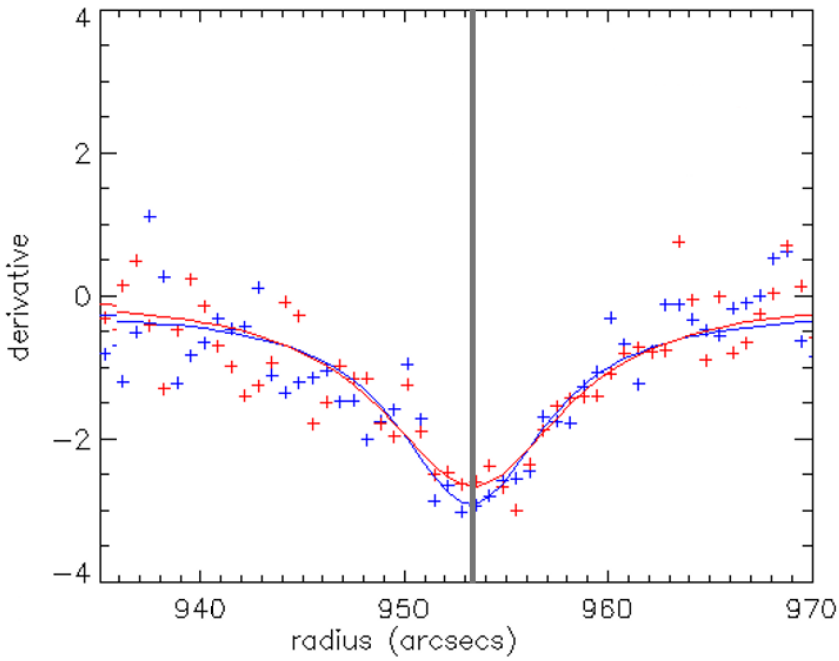

Figure 3.30 The derivatives of the full disk average intensity variations close to the limb derived from the IRIS mosaic observation on May 27 2014. The results of the line core intensities for Mg II k and h lines are shown with '+' in blue and red respectively. The blue and red curves are the fitted lines for k and h lines.

prominence, at some height above the surface:

$$J = \frac{1}{4\pi} \oint_{\Omega} J(\Omega)\, d\Omega \tag{3.1}$$

The contribution from the surface in different directions is computed from the radiation J_{P} at different points P on the solar surface:

$$J_{\alpha} = \frac{1}{4\pi} J_{\mathrm{P}} \Delta\Omega \tag{3.2}$$

in which

$$\Delta\Omega = \Delta S \cos\delta / \rho^2 = \frac{\Delta S}{\rho^2} \sqrt{1 - \left(1 + \frac{h}{R_{\odot}}\right)^2 \sin^2\alpha} \tag{3.3}$$

where α is the angle between MP and the local vertical, $\rho = \mathrm{MP}$, $h = \mathrm{P_0M}$ is the height of M above the limb, $R_{\odot}$ is the solar radius, and δ is the angle between the normal to the surface of the Sun and the MP direction.

In our computation J_{P} is mainly derived from the absolute intensities of IRIS mosaic observations in Mg II k&h lines. We calculate the absolute radiation intensity from a IRIS full-disk mosaic observation taken from 10:06 UT on May 27 to 3:30 UT on May 28, assuming that the variation of solar radiation in Mg II k&h lines is negligible between the observing times of the mosaic and the prominence of this work. This observation is transformed into Carrington

coordinates, as shown in Fig.3.31, and complemented with He II 304 Å data from STEREO A taken at 15:00 UT on May 28 using World Coordinate System (WCS) routines in the Solar Software Tree (Thompson, 2006). The regions inside the red, green and blue circles indicate where the incident radiation comes from at the heights of 10 000, 20 000 and 50 000 km over limb respectively. There is no large active region but only small bright fragments scattered inside these circles. Thus we calculate the incident radiation from absolute intensities of the mosaic observation for heights lower than 20 000 km. For heights between 20 000 and 50 000 km, it is computed from the derived incident radiation at the height of 10 000 km by applying the geometric dilution factor. The geometric dilution factor W depends on the height h over the limb, when assuming a uniform angular brightness coming from a spherical surface, it can be given as:

$$W = 0.5 \times (1 - \sqrt{1.0 - (\frac{R_\odot}{R_\odot + h})^2}\ ) \tag{3.4}$$

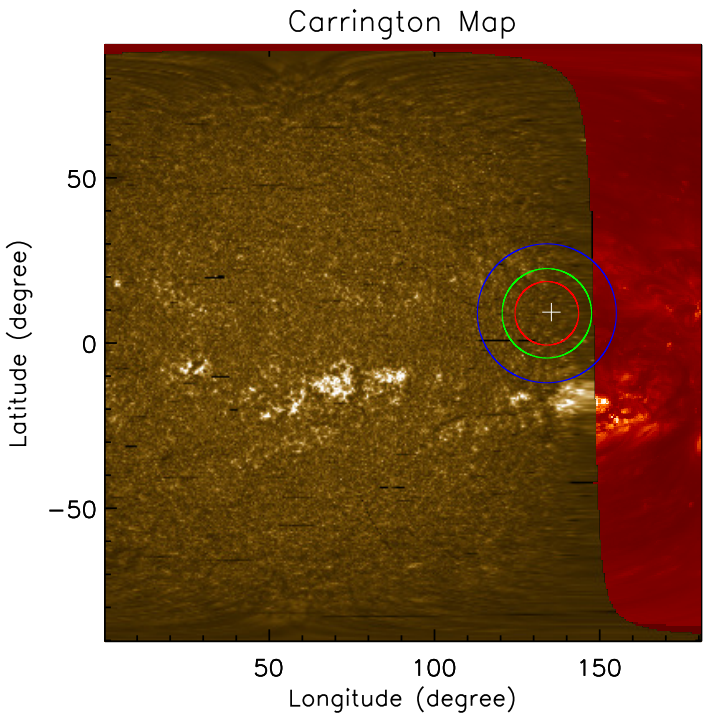

Figure 3.31 Composite Carrington map of the solar hemisphere centered on 90° Carrington longitude, with the IRIS mosaic of 2014-05-27 (Mg II k radiance, yellow) and, behind the IRIS limb, He II 304 Å data from STEREO A taken at 15:00 UT on May 28 (in red). The regions inside the red, green and blue circles indicate where the incident radiation comes from as seen from an altitude of 10 000, 20 000 and 50 000 km over the limb respectively, at the position of the prominence (+ symbol).

We also compute the center-to-limb variation of the radiation at different heights above the solar surface in our calculation of the incident radiation. This variation was usually neglected in

previous modeling of Mg II lines, e.g., Heinzel et al. (2014) used Mg II h and k lines on the solar disk from the RASOLBA experiment (Staath and Lemaire, 1995). The absolute intensities are derived by comparing with the OSO 8 LPSP observations. We calculated the center-to-limb variation from the IRIS mosaic observation taken on 12 March 2017, when there was no apparent active region on disk. In Fig.3.32 the left panel shows the mosaic observation in Mg II k line, the right panel shows the mean profile of Mg II k line averaged over the full disk in the left panel.

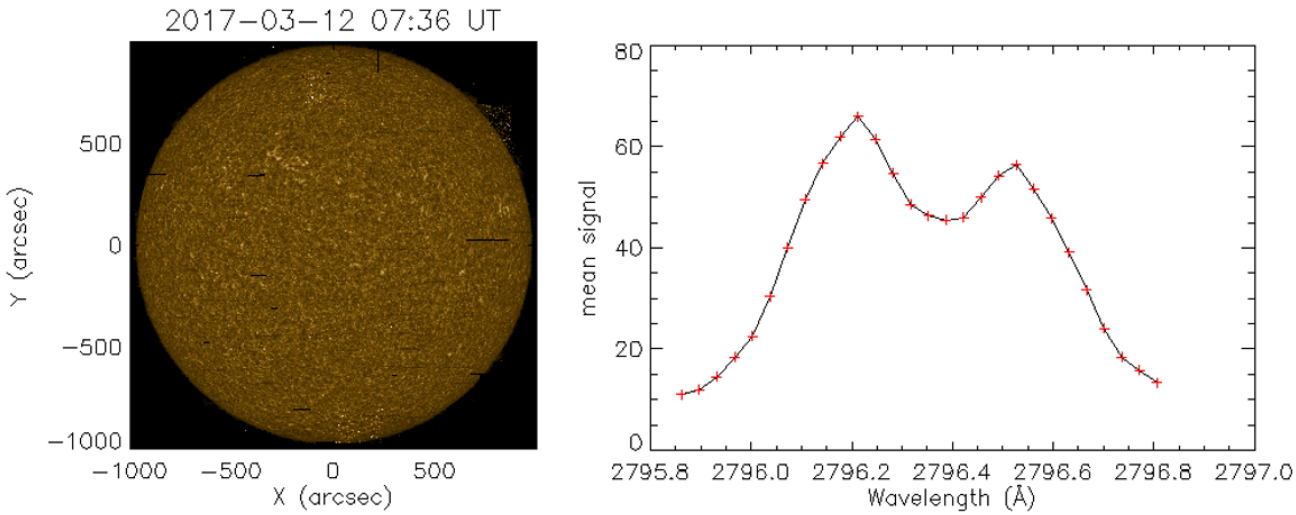

Figure 3.32 Left: IRIS mosaic image taken on 2017-03-12 in Mg II k line. Right: The mean profile of Mg II k line averaged over the full disk in the left panel.

We take the full disk image in Fig.3.32 as a representation of the "mean quiet Sun" and derive the radial intensity variation for Mg II k&h spectrum. Fig. 3.33 shows the derived center-to-limb variation at the wavelength of k_3 and k_{2v} of the mean profile. We find that the intensities decrease from the center to limb for both k_3 and k_{2v}. The limb-darkening effect may be caused by the variation of the formation height of k_2 and k_3 from the center to limb. More dark fibrils that lie higher in the solar atmosphere are taken into account close to the limb (Schmit et al., 2015). We have limb darkening at the positions of the blue and red peaks of the k&h lines, and the variation changes from limb darkening to limb brightening in the wavelength range between k_2 and k_1. This change may only be apparent and caused by the variation of the thermal broadening of the k&h lines, which makes the peaks go further away from the line center from center to limb, as shown in Fig.3.34.

For our modeling purpose, we rely on the IRIS mosaic observation taken from 10:06 UT on May 27 2014 to 3:30 UT on May 28 2014 to derive the incident radiation from the surrounding solar atmosphere. Clearly, since there is no active region inside the "horizon" as seen from the prominence, the incident radiation comes from quiet regions. This means that our modeling is valid for quiescent prominences only. Figure 3.35 shows the derived incident radiation in Mg II k&h lines at the height of 10 000 km over the limb. We find that the addition of the center-to-limb variation leads to an increase of about 30% around the line cores for both k and h lines.

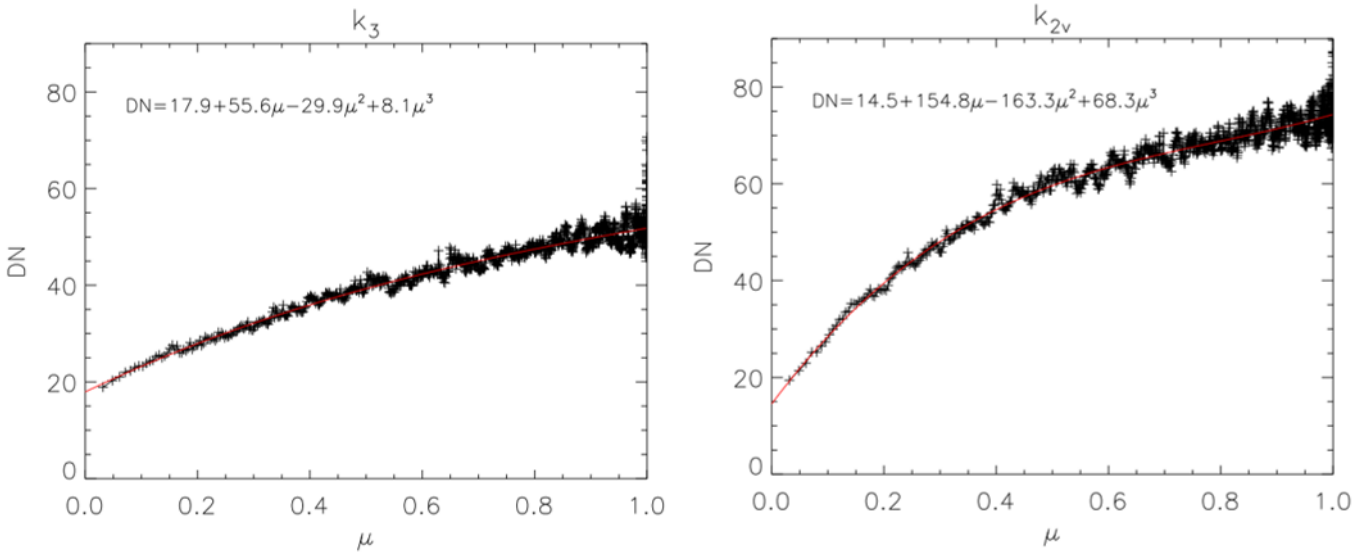

Figure 3.33 Radial variation of intensity in k_3 and k_{2v}. A polynomial fit as a function of μ is over plotted in red.

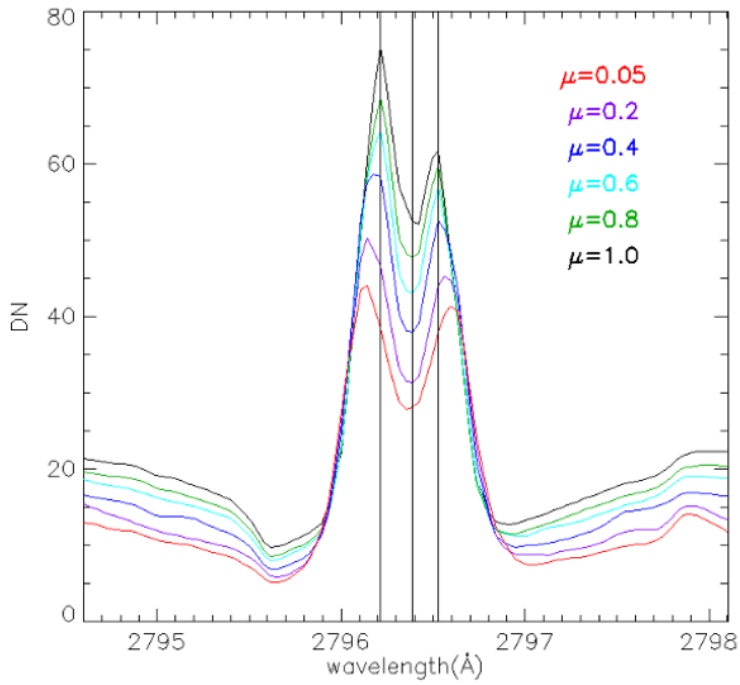

Figure 3.34 Mean profiles of Mg II k derived from IRIS mosaic observation on 2017-03-12. The different colors show the mean profiles derived at different μ positions.

Diagnostics To compare with observations, we built a grid of NLTE models (using the PRODOP_Mg code) with 11 different temperature values covering a range of 5000 to 15 000 K, 45 different pressure values covering a range of 0.05 to 0.5 dyn cm^{-2} and 5 different height values covering a range of 10 000 to 50 000 km, while the turbulent velocity is set to be 5 km s^{-1} for all the models. The thickness is set to be 1000 km given that the cross-sections of the small blue-shifted cells distributed between the red-shifted strands in Fig. 3.24 are about 1"-2".

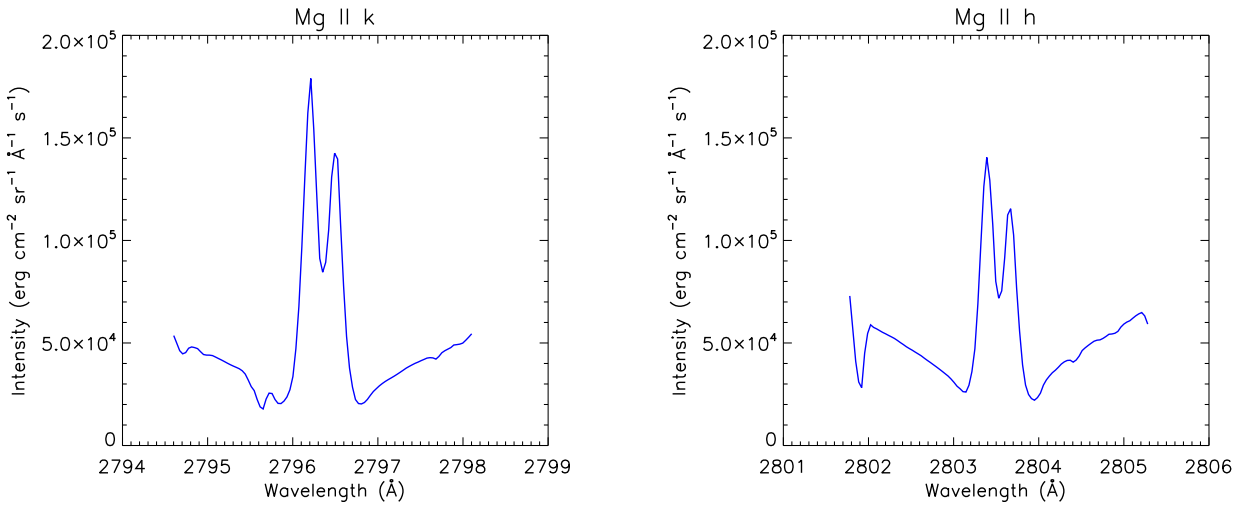

Figure 3.35 Incident Mg II h and k profiles at an altitude of 10 000 km.

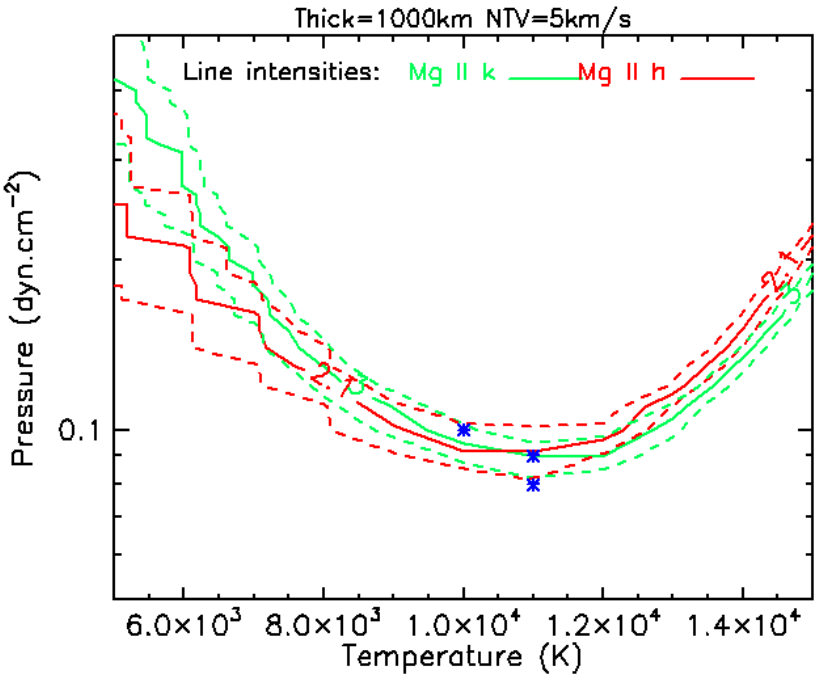

Figure 3.36 The solid lines show how a pair of observed k (in green) and h (in red) line intensities change with pressure and temperature. Considering the uncertainty of the radiometric calibration which is less than 5%, the upper and lower limits of the k and h line intensities are also overplotted in dashed lines.

With the results of all these models, we obtained a range of Mg II h and k line intensities including profiles as well as the integrated intensities changing with temperature and pressure. We calculated Mg II h&k integrated intensities from IRIS spectral observations which have been binned to have square pixels of 1"×1". Then we computed the deviation of Mg II h&k

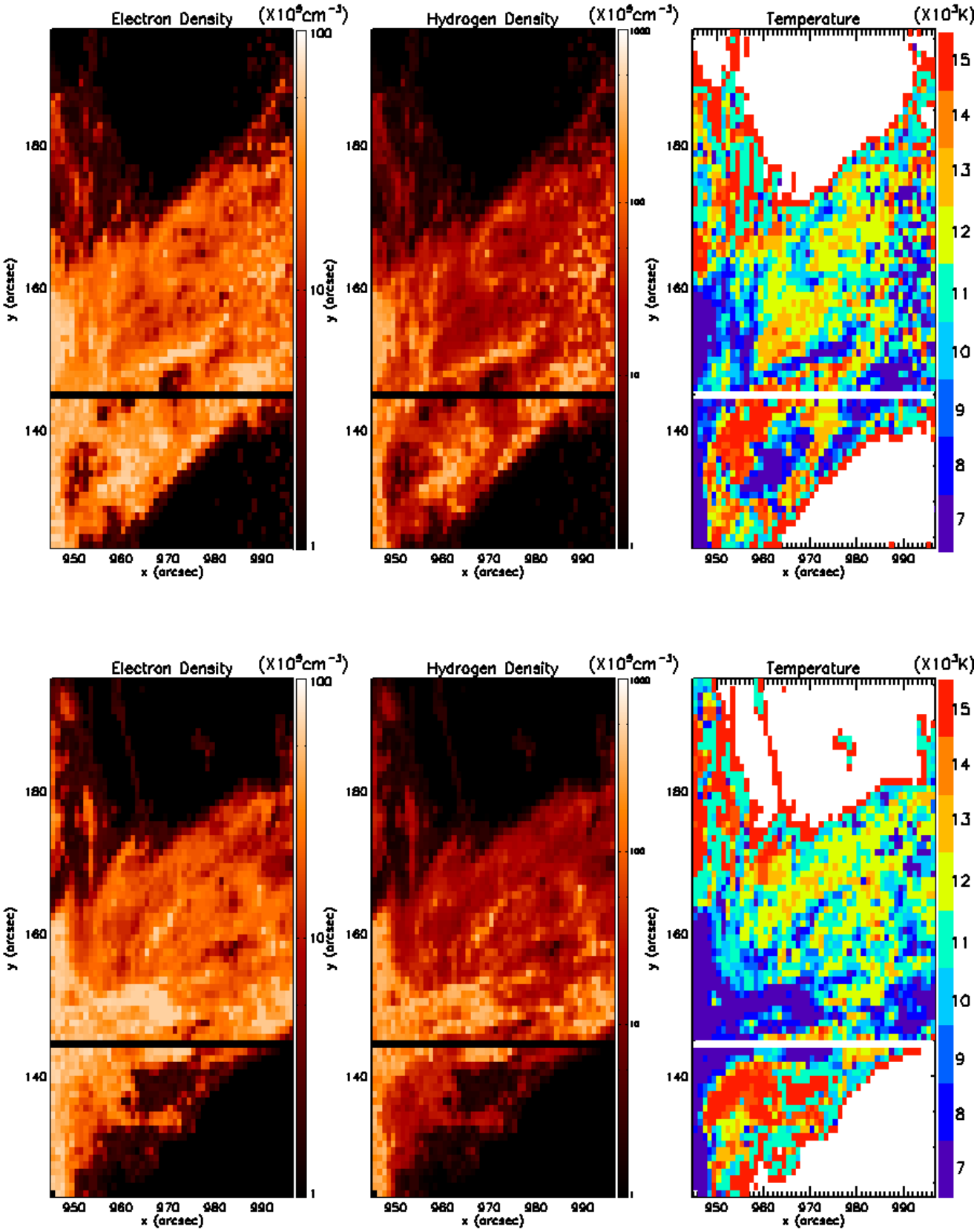

Figure 3.37 Electron density (left of each panel), hydrogen density (middle of each panel) and temperature (right of each panel) in the prominence derived from IRIS spectral observations between 11:24 and 11:42 UT (top) and between 13:08 and 13:26 UT (bottom).

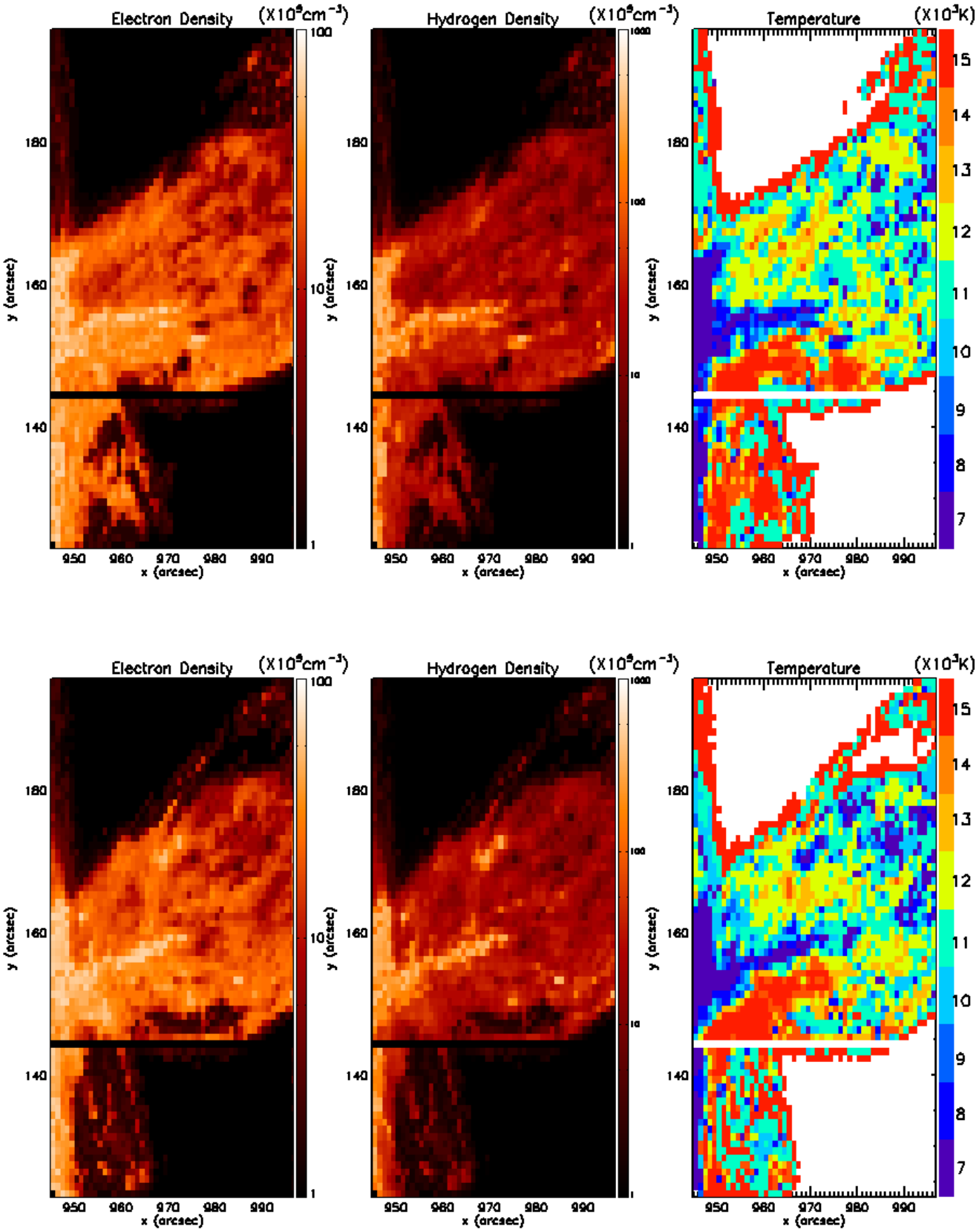

Figure 3.38 Electron density (left of each panel), hydrogen density (middle of each panel) and temperature (right of each panel) in the prominence derived from IRIS spectral observations between 14:52 and 15:10 UT (top) and between 15:10 and 15:27 UT (bottom).

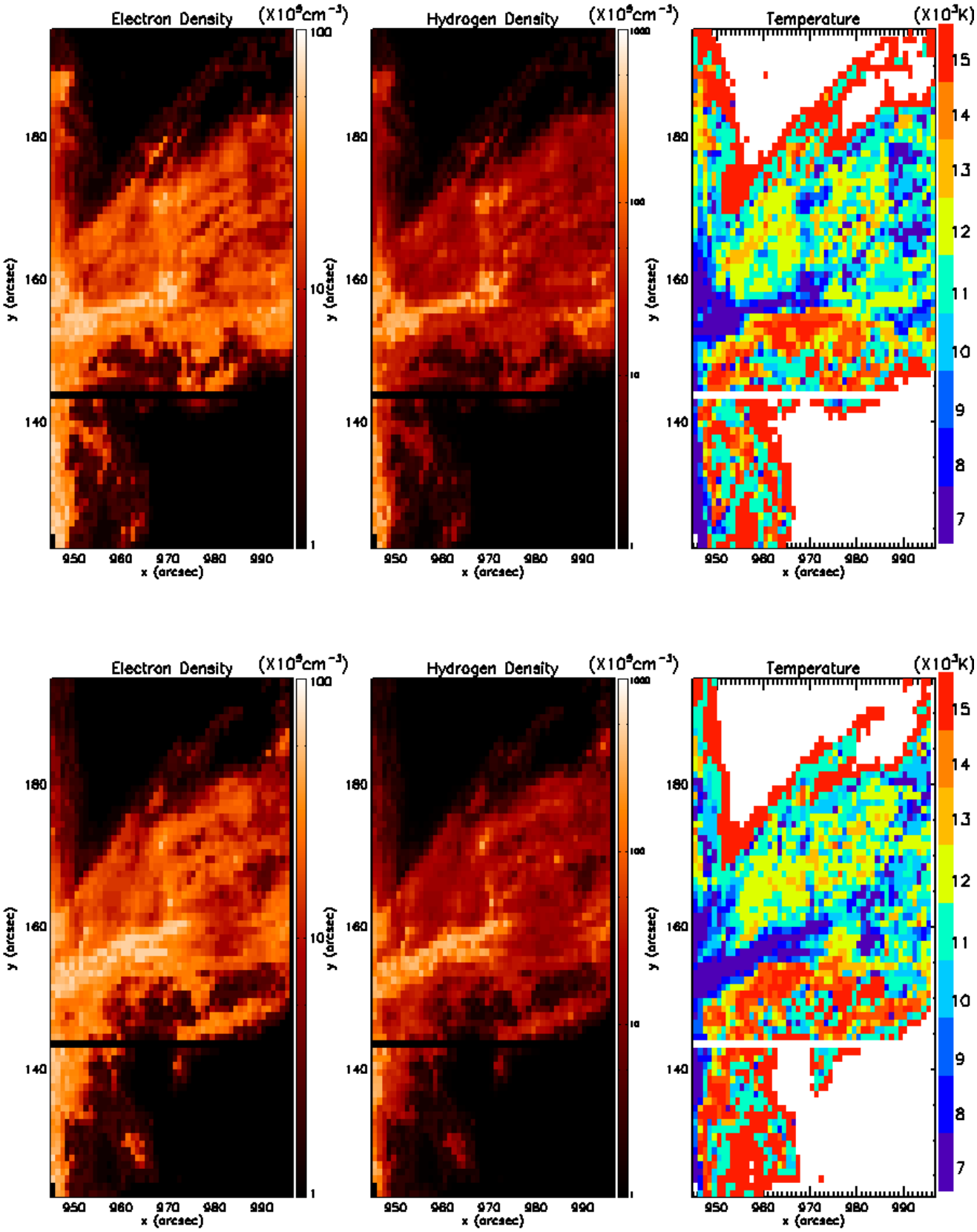

Figure 3.39 Electron density (left of each panel), hydrogen density (middle of each panel) and temperature (right of each panel) in the prominence derived from IRIS spectral observations between 15:27 and 15:44 UT (top) and between 15:44 and 16:01 UT (bottom).

Table 3.2 The derived ranges of temperature, electron density, total hydrogen density and ionization degree in the prominence.

Physical parameter	
T(K)	7000-15000
n_e (cm^{-3})	1.3×10^9 - 7.0×10^{10}
n_H (cm^{-3})	1.5×10^9 - 3.6×10^{11}
n_e/n_g (n_g is the ground level hydrogen density)	0.1–10

line intensities between observations and outputs of the models. We determined the optimum temperature and density simultaneously for the observations by minimizing the RMS residuals of both intensities. The solid lines in Figure 3.36 show how a pair of observed k (in green) and h (in red) line intensities change with presse and temperature. Considering the uncertainty of the radiometric calibration which is less than 5%, the upper and lower limits of the k and h line intensities are also overplotted in dashed lines. We find that for the optimum temperatures and pressures (marked with '$*$' in blue) for the observed k and h lines, the upper and lower limits are 11 000 K, 0.09 dyn cm^{-2}; 10 000 K, 0.10 dyn cm^{-2} and 11 000 K, 0.08 dyn cm^{-2} respectively. We find that the error of the radiometric calibration leads to an uncertainty of about 15% in the derived physical parameters.

By applying this method in each pixel of IRIS spectral observations, we constructed the 2D density and temperature maps of the prominence. Fig. 3.37, Fig. 3.38 and Fig. 3.39 show how the electron density (left of each panel), total hydrogen density (middle of each panel) and temperature (right of each panel) are distributed in the prominence at different times from the beginning until the end of IRIS observation. The horizontal lines located around y=145" in these figures are fiducials used for calibration (Wülser et al., 2018). In this region the light is blocked from entering. The derived ranges of temperature, electron density, total hydrogen density and ionization degree are listed in Table 3.2.

The derived electron densities range from 1.3×10^9 to 7.0×10^{10} cm^{-3} and the derived total hydrogen densities range from 1.5×10^9 to 3.6×10^{11} cm^{-3} in different regions of the prominence. Our values are consistent with densities estimated in previous studies in the range of 10^9 and 10^{11} cm^{-3} (Hirayama, 1971; Stellmacher et al., 1986; Bommier et al., 1994; Labrosse et al., 2010). The electron and hydrogen densities decrease at the edges of the prominence when assuming a constant effective thickness. High density plasma is mainly located at the bottom of the prominence and extends along the main axis over the whole observation time of IRIS.

We also have information on the electron density from the Si IV doublet at 1394 and 1403 Å. The signal being very weak, we computed profiles averaged in space (over an area about 10"$\times$10" in the lower part of the prominence) and in time (the 16 rasters). The resulting integrated intensities are respectively 36 and 16 $\mathrm{erg\,s^{-1}\,sr^{-1}\,cm^{-2}}$ for the two lines[3]. If we adopt a formation temperature of 7×10^4 K (or $\log T = 4.8$), we can derive an Emission Measure (EM)

[3]A lower value was found from SUMER at 1403 Å, in a different case: 8 to $10\,\mathrm{erg\,s^{-1}\,sr^{-1}\,cm^{-2}}$ (Cirigliano et al., 2004).

of about 8×10^{25} cm^{-5}. Such a value leads to a squared density of 8×10^{17} cm^{-6} (when using the adopted thickness of 1000 km). The average density is consequently of 9×10^{8} cm^{-3}. When equaling the pressure between Mg II ($T = 10000$ K) and Si IV formation ($T = 7 \times 10^{4}$ K) regions, one obtains electron density to be 1.2×10^{10} cm^{-3}, well in the range found from Mg II modeling (1.3×10^{9} to 7.0×10^{10} cm^{-3}).

We also estimated electron densities in the prominence with K-COR white light observations, where the emission is mainly Thomson scattering in this wavelength range. The electron density is then about 7×10^{9} cm^{-3} at the height of 55 000 km above limb around 17:00 UT when assuming a cylindrical geometry with an effective thickness of 1000 km. This density value coincides with the value derived from Si IV measurements and is also well in the range found from Mg II h and k modeling at an altitude of 50 000 km (1.3×10^{9} to 7.0×10^{10} cm^{-3}).

Right panels in Fig.3.37, Fig.3.38 and Fig.3.39 show the derived temperature distribution in the prominence during activation. It is in the range of 7000 to 15 000 K. Labrosse and McGlinchey (2012) found similar values in erupting prominences using the intensity of the He II 304 Å line. The temperature increases at the edges of the prominence to 15 000 K. No conspicuous pattern of temperature distribution is found where x > 980". But we find a low temperature region located along the axis and between the solar surface and the prominence, where we also find a high density in Fig.3.37, Fig.3.38 and Fig.3.39. And the temperature in the regions close to the south edge increases during the activation. The ionization degree was also computed from model results as the ratio of the electron density n_e to the number density of ground level hydrogen n_g. It ranges from 0.1 to 4 in the main body and exceeds 10 at the edges between 15:10 and 15:27 UT, as shown in Fig. 3.40. The values found by Vial (1982a) (around 3) and Hirayama (1985) (1–10) for quiescent prominences belong to our derived range. But the ionization degree reaches rather lower values (down to 0.1), a result rather surprising for an activated prominence.

Mg II line profiles from models. Until now, we relied on the integrated intensities of the Mg II k and h lines to perform the diagnostics of the physical parameters in the prominence. The outputs of the models also contain the profiles of the k and h lines. Considering that the instrumental broadening for the spectra in NUV passband, we convolve the output Mg II profiles with the IRIS instrumental profile, a Gaussian function with a FWHM of 52 mÅ (Wülser et al., 2018), similar to that used by (Heinzel, 2015). Based on the main characteristics of the derived profiles, we generally divide them into 2 groups: A) single-peaked profiles and B) central-reversed profiles. The spatial distribution of the profile types of the optimum models (for k and h line intensities) in the prominence between 15:10 and 15:27 UT, with pixel size degraded to 1"$\times$ 1", is shown in the right panel of Figure 3.21. The spatial distribution of the 3 groups of profiles: A) single-peaked profiles, B) central-reversed profiles and C) complex profiles (see Paragraph Mg II line profiles), as derived from IRIS spectral observations between 15:10 and 15:27 UT, with pixel size degraded to 1"$\times$ 1", are shown in the left panel. Out of all the

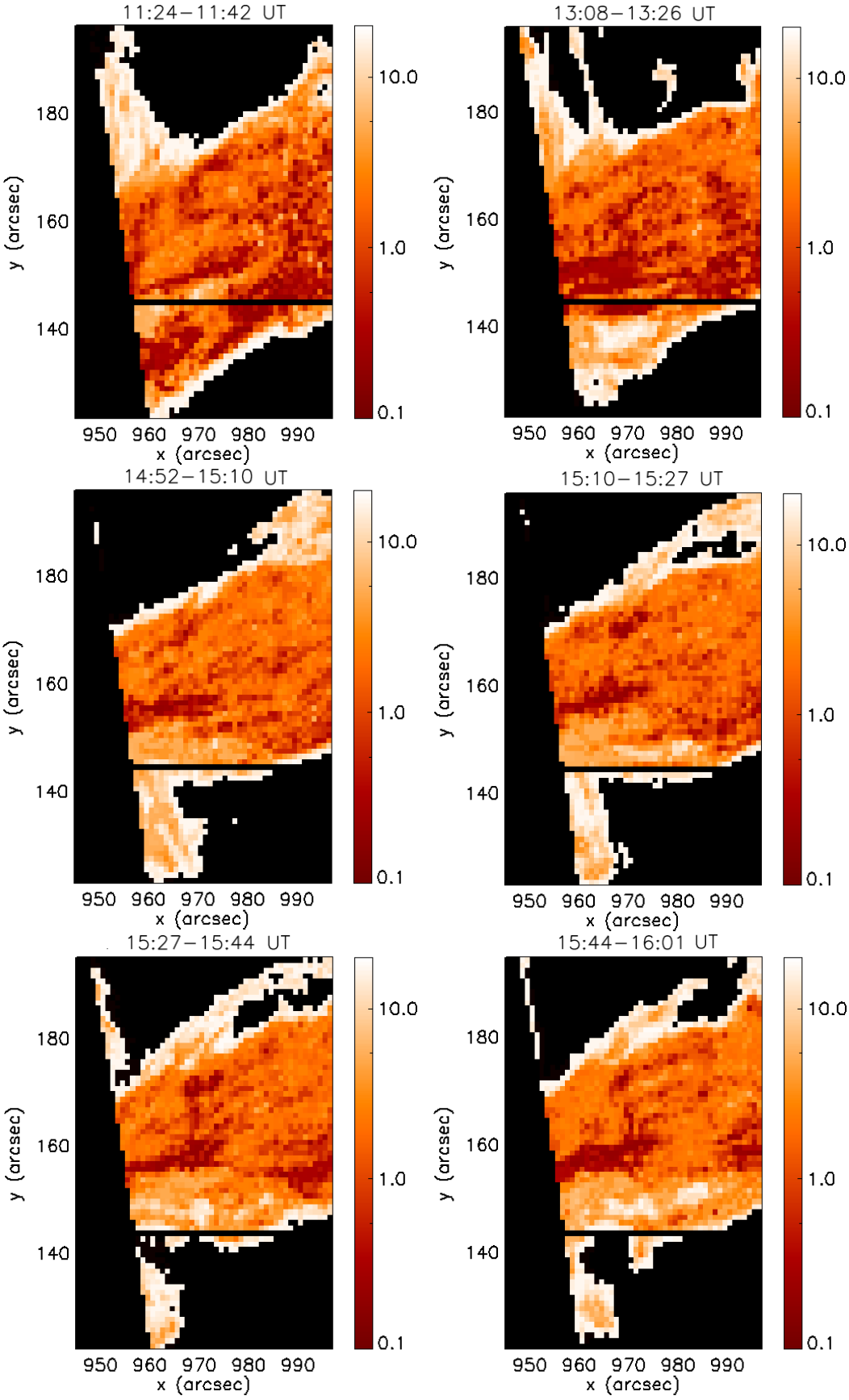

Figure 3.40 Ionization degree in the prominence higher than 10 000 km above the limb derived from IRIS spectral observations at different times on 28 May 2014. The duration of observation is shown at the top of each panel.

profiles of the prominence inside the FOV, about 60 % of the observed profiles belong to the A group, while about 38 % of the synthetic profiles from models belong to the A group. Most of the A type synthetic profiles are located in the regions close to the edges of the prominence, where the plasma is optically thin due to the lower density and higher temperature in these regions. And the regions with electron densities larger than $2.0 \times 10^{10}\,\mathrm{cm}^{-3}$ are the central-reversed profiles (B) dominated (see Figure 3.38). The fact that there are more reversed profiles from models than from observations in the central part of the prominence could be caused by the smaller turbulence velocity of $5\,\mathrm{km}^{-3}$ fixed for all the models. The inclusion of a PCTR into the isothermal and isobaric prominence slab can also slightly enhance the line center emission of the k and h lines (Heinzel et al., 2014; Heinzel, 2015).

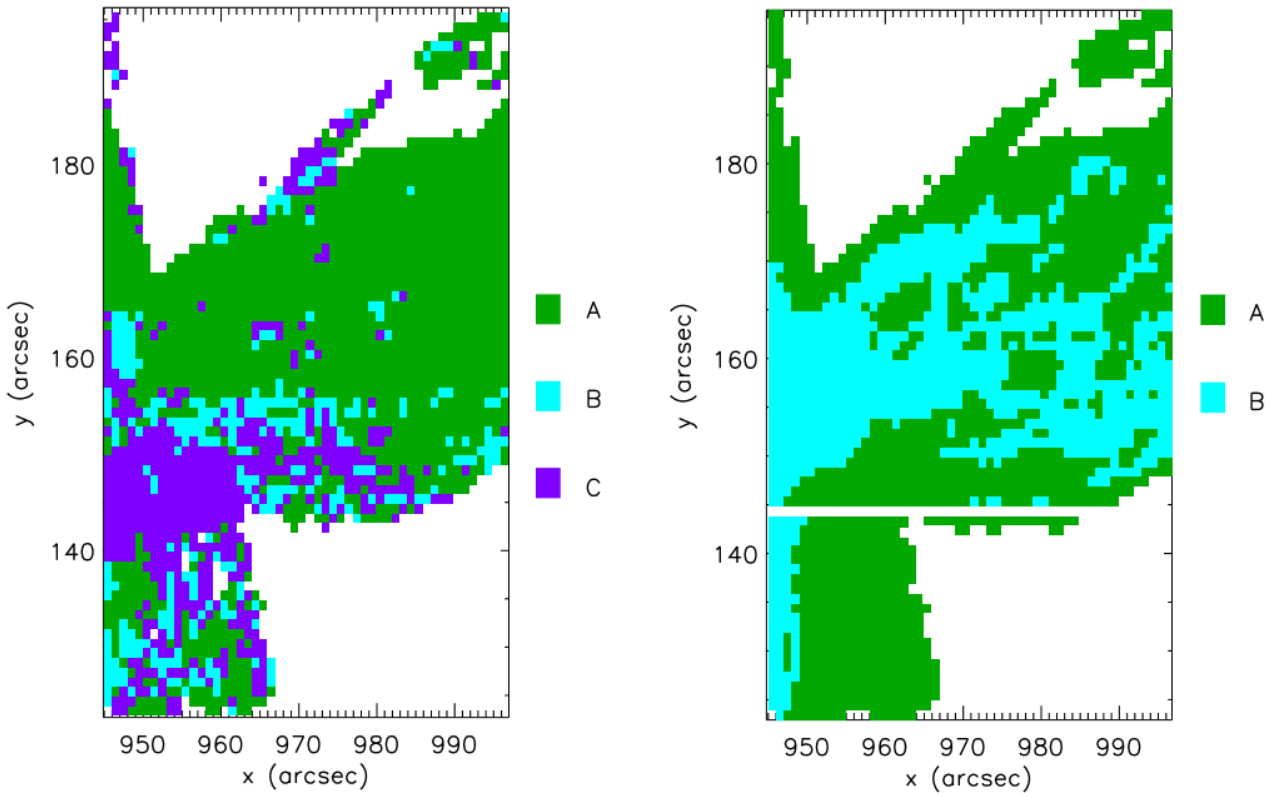

Figure 3.41 Left: The spatial distribution of the three groups of profiles in the prominence in different colors derived from IRIS spectral observations between 15:10 and 15:27 UT. Right: The spatial distribution of the profile types of the optimum models (for k and h line intensities) in the prominence between 15:10 and 15:27 UT.

3.5 Hydrogen Mass flows

Based on the 2D hydrogen density maps in the prominence body (as shown in Fig. 3.37, Fig. 3.38 and Fig. 3.39), we computed the hydrogen mass distribution by multiplying the total density by the hydrogen atom mass, the pixel area and the thickness which is assumed to be

1000 km. The total mass in the observed region of the prominence is then derived by summing up all the pixels of the prominence in each raster. We do not take into account the angle between the prominence and the POS in this computation, because this angle actually varies with fine structures and we considered that the average value is 90°.

Figure 3.42 shows how the total hydrogen mass in the observed region of the prominence changes with time. In the IRIS observation duration between 11:24 and 16:01 UT, the total hydrogen mass varies in the range of 6.3×10^{13} to 1.5×10^{14} g. It reaches a maximum around 12:43 UT, then decreases to a minimum around 15:54 UT. As only about half of the prominence is located in the FOV of the IRIS spectral rasters, the total hydrogen mass of the prominence is estimated very roughly by multiplying by 2, which leads to the range of 1.3×10^{14} to 3.0×10^{14} g and the total mass of the prominence that takes into account the mass of all the elements is about 1.8×10^{14} to 4.2×10^{14} g. This is close to the values derived in previous studies. For example, Gilbert et al. (2005) found a total mass of 6.0×10^{14} g in an erupting prominence using coronal observations in the Fe XII (195 Å) line. Schwartz et al. (2015) derived a total mass between 2.9×10^{14} g and 1.7×10^{15} g for six prominences. We also calculated the mean temperature of the prominence averaged in the same region, and the variation is shown in Fig. 3.43. It ranges from 1.10×10^{4} to 1.20×10^{4} K in the four and a half hours, which is higher than in quiescent prominences (Heinzel et al., 2014). An increase of about 600 K of the mean temperature occurs close to the beginning of the activation.

Based on the derived POS velocities, the plasmas in the FOV generally move downwards with a mean velocity which varies with time between about 1 km s^{-1} to about 4 km s^{-1}, which indicates the domination of downflows in the prominence. We estimated the mass exchanges between the prominence and the Sun by computing the hydrogen mass that crosses a layer which is set to be 10 000 km above the limb to avoid spicules. With the distribution of mass and velocity in the prominence, the derived total hydrogen mass drainage from the prominence to the solar surface adds up to 1.3×10^{13} g during the whole observation time of IRIS. The averaged drainage rate is 7.8×10^{8} g/s, leading to a drainage of 6.8×10^{13} g/day. A larger drainage rate of about 10^{15} g/day was found by Liu et al. (2012) in a prominence with more active drainage with an average downflow speed of about 30 km/s that is about ten times faster than the our prominence. The mass drainage during the whole observing duration of IRIS is about one tenth of the total mass of the prominence. Considering the significant role of the mass weight in the confinement of a magnetic flux rope, the alleviation of the mass is not negligible for the balance of the prominence and may possibly be associated with the activation of the eruption (Low, 2001).

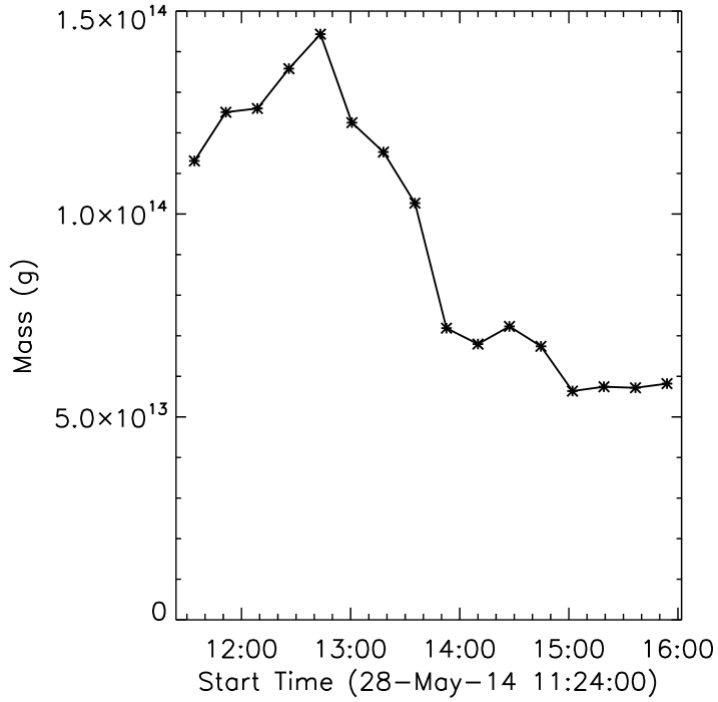

Figure 3.42 Total (hydrogen) mass of the prominence in the FOV of IRIS spectral observation as a function of time, between 11:24 and 16:01 UT.

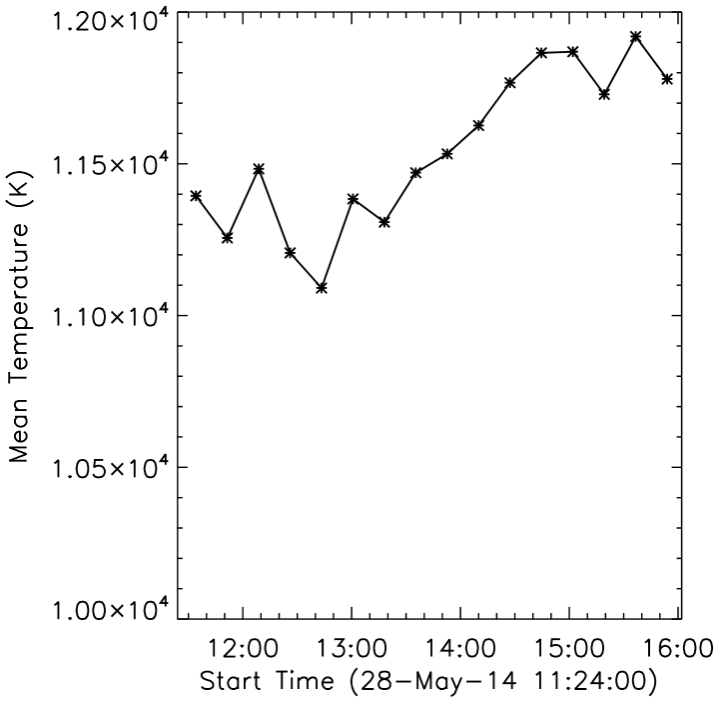

Figure 3.43 Mean temperature of the prominence in the FOV of IRIS spectral observation as a function of time, between 11:24 and 16:01 UT.

3.6 Discussion

On 28 May 2014, an erupting prominence occurred near North-West limb of the Sun. We analyzed a rather complete set of observations of the eruptive prominence, which involves IRIS, SDO, STEREO, SOHO and K-COR.

We computed the velocity pattern of the prominence. In the POS downward motions dominate in the lower part of the prominence with a mean velocity less than 5 km s^{-1} during the activation. In all the 16 IRIS rasters, Doppler redshifts dominate in the lower part of the prominence and no evidence of helical motions is found which may be caused by the limited duration of the IRIS observation. It only covers the activation phase, while the untwisting motion is not evident before the eruption.

We performed plasma diagnostics by comparing Mg II h&k integrated intensities from IRIS observations and from the NLTE radiative-transfer code PRODOP_Mg. The derived electron densities range from 1.3×10^9 to 7.0×10^{10} cm^{-3} and the derived total hydrogen densities range from 1.5×10^9 to 3.6×10^{11} cm^{-3} in different regions of the prominence. The mean temperature is around 1.1$\times$10^{4}K which is higher than in quiescent prominences.

Since the modeling starts from NLTE computations of hydrogen, once the best Mg II model was found, we were able to compute the neutral hydrogen density and consequently the total hydrogen density. We could build maps of the ionization degree (the ratio of electron density to neutral hydrogen density). The ionization degree increases at the edges of the structure and is overall in the range 0.1–10. We note that our ionization degree reaches rather lower values (down to 0.1), a result rather surprising for an activated prominence. The fact that we obtain a lower temperature (representative of quiescent prominences) and a lower ionization degree in the central parts of our prominence may mean that the activation starts in peripheral regions more prone to heating, whatever the actual process.

We could also derive the total hydrogen mass, which is in the range of 1.3×10^{14} to 3.0×10^{14} g. The total mass drainage from the prominence to the surface of the Sun during the whole observation time of IRIS is about one order of magnitude smaller than the total mass of the prominence.

We don't detect clear cavities in IRIS SJIs, since we roughly see the prominence "head-on". No evidence of helical motions is found in the Doppler velocity maps during the activation, although we detect untwisting motions in AIA observations between 18:30 UT and 21 UT. There is no clear current sheet in the density and temperature maps. The radial onset height of the PE is about 100 000 km while McCauley et al. (2015) derived an average value of 83 000 km in their study of 106 limb events.

The non-LTE modeling of Mg II k&h lines allowed us to better understand the distributions and evolutions of the plasma parameters in eruptive prominences. We plan to perform a more precise analysis of the large range of profiles, e.g. with a machine learning technique. We also plan to perform a quantitative analysis of more eruptive prominences observed with a larger FOV and longer observing times in a future research. We will also study the effects of

the 3D velocity and density structures on the NLTE diagnostic of the prominence plasma. A prominence-corona transition region will be added in our models and once the geometry of the prominences studied is well characterized, 2D NLTE models will be used.

Chapter 4

Spectral diagnostics of prominence plasma

In this chapter we mainly introduce the NLTE radiative transfer model PRODOP_Mg used in our modeling of the Mg II k and h lines and present some relationships between radiative and atmospheric quantities through one-dimentional (1D) NLTE modeling of prominences in the Mg II lines. The UV Mg II k (2795.53 Å) and h (2802.71 Å) lines are very useful for the diagnostics of the solar prominence plasma (Labrosse et al., 2010). Vial et al. (1979) obtained the first high resolution Mg II k&h spectra in an active region prominence from the LPSP UV Polychromator onboard OSO 8. The IRIS mission provides high spectral and spatial resolution imaging and spectroscopy in the Mg II h and k lines. Since its launch, a lot of results have been obtained in both observational and modeling domains (e.g. Heinzel et al., 2014; Vial et al., 2016). A systematic NLTE radiative transfer modeling is necessary to study the relationships between observed Mg II lines and plasma parameters in prominences. In this thesis we use 1D isothermal and isobaric models to study how the Mg II lines in solar prominences change with the different physical parameters in a realistic range.

4.1 Description of PRODOP_Mg

We rely on the NLTE radiative-transfer code PRODOP_Mg for our computation of the Mg II h and k synthetic spectra. PRODOP was written in the programming language FORTRAN and developed by Gouttebroze and Labrosse (2000) to solve 1D NLTE radiative transfer in solar prominences and filaments. It uses angle-averaged partial redistribution (PRD) approach for the resonance lines of hydrogen, helium and calcium. Based on the PRODOP codes, the computation of the Mg II k and h lines as well as the subordinate lines (2791 Å and 2798 Å) are included in the new version called PRODOP_Mg. Atomic parameters for magnesium have been obtained from PANDORA (Avrett and Loeser, 1992) to compute Mg II spectra in prominences. The abundance of magnesium relative to hydrogen is 3.388×10^{-5} (PANDORA,

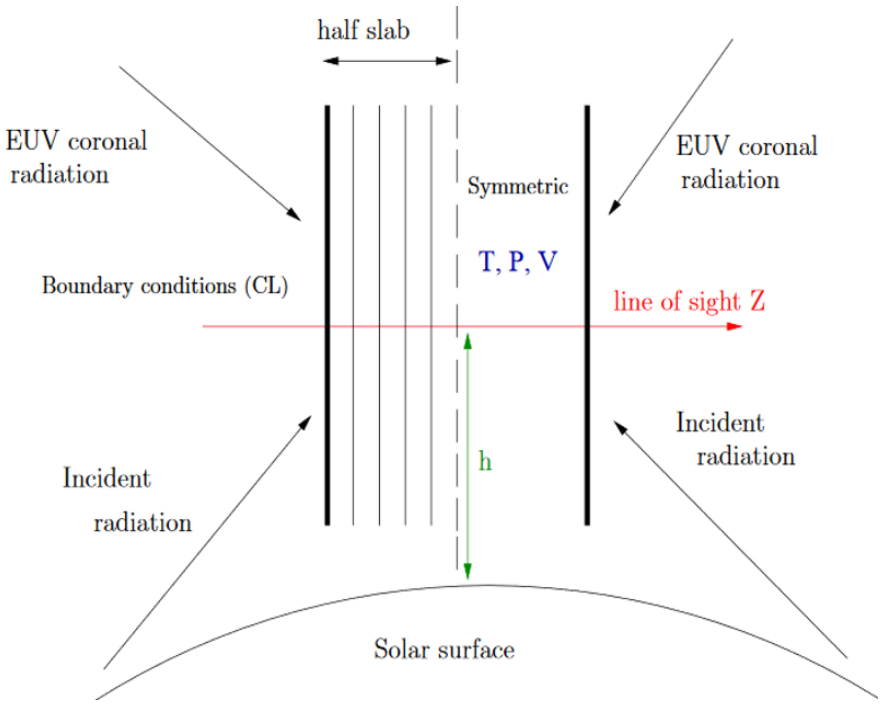

Figure 4.1 Schematic diagram showing a parallel slab standing vertically above the solar surface, illuminated by the surrounding atmosphere (Chane-Yook, 2015).

Avrett and Loeser, 1992). This code consists of plane-parallel slabs standing vertically above the solar limb (see Fig. 4.1), illuminated by the surrounding atmosphere. It solves a system of equations, e.g, the ionization equilibrium of hydrogen, the statistical equilibrium of the level populations for the atom of hydrogen, helium, calcium and magnesium, NLTE radiative transfer and other constraining equations.

There are two steps for each model. First, the NLTE modeling solves the statistical equilibrium equation for a twenty-level plus continuum hydrogen atom to derive the electron densities at all depths and the emerging intensities for the hydrogen lines. The ionization of helium is neglected in this computing. Then the derived electron density and the level populations of hydrogen are used to solve the radiative transfer equation for multilevel atom of magnesium (Figure 4.2) according to the atomic data of PANDORA (Avrett and Loeser, 1992) using the PRD approach. There are six levels (four levels of Mg II, one level of Mg I and one level of Mg III) plus continuum. The red lines represent the bound-bound transitions of the k&h lines and the subordinate lines (2791 Å and 2798 Å). The ionizations of Mg I to Mg II and Mg II to Mg III are also taken into account. This process is terminated until certain convergence criteria is met.

We used 1D isothermal and isobaric models in this study and concentrated on the properties of the Mg II k and h lines. A PCTR can be added in this modeling, but it will lead to more parameters to control in a region where the Mg II ions only exist below 15 000 K. And the thickness of the PCTR may be very different when the direction of the LOS varies ,e.g., parallel or perpendicular to the field lines (Chiuderi and Drago, 1991). Consequently, the prominence

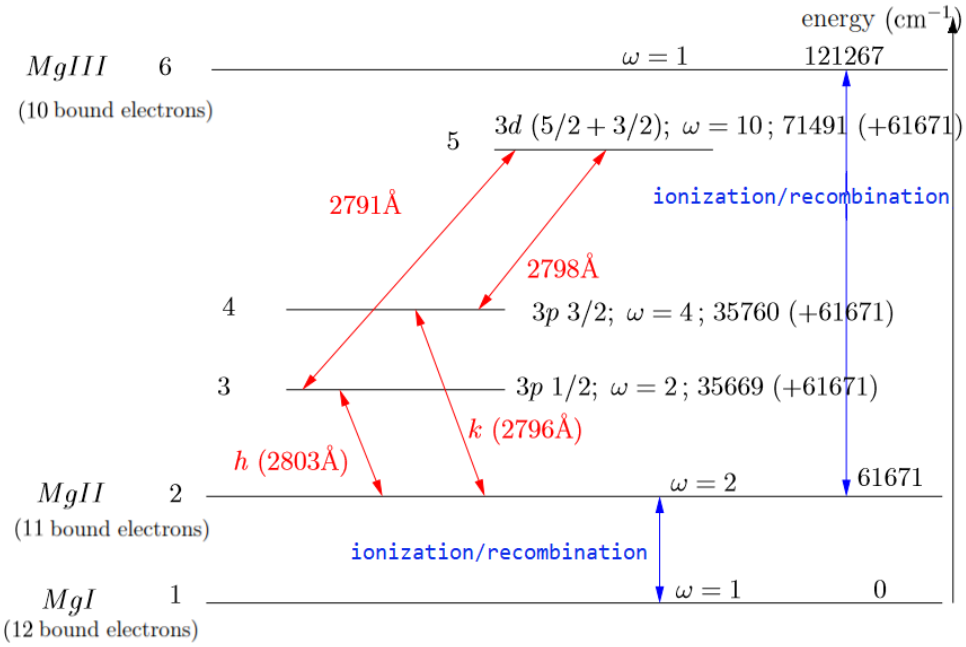

Figure 4.2 Magnesium energy diagram with four radiative transitions in red, corresponding to the k&h lines and the subordinate lines.

structure in this model consists in 1D isothermal and isobaric plasma slabs standing vertically above the surface of the Sun and illuminated by incident radiation from the surrounding solar atmosphere.

Each model is defined by five input parameters including the gas pressure, temperature, the height above the solar surface, thickness of the slab, and microturbulent velocity. The outputs are several physical parameters such as the electron density, the total hydrogen density and Mg I, II and III ground state populations, and optical quantities such as the spectral profiles and integrated intensities of hydrogen lines and magnesium lines, and their optical thickness.

With the results of the models, we want to investigate how the prominence physical parameters will affect the properties of Mg II k and h lines. For this purpose, we investigate a grid of models, obtain a range of predicted line intensities (profiles and integrated intensities) and compare with the observed IRIS profiles derived with IRIS (Chapter 3).

4.2 Grid of models

We constructed a grid of 1D NLTE models, with 7 different values in temperature (T) covering a range of 8000 to 14 000 K, 45 different values in pressure (p) covering a range of 0.005 to 0.5 $\mathrm{dyn/cm^2}$, 4 different values in thickness (D) covering a range of 200 to 5000 km, while the turbulent velocity is set to be 5 $\mathrm{km\,s^{-1}}$ and the height above the solar surface is set to be 10 000 km for all the models, as in GHV (Gouttebroze et al., 1993). We list the values of the physical quantities used for the prominence modeling in Table 4.1

Table 4.1 Grid of 1D-slab models used in this work.

1D-slab models	
T(K)	8000-14 000
p (dyn cm^{-2})	0.005-0.5
D (km)	200 1000 2500 5000
H (km)	10 000
V($\mathrm{km\,s^{-1}}$)	5

4.2.1 Boundary conditions

In the case of solar prominences modeling, the incident radiation is very important since it determines the boundary conditions for the radiative transfer equations (Heinzel, 2015). For a chosen point in the prominence above the solar surface, the incident radiation is computed by integrating all the radiation received at the point over all of the atmosphere that is visible from this chosen point (Brown and Labrosse, 2018; Sahal-Brechot et al., 1986). We compute the mean local intensity profile (in $\mathrm{erg\,s^{-1}\,sr^{-1}\,cm^{-2}}$ Å^{-1}) from IRIS observations and take into account the effect of the geometry, the active regions on solar surface, and the radial variation of the solar brightness (See more details in Chapter 3).

4.3 Results

Our objective is to find radiative signatures of the Mg II h and k lines from a grid of characteristic models. We first consider the (integrated) k and h intensities as the radiative outputs of the modeling and the (total) hydrogen and electron densities as the main physical quantities of the model, considering that the Mg II lines are formed in a (relatively) narrow range of temperatures, essentially determined by Mg II and Mg III (Heinzel et al., 2014). Secondly, we want to check if the relationship between the Hα intensity and the EM derived in HGV (Heinzel et al., 1994) could also be valid for the Mg II h & k lines. If so, it will offer a simple and supplementary tool for the diagnostic (density combined to thickness) of prominences. As a first step, the radial velocity was set to $0\,\mathrm{km\,s^{-1}}$.

The EM was computed as the integral of the square of the density over the depth in the prominence, as given in Chapter 1. It was computed for both the electron density and the (total) hydrogen density, which is the result of the hydrogen NLTE computations that are preliminary to the Mg modeling. The hydrogen density is important and is used in the computation of mass flows derived from IRIS observations (see Chapter 3). The results with different thicknesses and temperatures for both EM are shown in Fig. 4.3 for Mg II k and Fig. 4.4 for Mg II h.

There is a monotonous variation of I_k and I_h (the integrated Mg II k and h intensities) vs. the two EMs when temperature and thickness are fixed. So we only focus on I_k for now. However, both I_k and I_h information are used for comparing with observations and they can be used for further discriminating between models (Alissandrakis et al., 2018).

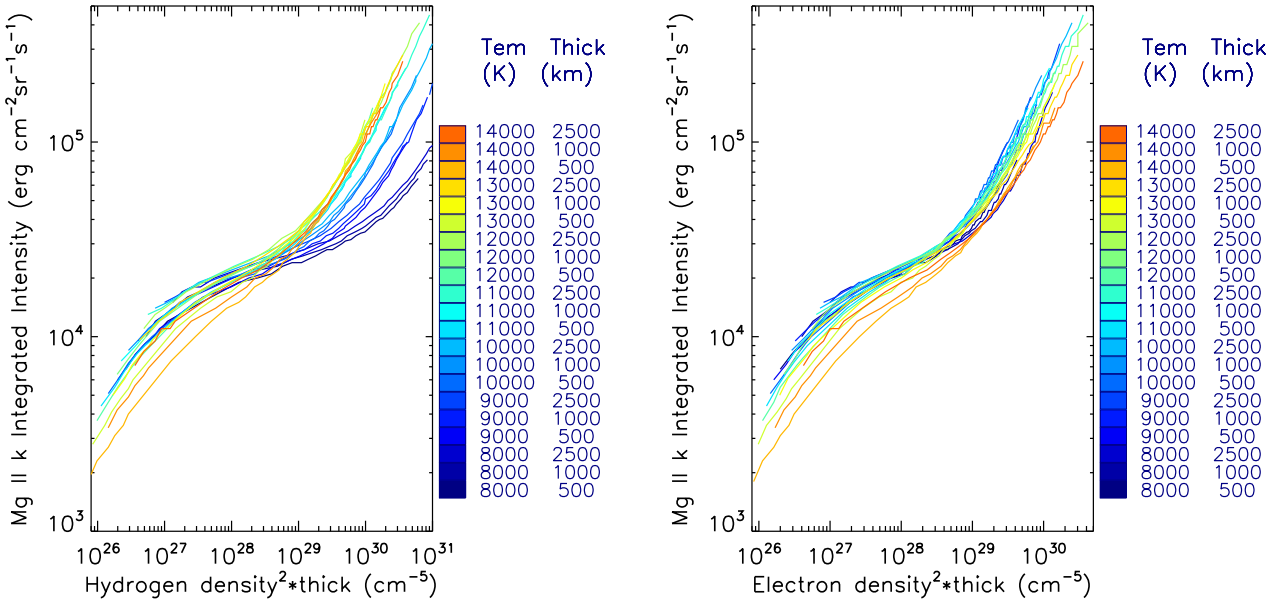

Figure 4.3 Integrated Mg II k line intensity as a function of the hydrogen EM (left) and the electron EM (right). The different colors show the different temperatures (refer to Tem in the figure) and thicknesses (refer to Thick in the figure).

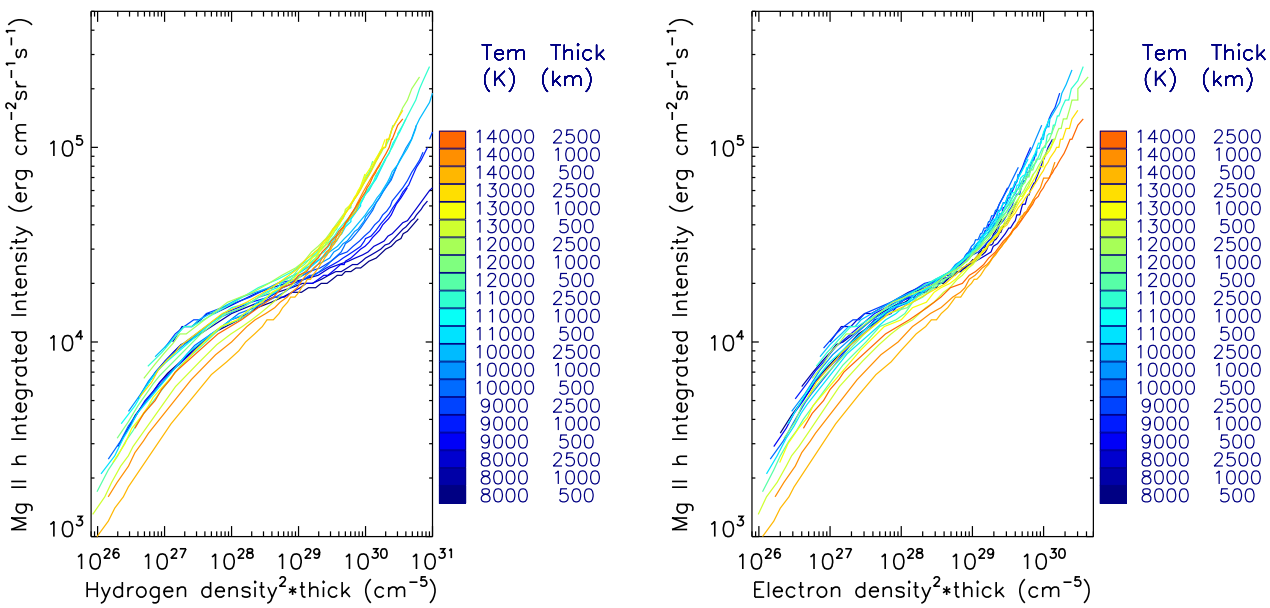

Figure 4.4 Integrated Mg II h line intensity as a function of the hydrogen EM (left) and the electron EM (right). The different colors show the different temperatures (refer to Tem in the figure) and thicknesses (refer to Thick in the figure).

We find that the integrated intensities increase with the hydrogen and electron EM, and decrease with increasing temperature in the low pressure region due to the ionization of the Mg II at higher temperatures, similar to the results obtained by Heinzel et al. (2014). At high intensities ($I_k > 4 \times 10^4\,\mathrm{erg\,cm^{-2}\,sr^{-1}\,s^{-1}}$), the curves are well separated with temperature for the hydrogen EM. This is not the case for the electron EM. In this high pressure region, the collision emission dominates over the radiative emission, and the collisional ionization is more important for higher temperatures. Around 10 000 to 11 000 K, for intensities lower than $4 \times 10^4\,\mathrm{erg\,cm^{-2}\,sr^{-1}\,s^{-1}}$, the curves seem to not depend on the thickness.

Since the NLTE computations show the importance of the incident radiation (e.g. Heinzel et al., 2014), we study the variation due to the Doppler effect of a radial velocity. When the prominence plasma moves towards or away from the solar surface in the radial direction, the incident radiation is shifted to higher or lower frequencies, which will cause variations in the emitted radiation. For the incident radiation used in our models, the distances between the line center and the peaks correspond to velocities of about 15 $\sim$ 20 $\mathrm{km\,s^{-1}}$. Figure 4.5 shows the integrated Mg II k line intensity as a function of the hydrogen EM (left) and the electron EM (right), for 0 (dashed lines) and $20\,\mathrm{km\,s^{-1}}$ (solid lines) radial velocities, for a thickness of $1000\,\mathrm{km}$. The different colors show the different temperatures (refer to Tem in the figure). We find that for a given EM, there is a slight increase in the integrated intensity I_k. For a given I_k, the EM decreases by at most a factor 2 for a velocity of $20\,\mathrm{km\,s^{-1}}$. And the effect of radial velocity (at $20\,\mathrm{km\,s^{-1}}$) disappears for electron EM above $10^{29}\,\mathrm{cm^{-5}}$, because of the domination of the collisional excitation over the radiative excitation.

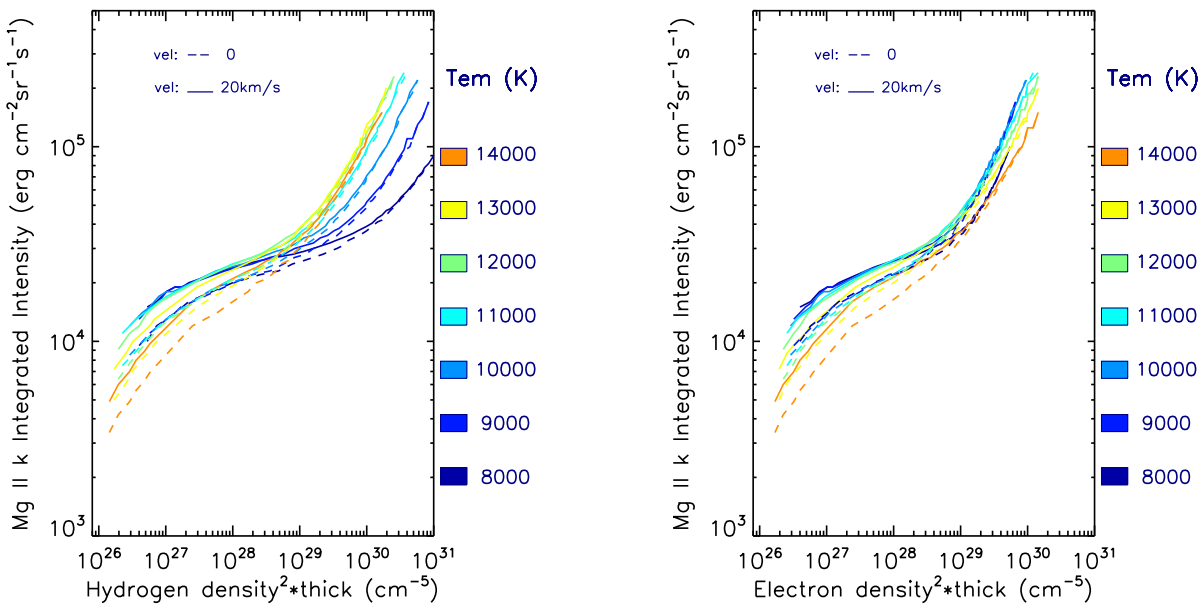

Figure 4.5 Integrated Mg II k line intensity as a function of the hydrogen EM (left) and the electron EM (right), for radial velocities of 0 (dashed lines) and $20\,\mathrm{km\,s^{-1}}$, for a thickness of $1000\,\mathrm{km}$. The different colors show the different temperatures (refer to Tem in the figure).

The integrated Mg II k (blue) and h (red) line intensities change with velocities in the range of $20-80\,\mathrm{km\,s^{-1}}$ with three different pressures (0.01, 0.1 and 0.5 dyn cm^{-2}) are shown in the Figure 4.6. The line intensities being relatively insensitive to the temperature, the value of the temperature is set to be 10 000 K. The integrated intensities with radial velocities relative to that without radial velocities for the k and h lines are shown as the blue and red lines respectively. The relative integrated intensities first increase then decrease with the velocities, and reach a maximum when the velocity is $15-20\,\mathrm{km\,s^{-1}}$, corresponding to the distance between the line core and the blue peak of the incident radiation. The deviations of the relative integrated intensities from unity increase with decreasing pressures for velocities less than $40\,\mathrm{km\,s^{-1}}$. For the low pressure of 0.01 dyn cm^{-2}, the maximum deviation from the unity reaches about 0.2. For our eruptive prominence (Chapter 3),in the lower part except in the regions close to the edges, the radial velocity is smaller than $5\,\mathrm{km\,s^{-1}}$, leading to an derivation of the integrated intensity smaller than 5 % which is negligible for the diagnostics of the physical parameters in the prominence.

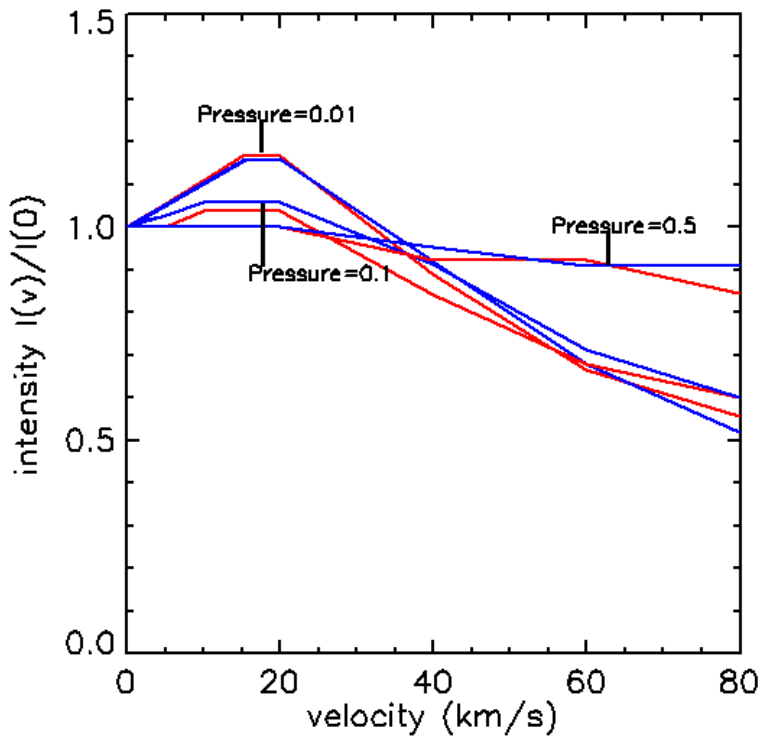

Figure 4.6 Integrated Mg II k (blue) and h (red) line intensities change with velocities in the range of $20-80\,\mathrm{km\,s^{-1}}$ with three different pressures (0.01, 0.1 and 0.5 dyn cm^{-2}) and a fixed temperature of 10 000 K.

The range of I_k values is limited by observations, e.g., for IRIS observations in a prominence in Chapter 3 (Fig. 4.7), the integrated intensities of the k line range from 1.4×10^4 and 5.0×10^4 erg s^{-1} sr^{-1} cm^{-2}, and in the central part of the prominence the values of I_k range from 1.8×10^4 and 3.9×10^4 erg s^{-1} sr^{-1} cm^{-2}. Similar values (1.8×10^4 and 3.7×10^4 erg s^{-1} sr^{-1} cm^{-2}) are

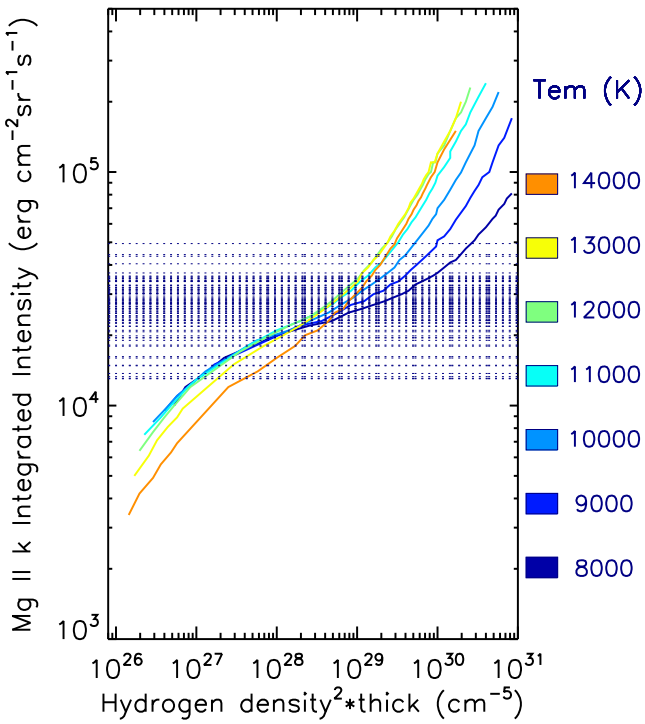

Figure 4.7 Integrated Mg II k line intensity as a function of the hydrogen EM for a zero radial velocity and a fixed thickness of 1000 km, with observed intensities from Chapter 3 (horizontal dotted lines in blue). The different colors show the different temperatures (refer to Tem in the figure).

found by Schmieder et al. (2014). A lower limit of about 8.0×10^3 erg s^{-1} sr^{-1} cm^{-2} was found by Jejčič et al. (2018) in a quiescent prominence.

The variations of I_k with the hydrogen and electron EM is also shown in Fig. 4.7, when the thickness is set to be 1000 km for different temperatures. The curves do not show strong variations for temperatures lower than 12 000 K and EM lower than 10^{29}. We set the temperature to a fixed value of 11 500 K in modeling to study the effect of the thickness variation. The curves in the left panel of Figure 4.8 show how the line intensities change with the square of the hydrogen density. The different colors correspond to different heights above the solar surface. The curves in the left panel show a strong sensitivity to the value of the thickness, which varies between 200 and 5000 km. In the right panel, there is a unique relation between the line intensity in the realistic range and the hydrogen EM for different heights and a fixed temperature of 11 500 K. These plots provide the observer a very useful tool for computing the average electron and hydrogen densities directly from IRIS spectral observations of Mg II lines. Assuming a circular cross-section, the actual thickness of the threads can be derived with high resolution SJI images from IRIS.

This means that when the altitude of the prominence plasma blob and the state of the underlying chromosphere (whether there is active region or not) are known, if observers can

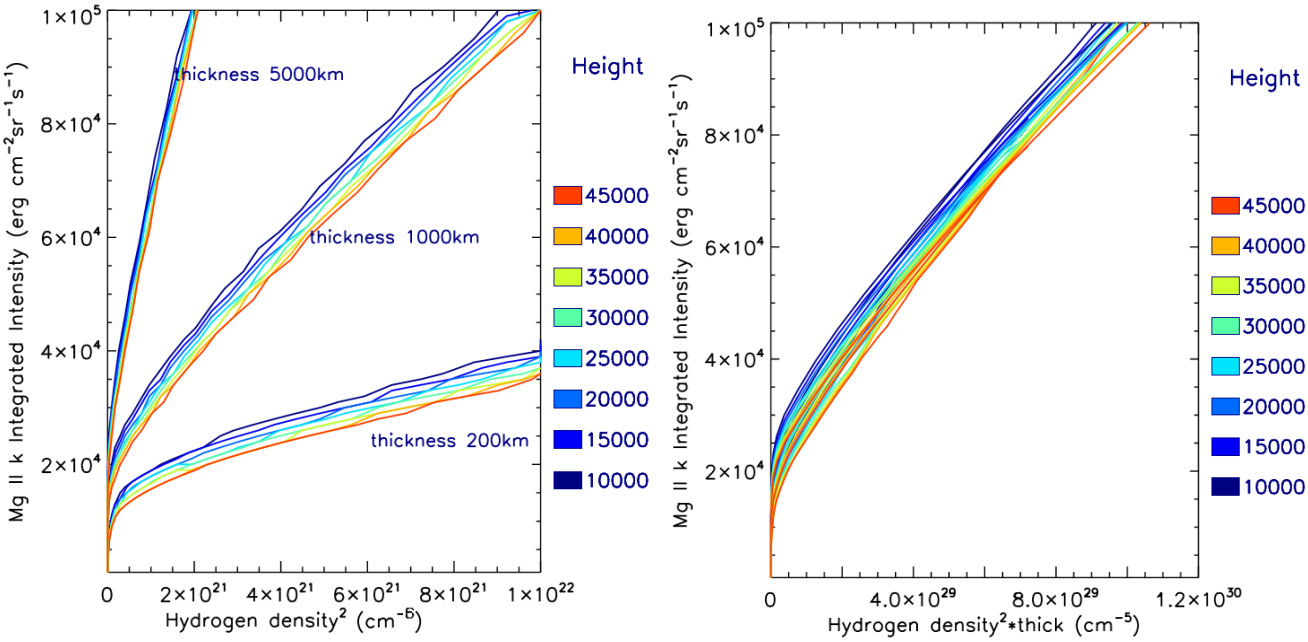

Figure 4.8 Integrated Mg II k line intensity as a function of the square of the hydrogen density for three values of the thicknesses (200, 1000 and 5000 km, left) and as a function of the hydrogen EM (right). The different colors show the different heights above the solar surface.

derive the POS velocity and the thickness of the blob from observations, they can rely upon a unique relationship between the measured I_k (or I_h) and the hydrogen and electron EMs to derive the hydrogen and electron densities with assumed typical values of microturbulence and temperature. The derivation of the densities is rather accurate assuming a filling factor of 1. The filling factor can also be derived through a ratio of spectral lines sensitive to density.

Actually, this relation also can be used in the reverse way. Heinzel et al. (1996) obtained the electron density from polarimetric measurements in Hα and He I D3 lines and from the theoretical correlation of the EM with the Hα integrated intensity (GHV), then they derived a large range of "effective" thicknesses. They also concluded that the total column mass in the direction normal to the prominence slab is fairly constant.

It should be noted that the unique relations between the Mg II line intensity and the hydrogen EM are only valid when the temperature is higher than 11 000 K. When the temperature is lower, the curves vary with different thicknesses, as shown in Figure 4.9. And the densities can be derived relying on these relations.

The combination of Mg II line intensity and the k/h ratio can provide some information on the estimation of the temperature range. The left panel in Figure 4.10 shows how the k/h ratios change with k line intensities at different temperatures. The scattered points in different colors represent the results from 888 isothermal and isobaric models with a fixed thickness of 1000 km and a fixed turbulence velocity of 5 km/s. For each temperature, the variation of k/h ratio with the k line intensity can be approximated by a curve through fitting procedure, as shown in the right panel in Figure 4.10. The fitted curves for each temperature from 7000 K to 15000 K are

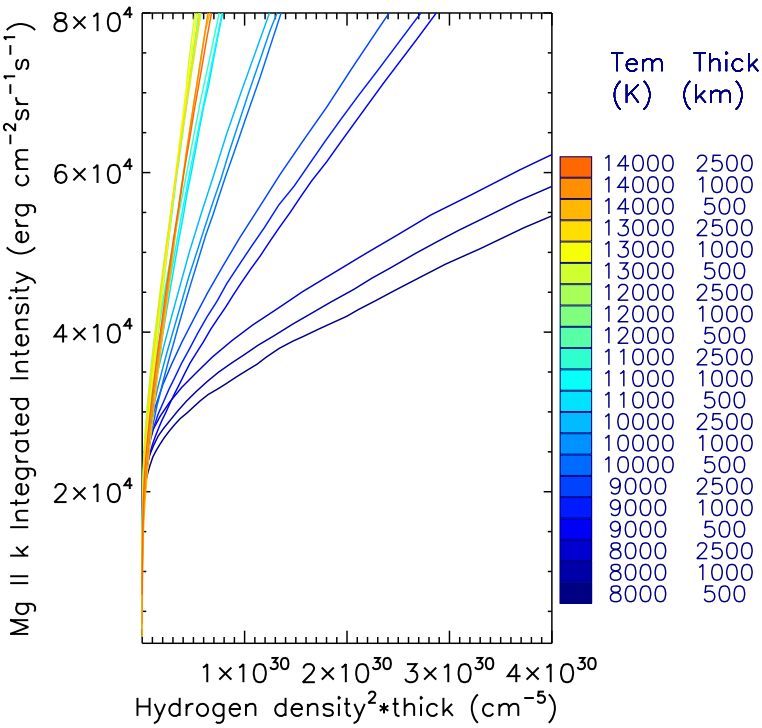

Figure 4.9 Integrated Mg II k line intensities change with the hydrogen EM. The different colors represent different temperatures and thickesses.

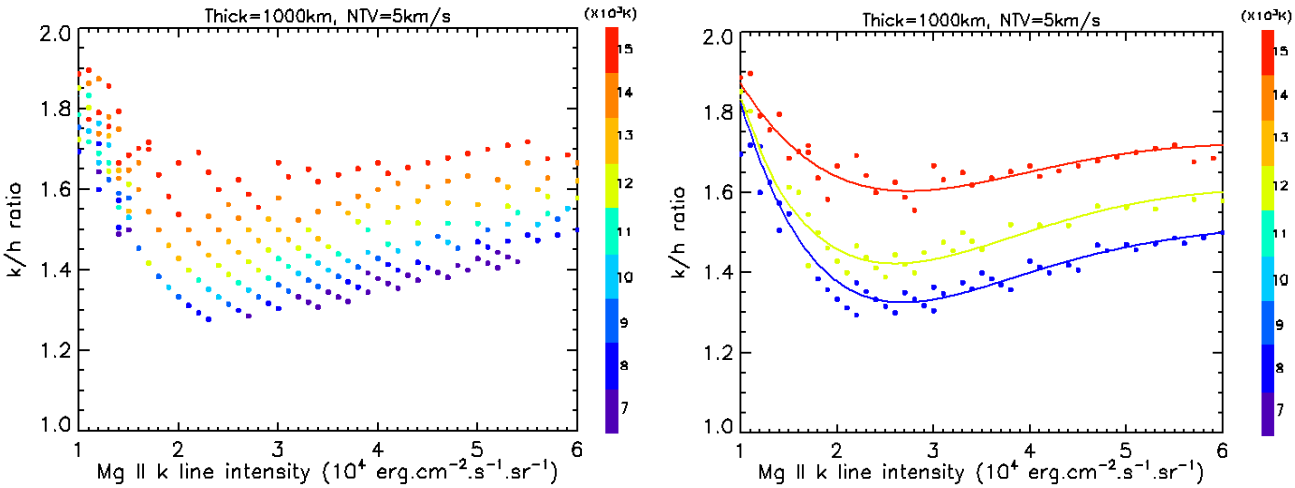

Figure 4.10 The left panel shows how the k/h ratios change with k line intensities at different temperatures. The scattered points in different colors represent the results from 888 models. The right panel shows the variation of k/h ratio with the k line intensity as approximated by a curve through fitting procedure.

shown in Figure 4.11. These curves can help estimate the temperature range of a prominence blob with the computation of the Mg II k line intensity and the corresponding k/h ratio.

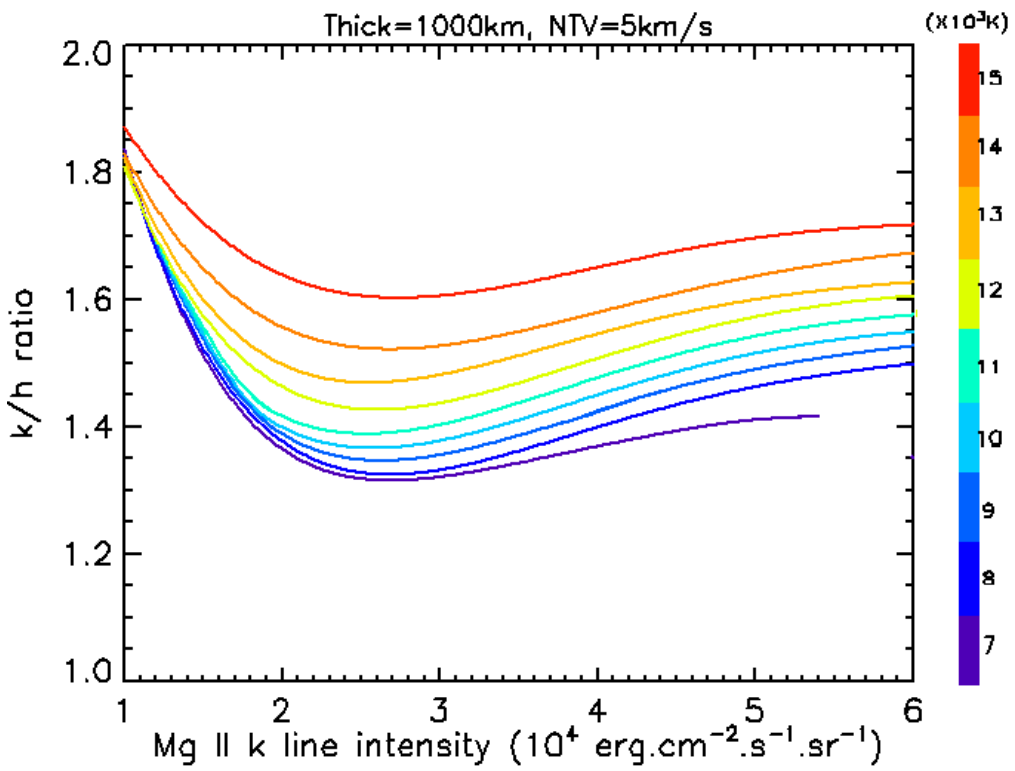

Figure 4.11 The curves in different colors represent the variations of k/h ratios with the k line intensities approximated through fitting procedure at different temperatures.

This means that for a prominence plasma blob, observers can rely on the combination of the relationship between the measured I_k and the hydrogen and electron EMs and the relationship between the measured I_k and the k/h ratios to estimate the hydrogen densities, electron densities and temperatures with measured height above the solar surface, the POS velocity and the thickness from observations as well as the assumed typical values of microturbulence.

4.4 Conclusion

We performed the Mg II 1D modeling to derive prominence plasma properties through the pixel-per-pixel spectro-imaging from IRIS. We used the most accurately computed incident radiation of Mg II k and h lines. Depending on the altitude of the prominence, these profiles are derived from the point-per-point emission of all areas within the horizon of the prominence. The incident radiation used in this work comes from quiet regions of the Sun. This means that it applies to quiescent prominences only.

Although we computed the full profiles of the Mg II lines, we focused on the integrated k and h intensities as it has been done with the hydrogen lines by HGV.

Since the Mg II k and h intensities as a function of EM have the same behavior, we focused on k only. We found that the k intensity increases with the hydrogen and electron densities. The correlation does not change much when a radial velocity of $20\,\mathrm{km\,s^{-1}}$ is added. Because of the Doppler dimming effect, velocities of the order of $300\,\mathrm{km\,s^{-1}}$ could change the emitted radiation by a factor 5 (see Heinzel, 2015).

The same behavior takes place between the k intensity and the EM. This is valid for both electron and hydrogen densities. Such a correlation is relatively insensitive to temperature, thus the density can be derived with a good accuracy with the determination of the geometrical thickness.

As a conclusion, we think that the correlation found for Mg II k (and h) intensity is a very useful complement to a similar correlation found for the Hα line of hydrogen (HGV). Although the modeling can be improved in many aspects (e.g. with 2D models), our results should be useful to prominence observers and analyzers, working presently with IRIS and in the future with the planned CLASP 2 experiment.

Chapter 5

Two weeks as an IRIS planner

Planning of the observations is critical and necessary to achieve the scientific objectives of IRIS. Because of the narrow FOV of the spectrograph, the complexity of operating the instrument and the extremely variable nature of the targets, science observations can not be simply decoupled from the planning, as can be done in many space telescopes. For these reasons, the most effective approach is to train selected scientists as Science Planner to perform the planning for a number of weeks in close cooperation with the IRIS team [1]. During these periods IRIS planners can execute their own science observations as well as the regularly scheduled calibration/synoptic and coordination programs [1].

After submitting a proposal in response to the 3rd ESA Announcement of Opportunity for the participation in the NASA-led IRIS mission [1], with the role of Science Planner, published in April 2017, I was appointed as Science Planner for the IRIS mission for a period of one year and ran the IRIS instrument for 2 weeks: from Dec 12 2017 to Dec 18 2017 and from Mar 27 2018 to Apr 2 2018. I was required to travel to the "Lockheed Martin Solar and Astrophysics Laboratory" – LMSAL (Palo Alto, CA) one week before my first planning week to learn the operation of the instrument because I had no previous experience in IRIS planning. The training and first-time planning was at LMSAL and subsequent planning was done remotely from Institut d'Astrophysique Spatiale (IAS, Orsay).

5.1 The daily plan

5.1.1 Calibration and Coordination

IRIS science planning involves the daily science plan for the coordinated observing programs (in particular with Hinode and ground-based observatories) as well as regularly scheduled calibration programs (ITN 8; all the related ITN documents are stored in the IRIS website [2]). In addition, I have the possibility to run my own science observing programs during my planning

[1] https://www.cosmos.esa.int/documents/
[2] http://iris.lmsal.com/documents.html

weeks. The calibration and synoptic observing programs are listed in the IRIS calibrations and synoptic observations calendar [3]. There are regular calibration programs with designated observing lists (OBS), such as A1 QS monitoring, B1 AR tracking from limb to limb and B2 QS region tracking from limb to limb at the same μ value as the AR. IRIS operations are included in certain Hinode Operation Plans (HOPs), and they appear in the Hinode Monthly Events page [4] as one of "other participating instruments".

The completed plans are uploaded to the IRIS mission from Monday to Friday. The Monday to Thursday timelines cover a period of 24 hours,while the Friday timeline covers a period of 72 hours. The timelines start from 4 UT the next day. For example, the Monday timeline covers from 4 UT Tuesday to 4 UT Wednesday (ITN 8). Hinode executes three weekly timelines covering from Tue 10 UT to Thur 10 UT, from Thur 10 UT to Sat 10 UT and from Sat 10 UT to Tue 10 UT in the normal operations mode (ITN 8). Therefore, for coordination with Hinode, given their different weekly schedules, the Hinode planners should be notified two days in advance about the general information of the pointing and the observing mode. In my planning weeks, I sent emails which contain the tentative IRIS observing plans to the Hinode planners on Sunday, Tuesday and Thursday before 5 pm Pacific Daylight Time (PDT) (0 UT next day). For example, the following is the tentative plan I sent to Hinode planners on 14 Dec 2017:

Here is the tentative IRIS observing plan for 2017-Dec-16 - 2017-Dec-18. IRIS is now in eclipse season, with less than 70 minutes of continuous observations every orbit.

IRIS will continue to run HOP 307 on the AR now located near the East limb. IRIS will continue coronal jet study (OBSID 3600102856) on bright points in a coronal hole.

2017-Dec-16 (starting at 04:00 UT)
- 3 orbits of calibrations
- HOP 307: AR tracking from limb to limb (OBSID 3610108077)
- Prominence study (OBSID 3610263443,3610263452, 3610263454)

2017-Dec-17 (starting at 04:00 UT)
- 2 orbits of calibration
- HOP 307: AR tracking from limb to limb (OBSID 3610108077)
- Coronal jet study (OBSID 3600102856) on bright points in a CH

2017-Dec-18 (starting at 04:00 UT)
-10 orbits of calibration
-HOP 307: AR tracking from limb to limb (OBSID 3610108077)

[3] http://iris.lmsal.com/operations.html
[4] http://www.isas.jaxa.jp/home/solar/hinode_op/hinode_monthly_events.php

-Coronal jet study (OBSID 3600102856) on bright points in a CH

When Hinode is in normal operations mode, the uploaded Hinode timelines are usually sent to IRIS planner before 5 UT on Tuesday, Thursday and Saturday (ITN 8). For example, the following is the final SOT plan I received from the Hinode planner Thomas.J.Cruz on 16 Dec 2017 at 4 UT:

The final SOT timeline to be uploaded on 2017/12/16 covers the period from 2017/12/16 10:43:00 UT to 2017/12/19 12:25:00 UT. SOT continues to support HOP 336 with other Hinode instruments and with IRIS on 12/18 as previously reported. SOT supports HOP 336 Cycle 25 Bright Points with XRT, EIS, and IRIS on 12/18 starting at 10 UT for 3 hours in the Northern Hemisphere (SOT pointing: (-40,640) tracking at 2017/12/18 10:00:00), followed by Southern Hemisphere pointing starting at 21 UT (SOT pointing: (-38,-701) tracking at 2017/12/18 21:00:00). SOT spends the remainder of the time in this 3-day weekend plan observing the plage region (formerly AR 12691). The current SOT pointing offset of (20,31) has been used to calculate pointing coordinates.

Plage Region (was AR12691) (2017/12/16 10:57:00 - 2017/12/16 18:14:35)
SOT pointing: (-90,-104) tracking at 2017/12/16 10:53:00
- SP01 (0x017f) Fast map, 230"x164", Q65, 1-side CCD at 2017/12/16 10:57:00
- SP05 (0x0145) Normal Map 246 x 164 arcsec, one side at 2017/12/16 14:00:00

⋮

HOP 336 Northern Hemisphere (2017/12/18 10:04:00 - 2017/12/18 14:59:35)
SOT pointing: (-40,640) tracking at 2017/12/18 10:00:00
- SP02 (0x01ce) Normal 320"x82", 1 side, Q75 at 2017/12/18 10:04:00

⋮

HOP 336 Southern Hemisphere (2017/12/18 21:04:00 - 2017/12/18 23:59:35)
SOT pointing: (-38,-701) tracking at 2017/12/18 21:00:00
- SP02 (0x01ce) Normal 320"x82", 1 side, Q75 at 2017/12/18 21:04:00

The received Hinode timeline should be checked to implement and optimize the IRIS timeline for its coordination with Hinode and ground-based observatories. Sometimes the targeting of requested observations, especially for small scale and short lived features such as bright points (BPs), may be discussed and adjusted before and during the planning. In this case the pointing information needs to be rechecked and confirmed before submitting

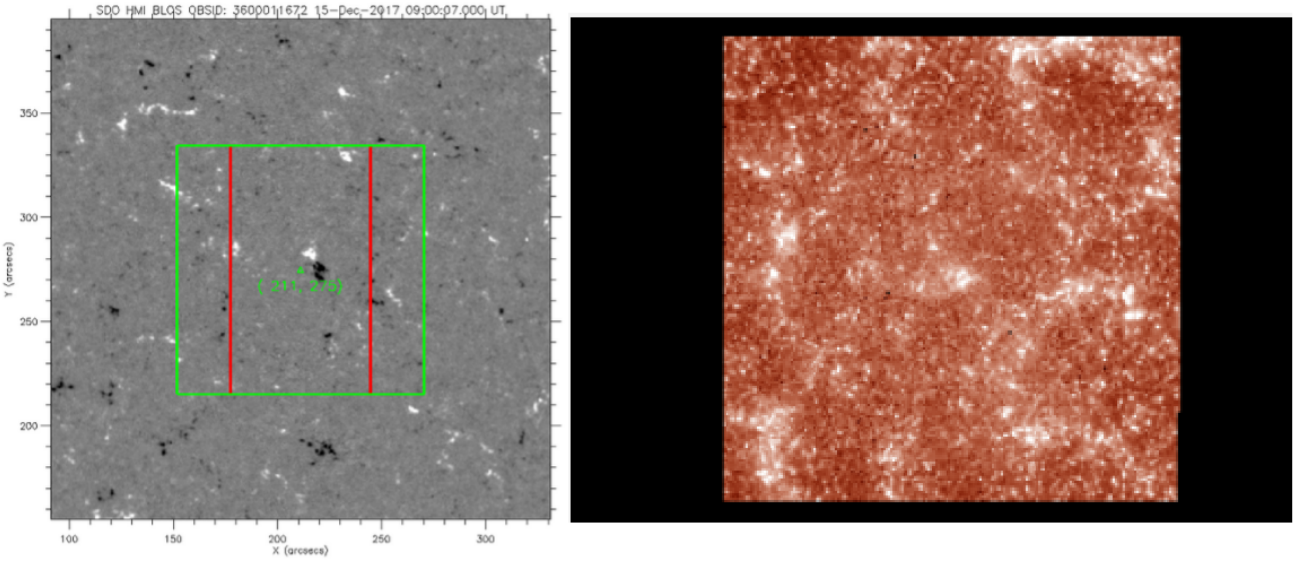

Figure 5.1 Left: The pointing preview that shows up on the IRIS web after submitting the timeline on Dec 14. The SDO/HMI magnetogram in this panel at 09:00 UT on Dec 15 is derived by adding solar rotation to the latest magnetogram obtained when the observation is being planned. The green box shows the FOV of the planned IRIS SJI observation, and the red lines show the left and right boundary positions of the slit raster. Right: The IRIS SJI image observed at 09:30 UT on Dec 15 in 1330 Å.

the plan. For example the observation HOP 335 which starts at 08:05 UT on Dec 15 2017 requires Hinode and IRIS co-observations of coronal BPs. The several pointing requests were received from Dec 12 to Dec 14 and the final pointing was determined several hours before the submission, because of the disappearance of the initially chosen targets. The left panel in Fig. 5.1 is the pointing preview that shows up on the IRIS web [2] after submitting the timeline on Dec 14. The planned IRIS large dense 192-step raster observation lasts from 07:23 UT to 09:54 UT on Dec 15. The corresponding SDO/HMI magnetogram is derived by adding solar rotation to the latest magnetogram obtained when the observation is being planned. The green box shows the FOV of the planned IRIS SJI observation, and the red lines show the left and right boundary positions of the slit raster. A small magnetic bipolar is located close to the center of the FOV. The right panel in Fig. 5.1 is the IRIS SJI image observed at 09:30 UT on Dec 15 in 1330 Å. The coronal BP is located at the center of the FOV as planned with a slit crossing at this time. The timing, pointing and the choice of OBS meet the requirements for the IRIS observation in HOP 335.

The IRIS planner meeting takes place at 13:00 PDT (20:00 UTC) on Wednesday every week. During this meeting the IRIS planner needs to introduce IRIS science plan and calibration programs planned so far this week to all the members of IRIS science team including the IRIS planner of the following week. The upcoming observations of the current week and the observing priorities of the following week are also discussed in this meeting. The following is

my notes of the IRIS planner meeting on March 28 2018:

Solar conditions so far: no active regions on disk, a new AR will be close to the East limb on Mar 29 (approximate (-948", -135") at 15:18 UT on Mar 29th), no good targets for filament observations. There is a large low latitude coronal hole on disk.

Observations so far this week: Coronal Hole/Quiet Sun boundaries studies, spicule studies at north, south pole and west limb, HOP 312 coordination with Hinode (QS 45 degree west and 75 degree west).

Upcoming observations: several programs on the new AR close to the East limb.(HOP 306 and very large sit and stare observation). Coordination with ALMA:1 April 2018 13:45 -19:30 UT (target: polar coronal hole, coordinates will be sent until 00:30 UT 30 March).

Calibrations so far this week: calib 9 wedge motor and calib 14 wobble (zero roll).

Upcoming Calibrations: C1: North/South Pole, Calib 4: Focus, F1: Mid latitude scan (HOP 336).

Observations next week priority to: 1) Coordination with ALMA; 2) AR track.

5.1.2 Timeline

The operations of the IRIS instruments are controlled by the timeline software. It contains a package of commands for the operation of the instrument and spacecraft. With the timeline, IRIS is able to perform the following operations (ITN 1):

Point the telescope to a position on (or off) the solar disk

The pointing tool of the timeline provides the latest observations in different passbands from satellites and ground-based observatories [3]. These observations are very significant for the determination of the pointings in specific programs, especially for small-scale targets and coordinated observations. For example flare watch observations require the telescope to precisely follow the most active PILs of the active region with the use of the SDO/HMI magnetogram in the pointing tool. The tracking observations of CHs that are visible as dark areas in the solar corona as observed in EUV are planned with the help of SDO/AIA 193 Å images. The left panel in Fig. 5.2 shows the pointing preview of a planned active region large sparse 64-step raster observation that lasts from March 31st 21:49 UT to April 1st 04:28 UT. It shows up on the IRIS web [3] after submitting the timeline on March 31st 2018. The SDO/HMI magnetogram in this panel that corresponds to the beginning of the planned observation is derived by adding solar rotation to the latest magnetogram obtained when the observation is being planned. The green box shows the FOV of the planned IRIS raster observation, and the red lines show the left and right boundary positions of the slit raster. The PIL of this AR is located in between the red lines and close to the center of the green box. The right panel shows the IRIS SJI observed at 00:54 UT on April 1st in 1330 Å. The brightening loop of the

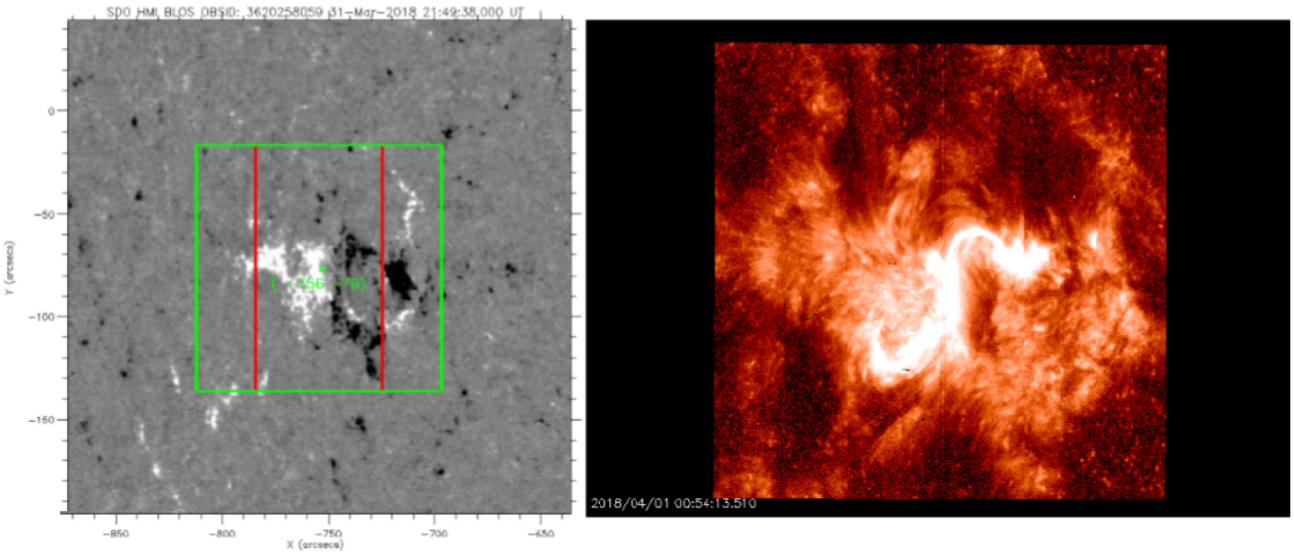

Figure 5.2 Left: The pointing preview shows up on the IRIS web after submitting the timeline on March 31st 2018. The SDO/HMI magnetogram in this panel that corresponds to the beginning of the planned observation which lasts from March 31st 21:49 UT to April 1st 04:28 UT is derived by adding solar rotation to the latest magnetogram obtained when the observation is being planned. The green box shows the FOV of the planned IRIS raster observation, and the red lines show the left and right boundary positions of the slit raster. Right: The IRIS SJI observed at 00:54 UT on April 1st in 1330 Å.

GOES B 1.1 flare whose peak time is around 00:54 UT is located around the center of the image and the slit at the center of each image crosses the flare region during the observation.

When planning on observing a target that is currently behind the east limb, the future pointing of the targets can be determined by using `STEREO_POINTING.pro` (Harry Warren, 2010) in SSW package. I used this tool for my planning of the prominence observation which lasts from 07:01 UT to 07:52 UT on Dec 14. Part of the prominence is located at the east limb when the observation is being planned, while the other part to be observed is still behind the limb. With the use of the `STEREO_POINTING.pro`, we can determine the future pointing of the prominence, as shown in Fig. 5.3. The left panel is a STEREO/EUVI full-disk image in 304 Å taken at 16:15 UT on Dec 13. A long filament is observed across the east limb. The feature that will appear at the limb at 07:27 UT on Dec 14 is marked in red in this panel, and the corresponding coordinates are shown in the middle panel. The right panel is the IRIS SJI image observed at 07:10 UT on Dec 14 in 2796Å in which the prominence is exactly in the FOV as planned.

Switch on or off solar tracking

When the tracking is on, solar rotation is continuously compensated for so that the same region is kept within the FOV (ITN 1). Based on the requirements of different observations, IRIS planner can define in the timeline whether the region that is being observed should be tracked

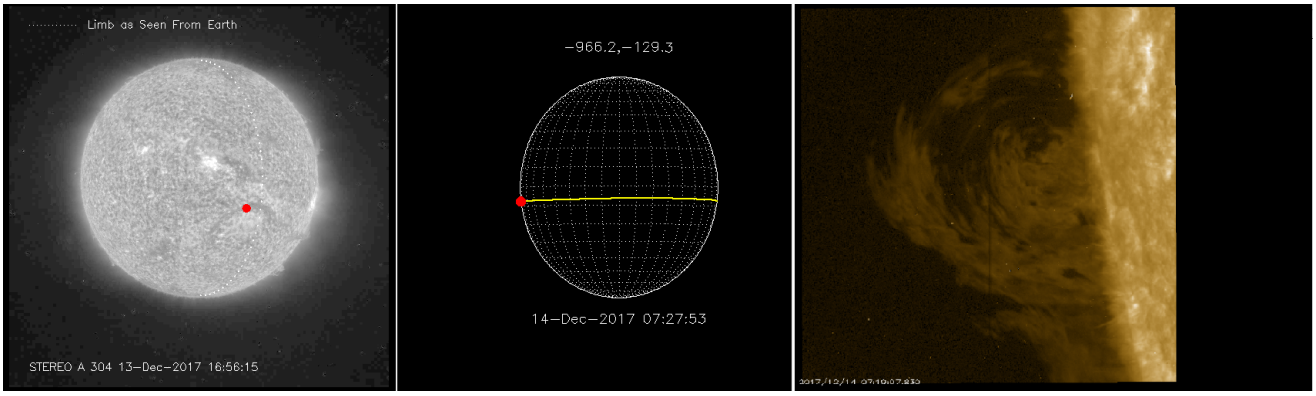

Figure 5.3 Left: A STEREO/EUVI full-disk image in 304 Å taken at 16:15 UT on Dec 13. The feature that will appear at the limb at 07:27 UT on Dec 14 is marked in red in this panel, and the corresponding coordinates are shown in the middle panel. The right panel is the IRIS SJI image observed at 07:10 UT on Dec 14 in 2796 Å.

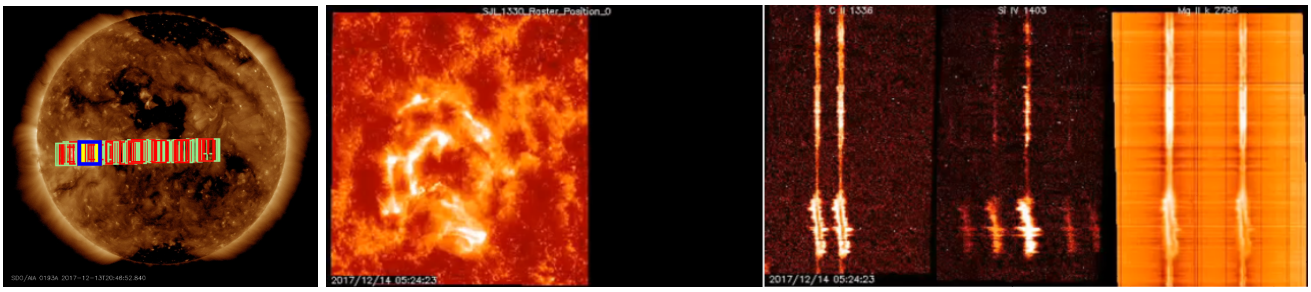

Figure 5.4 Left: An AR tracked as it crosses the disk. The full disk image of the Sun is taken on Dec 13 by AIA in 193 Å. The green boxes correspond to the FOV of the HOP 307 very large dense 320-step raster observations of IRIS, and the red lines show the left and right boundary positions of the slit rasters. Middle: IRIS SJI image whose FOV is marked in blue in the left panel observed at 05:24 UT on Dec 14 in 1330 Å. The slit is crossing the flare region at this time, and the corresponding spectra of C II, Si IV and Mg II lines are shown in the right panel.

or not. For example for coordination observation HOP 307 which tracks an AR from limb to limb and needs observations over 14 consecutive days, solar rotation tracking is required to determine the long term evolution of the magnetic field, the chromosphere and the transition region of the AR. The left panel in Fig. 5.4 shows the AR tracked as it crosses the disk in my first planning week. The full disk image of the Sun is taken on Dec 13 by AIA in 193 Å. The green boxes correspond to the FOV of HOP 307 very large dense 320-step raster observations of IRIS, and the red lines show the left and right boundary positions of the slit rasters. Each observation lasts at least one orbit, and the cadence is less than 8 hours. The middle panel in Fig. 5.4 shows the IRIS SJI image whose FOV is marked in blue in the left panel observed in 1330Å at 05:24 UT on Dec 14. Two brightening ribbons of a GOES B1.1 flare are observed from 05:24 UT to 06:23 UT. The slit is crossing the flare region at this time, and the corresponding spectra of C II, Si IV and Mg II lines are shown in the right panel.

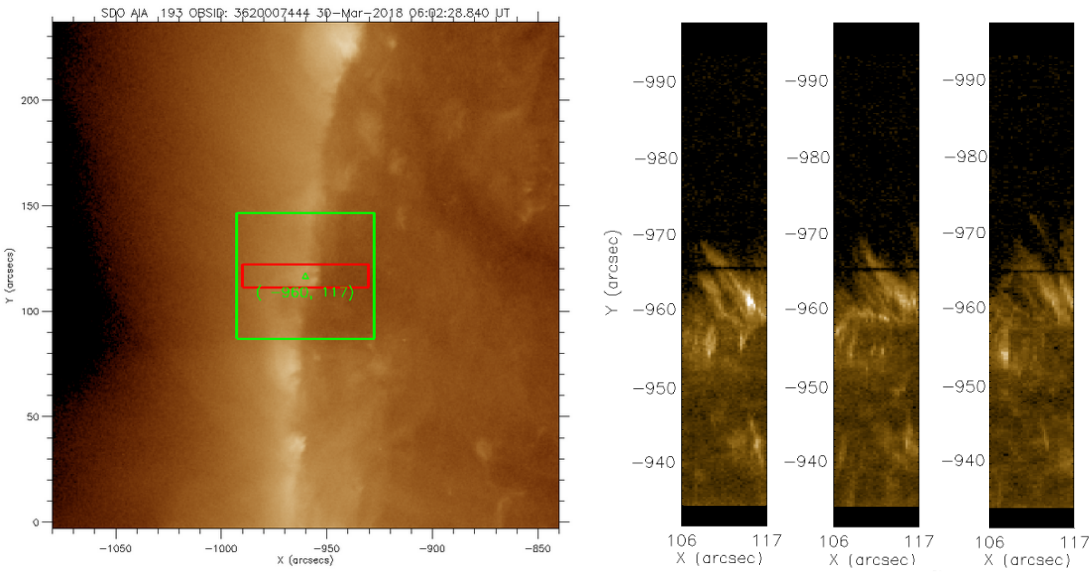

Figure 5.5 Left: The planned FOV of IRIS SJI observation marked with green in the SDO/AIA 193 Å image. The red lines correspond to upper and lower boundaries of the slit. Right: The monochromatic images in 2795.86 Å derived from the IRIS spectral observations from 06:06 UT to 06:14 UT.

Correct for orbital wobble

As IRIS is orbiting the Earth, the thermal variation produces deformations of various structures in the instrument and spacecraft, then leads to pointing differences between the main telescope and the guide telescope, consequently causes a drift of the observed image which is called “orbital wobble” (Wülser et al., 2018). It can be corrected for by setting the appropriate orbital wobble table ID (0 means no wobble table used) in the timeline software during the planning (ITN 1).

Roll the IRIS telescope

Normally the slit is oriented along the rotation axis of the Sun (N-S). And it can be rolled to other directions according to the observing requirements. For example for the spicule observation from 06:06 UT to 07:05 UT on Mar 30 in 2018 at the east limb, the slit is oriented along the E-W direction with a roll of -90°. The left panel in Fig. 5.5 shows the planned FOV of IRIS SJI observation marked with green in the SDO/AIA 193 Å image. The red lines correspond to upper and lower boundaries of the slit raster. The monochromatic images in 2795.86 Å derived from the IRIS spectral observations are shown in the right panel. The temporal variation of a selected spicule can be found in these three consecutive raster observations from 06:06 UT to 06:14 UT.

OBS ID parent	Description
0-100	Basic raster type (sit-and-stare, rasters, ...)
0-2,000	SJI choices
0-12,000	Exposure times
0-220,000	Summing modes (applied to FUV, NUV, SJI)
0-750,000	FUV summing modes
0-4,000,000	SJI cadence
0-10,000,000	Compression choices
0-180,000,000	Linelists
3.8-4 billion	OBS table generation number

Figure 5.6 OBS ID numbering scheme (ITN 31).

Execute previously uploaded OBS

The observing lists (OBS) determine the observing time, exposure time, compression, piezo-electric transducer (PZT) offset, focus, slitjaw bandpass, repeat count and cadence, etc (ITN 1). The PZT offset can change the way that the light passes through the slit of the telescope by adjusting the active secondary mirror. These parameters are controlled by the OBS-ID numbers, as given in Fig. 5.6. For different targets, the IRIS planner can choose from a variety of pre-defined observing tables. See more details in ITN 31.

There are also other timeline operations, such as setting the global automatic exposure control (AEC) parameters especially when changing between the active region and quiet sun observations, setting the ISS (image stabilization system) loop to stabilize the pointing for high resolution imaging spectroscopy.

Before the submission, the timeline needs to be double checked to make sure that it meets all the requirements in the checklist (ITN 8). Fig. 5.7 shows a completed timeline from 4 UT Mar 30 to 4 UT Apr 1 in 2018. The black filled region shows how the predicted memory usage evolves with the performing of the programs, while the green line over plotted shows the actual memory usage. It is important to keep the memory usage low by the end of the timeline. One aim is to get it down to 20 % (ITN 8). As shown in Fig. 5.7 and Fig. 5.8, AEC is enabled (thick black line) in the AR observations, rotation tracking is off or on as desired (green and blue bars). The telescope has a roll of -90°(blue strip) for the prominence observation at the limb, and it is set back to 0°at the end of the timeline.

The timeline for the next day should be submitted by 2 pm PDT (22 UT) and observations start from 4 UT. After the submission the observing plan should be reported to the IRIS team and other planners coordinating observations with IRIS by 5 pm PDT (1 UT next day) (ITN 8).

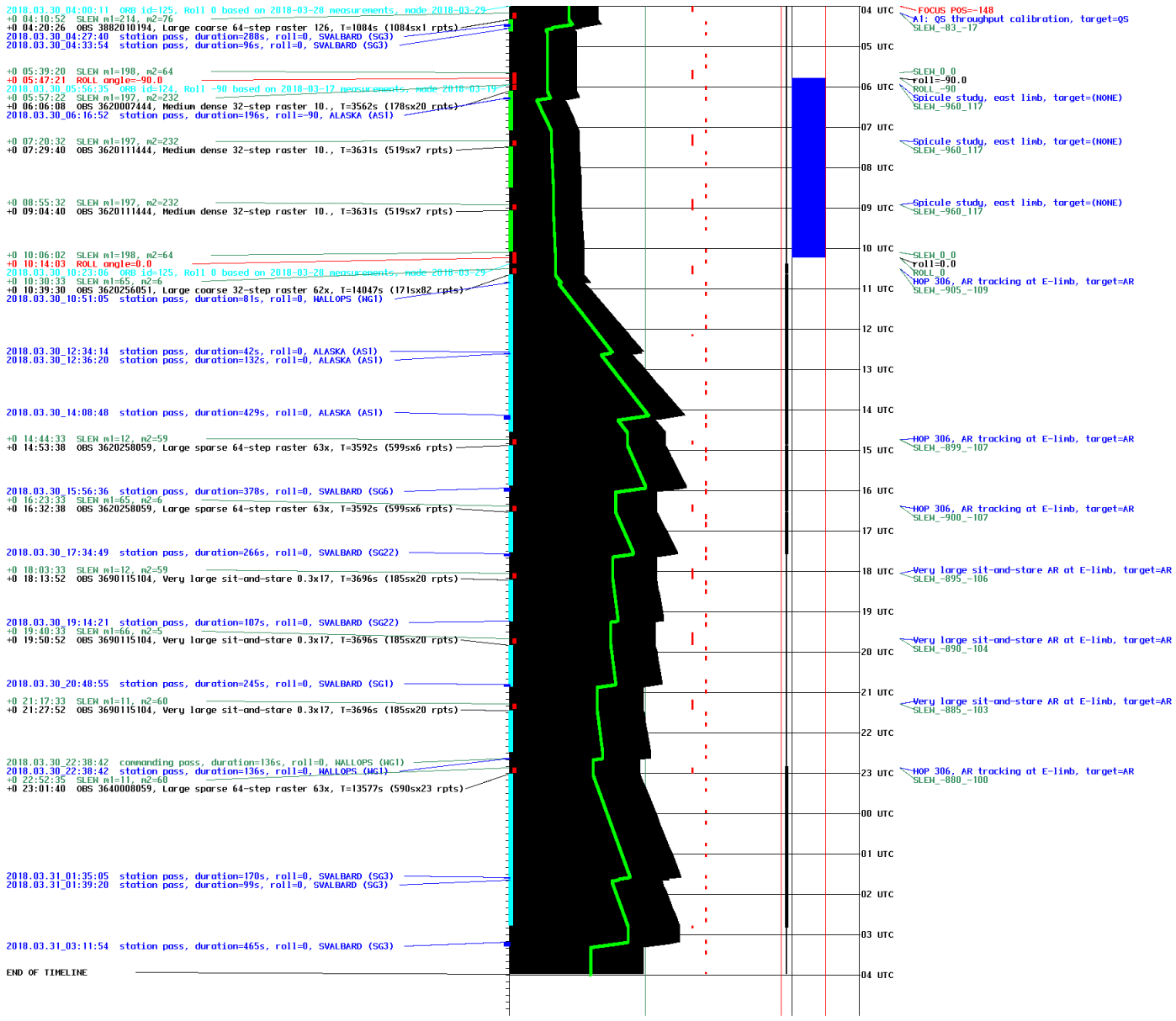

Figure 5.7 Timeline from 4UT Mar 30 to 4UT Apr 1, 2018.

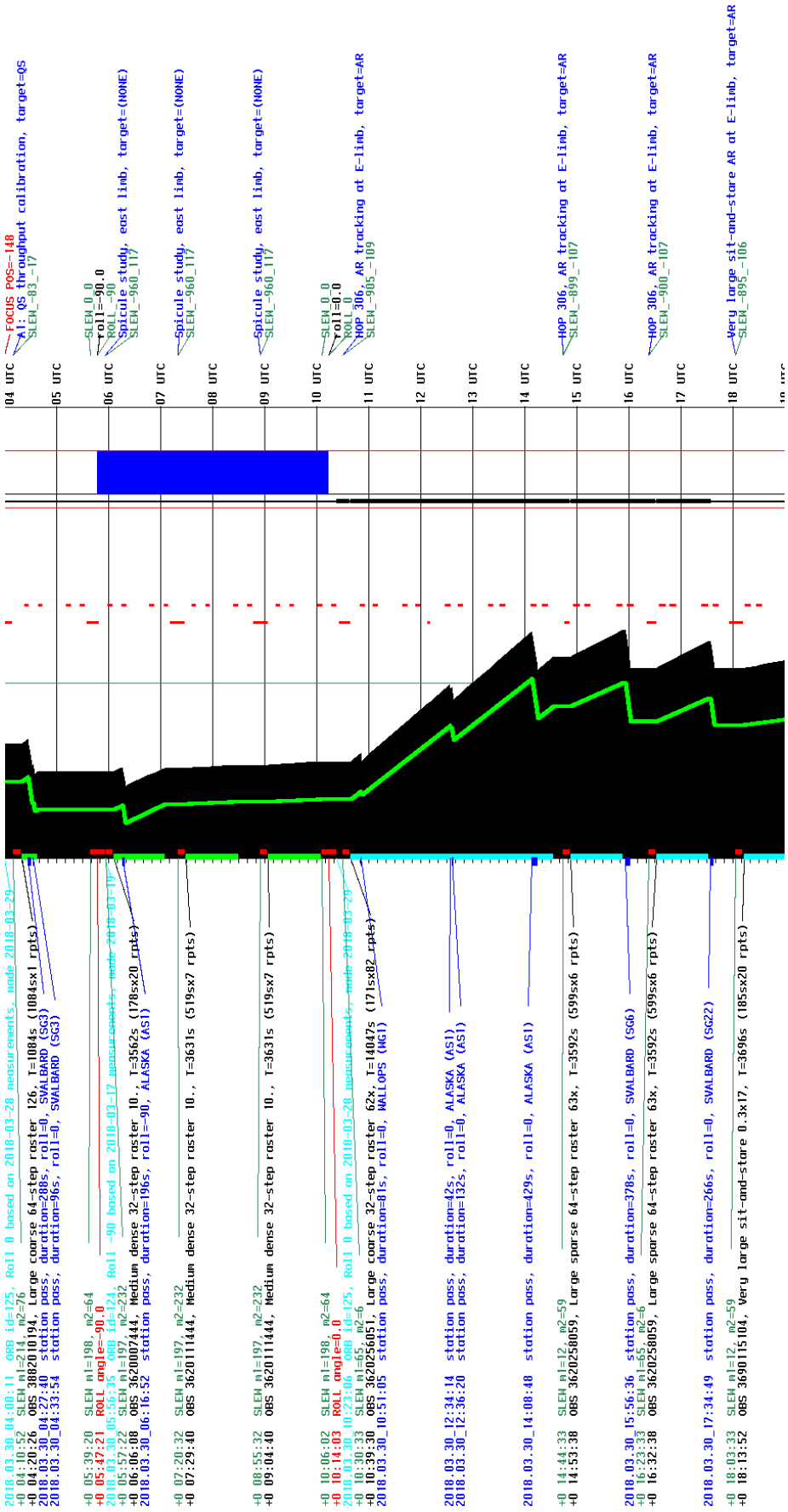

Figure 5.8 Timeline from 4UT to 19 UT on Mar 30, 2018.

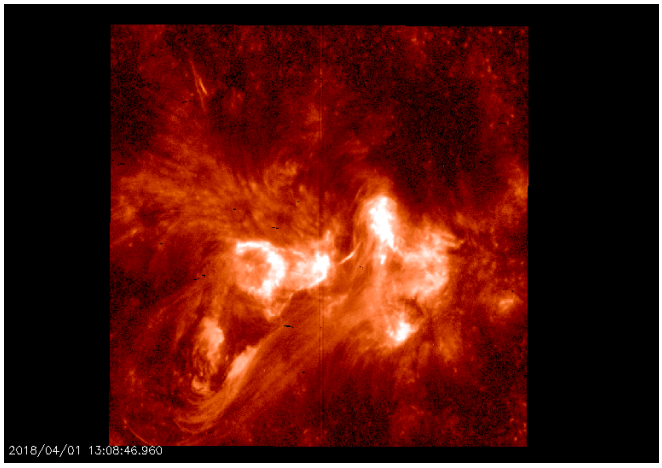

Figure 5.9 One IRIS SJI image at 13:08 UT on Apr 1, 2018 in 1330Å.

5.2 Post-planning activities: data verification and presenting highlights

After the plan is performed everyday, the IRIS planner needs to look through all the data to check if all OBS run as planned, whether the targets are maintained inside the FOV, and if there all datasets are present (ITN 8). After verifying the integrity of the observations, I present to the IRIS team an overview of my planning weeks which contains highlights of the whole-week observations with an emphasis on interesting and eruptive events, e.g., flares, microflares and explosive features. The wobble movies made from low-cadence observations in the planning weeks are also presented to confirm that the orbital wobble is fully corrected for in the observations. One movie of a prominence eruption associated with a flare (one image is shown in Fig. 5.9) is chosen and uploaded as requested to the “IRIS Movie of the Day” web page [5]. These visually interesting movies can offer an insight into solar physics as well as the outputs of IRIS to the non-specialists. Several small flares and sprays observed in my planning weeks are annotated using the annotation tool provided by Ryan from LMSAL IRIS science team. The annotation is aimed at collecting the timing and location information of significant and eruptive events, so that these events can be studied by a larger number of researchers.

5.3 Conclusions

This opportunity of operating a NASA spacecraft as an IRIS planner is an invaluable experience and an important component of my PhD education. Apart from maximizing the science output of IRIS, this program provides a unique hands-on training opportunity for me, allowing me to acquire the understanding necessary to best exploit the data. I also had the opportunity to run several sequences of my own science observing programs dedicated to capture erupting

[5] http://iris.lmsal.com/mod

prominences and to study spicules during my planning weeks. For both observations, the programs are arranged carefully to avoid the South Atlantic Anomaly (SAA) region to reduce the bright hits caused by energetic particles. In my first planning week, I focused on the long prominence across the east limb with several different OBS, trying to find the best compromise between a large field-of-view, the best time and spatial resolutions in order to increase the chances of observing an eruption. By observing the chosen prominence for eight orbits through three days in the planning week, I anticipated to capture prominence eruptions to study the balance of mass flows during the eruption with a proper diagnostic of the density and the combined measurements of a full velocity vector (see Chapter 3). Although the prominence did not erupt during the observation, rotations and small-scale motions are continuously detected, which will be useful for my future quantitative analysis of the dynamics and physical properties of prominences. In my second planning week, I ran several orbits of spicule observations at different positions (north pole, south pole, east limb and west limb) with different roll angles, when there was no good targets for the prominence observation. The spicules can be clearly observed in the monochromatic images and the data can be used for spicule modeling with NLTE codes in IAS.

In addition, this planning experience may also be useful to me e.g., in the context of understanding and preparing observations for future solar physics missions, such as Solar Orbiter and the Advanced Space-based Solar Observatory (ASO-S).

Chapter 6

Discussion and Conclusion

As discussed in Chapter 1, the issue of the prominence eruption (PE) mechanism is of critical importance for both solar physics and space weather, since PEs are often associated with flares and CMES. Our approach has been to obtain as much information as possible from joint observations involving IRIS and other space and ground-based instruments such as SDO/AIA, STEREO/EUVI and K-Cor.

We essentially relied upon the unique spectro-imaging capabilities of IRIS in a set of the Mg II doublet lines, allowing for the access to cool (8 000 K) and warm (up to 12 000 K) temperatures which characterize the mass bulk of prominences. At these temperatures, it is critical to perform a complete diagnostic of the prominence in terms of densities, velocities (POS and LOS), ionization degrees and mass flows, taking into account their variations in time and space. The limited FOV and observing time of the prominence observations drive us to focus on the activation phase of the eruption, for it is too difficult to follow in the later phase, beyond about 0.3 $R_\odot$ above the solar limb. However, we tried to fully use the gathered information that we processed into unique diagnostics of the prominence during the activation phase. Our methods and results can be summarized as follows.

1. Based on the 3D reconstruction with SDO and STEREO images, we find that the main body of the prominence is behind the limb as seen from the Earth, with an inclination angle (between the prominence motion axis and the POS) to be around 60° during the activation. Through an optical flow method, from the AIA 304 Å images and IRIS SJI images in the Mg IIk and h lines, we derived a changing pattern of POS velocities in the range of 0-20 km/s. The sign of these velocities is of major importance for determining the net balance between outward and inward motions. We found upward motions at the top, related to the eruption itself which started at an altitude of about 100 Mm. But we also found at lower altitudes, downward motions that, in terms of mass dominate the overall mass balance. Horizontal motions at the center of the structure probably correspond to projections of horizontal flows along the spine.

Using an extremum-finding algorithm, we derived Doppler velocity maps from spatially-resolved IRIS Mg II h&k profiles. We found that Doppler redshifts dominated in the lower part of the prominence. The large variation in the profile shapes introduces uncertainties when applying this algorithm, especially for complex profiles containing several independent components. In this case, we computed the average shifts which underestimate the shifts as well as the Doppler velocities. For each pixel, we derived a full velocity vector of the observed prominence by combing the POS velocities with the Doppler velocities from simultaneous IRIS spectra and images, taking into account their different cadences. Based on the prominence geometry, we could derive that some Doppler motions are the LOS components of the motions seen in the POS.

2. For prominence diagnostics with Mg II h&k lines, we relied on 1D NLTE radiative transfer code PRODOP_Mg to build pixel per pixel maps of the temperatures, densities and ionization degrees. In this computation, we used a grid of isothermal and isobaric models without PCTR, considering that the thickness of PCTR may vary with the LOS and adding a PCTR will lead to more parameters to control.

   As discussed in Chapter 4, by focusing on the integrated intensities for both k and h lines, we established that the line intensities increased with the hydrogen and electron densities and the corresponding EM for low velocities. Such a correlation that is relatively insensitive to temperature should help derive the density directly from observations.

   By comparing Mg II h&k line intensities from IRIS prominence observations and from the NLTE radiative-transfer modeling with the most accurate computation of the k and h profiles incident on the prominence, we derived electron densities ranging from 1.3×10^9 to 7.0×10^{10} cm^{-3}, Hydrogen densities ranging from 1.5×10^9 to 3.6×10^{11} cm^{-3} and a mean temperature of about 1.1×10^4K which is higher than in quiescent prominences. The ionization degree increases at the edges with values in the range 0.1–10. These low values for an activated prominence, especially in the central parts of the prominence, may imply the heating tendency in peripheral regions. We estimated the total mass of the prominence in the range of 1.3×10^{14} to 3.0×10^{14} g and a total mass drainage from the prominence which is not negligible during the activation. Considering the dominant downward flows through the activation, it could be related to the loss of equilibrium.

The diagnostics of Mg II k&h lines can provide us with a better understanding of the distributions and evolutions of the physical parameters of eruptive prominences. In this thesis, we analyzed observations with various observing limitations including the restricted FOV, the limited duration and the low raster cadence, as well as the unfavourable geometry which makes

it difficult to detect the small-scale structures (e.g., cavities and blobs). In a future study, we will search for other observations of PEs that start before they erupt and we also plan to make a quantitative analysis of more spectroscopic observations of PEs with a larger FOV, longer observing times and different geometries from satellites as well as from Ground-Based observatories. A machine learning technique would also be used to perform a more precise analysis of the numerous complex profiles.

In this thesis, we used 1D NLTE radiative transfer modeling without radial velocity. We will study the effects of the 3D velocity and density structures on the NLTE diagnostic of the prominence plasma. A PCTR will be added in our models and once the geometry of the prominences studied is well characterized, 2D NLTE models for Mg II lines which is going to be available at IAS will be used. In addition, our methods can be applied to the data from future instruments (e.g., SPICE and EUI onboard Solar Orbiter) to study prominence dynamics and perform the diagnostics.

In order to continue studying the physical mechanisms that influence prominence formation, dynamics, and instability, more observing capabilities are required for future instruments. Spectroimaging instruments in UV and EUV with a large FOV and a high time cadence are necessary to study the evolution of thermodynamic properties of the rapid changing large-scale eruptive structures. Complementary spectro-coronagraphy with a FOV down to a lower altitude will help determine the acceleration height of the eruption and provide insights into the rapid formation and evolution of prominence eruptions and CMEs. Since the hydrogen Lyman-α line is the brightest coronal line in EUV, Lyman-α imagery/coronagraphy (e.g., The Lyα Solar Telescope (LST) on the future ASO-S mission) will play an important role in understanding the triggering mechanisms, acceleration processes and physical properties of the eruptions in the low solar corona. All these future capabilities will help understand the unsolved questions in the energy accumulation, triggering and evolution of prominence eruptions.

Bibliography

Alissandrakis, C. E., Vial, J.-C., Koukras, A., Buchlin, E., and Chane-Yook, M. (2018). IRIS Observations of Spicules and Structures Near the Solar Limb. Sol. Phys., 293:20.

Antiochos, S., Dahlburg, R., and Klimchuk, J. (1994). The magnetic field of solar prominences. *The Astrophysical Journal*, 420:L41–L44.

Antiochos, S., MacNeice, P., and Spicer, D. (2000). The thermal nonequilibrium of prominences. *The Astrophysical Journal*, 536(1):494.

Antiochos, S. and Sturrock, P. (1978). Evaporative cooling of flare plasma. *The Astrophysical Journal*, 220:1137–1143.

Antiochos, S. K. (1998). The magnetic topology of solar eruptions. *The Astrophysical Journal Letters*, 502(2):L181.

Anzer, U. (1987). Modelling of the magnetic field of solar prominences. In *Physical Processes in Comets, Stars and Active Galaxies*, pages 61–66. Springer.

Auer, L. and Mihalas, D. (1969). Non-LTE model atmospheres. i. radiative equilibrium models with-alpha. *The Astrophysical Journal*, 156:157.

Aulanier, G. and Démoulin, P. (1998). 3-d magnetic configurations supporting prominences. i. the natural presence of lateral feet. *Astronomy and Astrophysics*, 329:1125–1137.

Aulanier, G. and Démoulin, P. (2003). Amplitude and orientation of prominence magnetic fields from constant-α magnetohydrostatic models. *Astronomy & Astrophysics*, 402(2):769–780.

Aulanier, G., DeVore, C., and Antiochos, S. (2002). Prominence magnetic dips in three-dimensional sheared arcades. *The Astrophysical Journal Letters*, 567(1):L97.

Avrett, E. and Loeser, R. (1992). The pandora atmosphere program (invited review). In *Cool Stars, Stellar Systems, and the Sun*, volume 26, page 489.

Avrett, E. H. and Loeser, R. (1987). Iterative solution of multilevel transfer problems. *Numerical Radiative Transfer*, page 135.

Babcock, H. W. and Babcock, H. D. (1955). The sun's magnetic field, 1952-1954. *The Astrophysical Journal*, 121:349.

Bemporad, A. (2009). Stereoscopic reconstruction from stereo/euv imagers data of the three-dimensional shape and expansion of an erupting prominence. *The Astrophysical Journal*, 701(1):298.

Berger, T. (2013). Solar prominence fine structure and dynamics. *Proceedings of the International Astronomical Union*, 8(S300):15–29.

Berger, T. E., Shine, R. A., Slater, G. L., Tarbell, T. D., Okamoto, T. J., Ichimoto, K., Katsukawa, Y., Suematsu, Y., Tsuneta, S., Lites, B. W., et al. (2008). Hinode sot observations of solar quiescent prominence dynamics. *The Astrophysical Journal Letters*, 676(1):L89.

Bhatnagar, A. and Livingston, W. C. (2005). *Fundamentals of solar astronomy*, volume 6. World Scientific.

Boerner, P., Edwards, C., Lemen, J., Rausch, A., Schrijver, C., Shine, R., Shing, L., Stern, R., Tarbell, T., Wolfson, C. J., et al. (2011). Initial calibration of the atmospheric imaging assembly (aia) on the solar dynamics observatory (sdo). In *The Solar Dynamics Observatory*, pages 41–66. Springer.

Bommier, V., Degl'Innocenti, E. L., Leroy, J.-L., and Sahal-Bréchot, S. (1994). Complete determination of the magnetic field vector and of the electron density in 14 prominences from linear polarizaton measurements in the hei d 3 and hα lines. *Solar Physics*, 154(2):231–260.

Bommier, V. and Leroy, J. (1998). Global pattern of the magnetic field vector above neutral lines from 1974 to 1982: Pic-du-midi observations of prominences. In *International Astronomical Union Colloquium*, volume 167, pages 434–438. Cambridge University Press.

Bradski, G. (2000). The OpenCV Library. *Dr. Dobb's Journal of Software Tools*.

Brown, G. M. and Labrosse, N. (2018). The influence of the solar coronal radiation on coronal plasma structures, i: Determination of the incident coronal radiation. *Solar Physics*, 293(2):35.

Brueckner, G. E., Howard, R. A., Koomen, M. J., Korendyke, C. M., Michels, D. J., Moses, J. D., Socker, D. G., Dere, K. P., Lamy, P. L., Llebaria, A., Bout, M. V., Schwenn, R., Simnett, G. M., Bedford, D. K., and Eyles, C. J. (1995). The Large Angle Spectroscopic Coronagraph (LASCO). Sol. Phys., 162:357–402.

Burkepile, J., Tomczyk, S., Lin, H., Zurbuchen, T., and Casini, R. (2007). Cosmo: The coronal solar magnetism observatory. In *Bulletin of the American Astronomical Society*, volume 39, page 134.

Çelik, G., Ateş, Ş., Özarslan, S., and Taşer, M. (2011). Transition probabilities, oscillator strengths and lifetimes for singly ionized magnesium. *J. Quant. Spectrosc. Radiat. Transfer*, 112:2330–2334.

Chae, J. (2001). Observational determination of the rate of magnetic helicity transport through the solar surface via the horizontal motion of field line footpoints. *The Astrophysical Journal Letters*, 560(1):L95.

Chae, J., Moon, Y.-J., and Park, Y.-D. (2005). The magnetic structure of filament barbs. *The Astrophysical Journal*, 626(1):574.

Chae, J., Wang, H., Qiu, J., Goode, P. R., Strous, L., and Yun, H. (2001). The formation of a prominence in active region noaa 8668. i. soho/mdi observations of magnetic field evolution. *The Astrophysical Journal*, 560(1):476.

Chane-Yook, M. (2015). Prom7: Non-LTE radiative transfer in solar prominences and filaments. Technical report, IAS.

Chatterjee, P. and Fan, Y. (2013). Simulation of Homologous and Cannibalistic Coronal Mass Ejections produced by the Emergence of a Twisted Flux Rope into the Solar Corona. ApJ, 778:L8.

Chiuderi, C. and Drago, F. C. (1991). Energy balance in the prominence-corona transition region. *Solar Physics*, 132(1):81–94.

Cirigliano, D., Vial, J. C., and Rovira, M. (2004). Prominence corona transition region plasma diagnostics from SOHO observations. Sol. Phys., 223:95–118.

De Pontieu, B., Title, A. M., Lemen, J. R., Kushner, G. D., Akin, D. J., Allard, B., Berger, T., Boerner, P., Cheung, M., Chou, C., Drake, J. F., Duncan, D. W., Freeland, S., Heyman, G. F., Hoffman, C., Hurlburt, N. E., Lindgren, R. W., Mathur, D., Rehse, R., Sabolish, D., Seguin, R., Schrijver, C. J., Tarbell, T. D., Wülser, J. P., Wolfson, C. J., Yanari, C., Mudge, J., Nguyen-Phuc, N., Timmons, R., van Bezooijen, R., Weingrod, I., Brookner, R., Butcher, G., Dougherty, B., Eder, J., Knagenhjelm, V., Larsen, S., Mansir, D., Phan, L., Boyle, P., Cheimets, P. N., DeLuca, E. E., Golub, L., Gates, R., Hertz, E., McKillop, S., Park, S., Perry, T., Podgorski, W. A., Reeves, K., Saar, S., Testa, P., Tian, H., Weber, M., Dunn, C., Eccles, S., Jaeggli, S. A., Kankelborg, C. C., Mashburn, K., Pust, N., Springer, L., Carvalho, R., Kleint, L., Marmie, J., Mazmanian, E., Pereira, T. M. D., Sawyer, S., Strong, J., Worden, S. P., Carlsson, M., Hansteen, V. H., Leenaarts, J., Wiesmann, M., Aloise, J., Chu, K. C., Bush, R. I., Scherrer, P. H., Brekke, P., Martinez-Sykora, J., Lites, B. W., McIntosh, S. W., Uitenbroek, H., Okamoto, T. J., Gummin, M. A., Auker, G., Jerram, P., Pool, P., and Waltham, N. (2014). The Interface Region Imaging Spectrograph (IRIS). Sol. Phys., 289:2733–2779.

Del Zanna, G. (2005). An atomic database for spectroscopic diagnostics of astrophysical plasmas.

Démoulin, P. and Priest, E. (1989). A twisted flux model for solar prominences. ii-formation of a dip in a magnetic structure before the formation of a solar prominence. *Astronomy and Astrophysics*, 214:360–368.

Deng, Y., Schmieder, B., Engvold, O., DeLuca, E., and Golub, L. (2000). Emergence of sheared magnetic flux tubes in an active region observed with the svst and trace. *Solar Physics*, 195(2):347–366.

DeVore, C. R. and Antiochos, S. K. (2000). Dynamical formation and stability of helical prominence magnetic fields. *The Astrophysical Journal*, 539(2):954.

Engvold, O. (1998). Observations of filament structure and dynamics. In *International Astronomical Union Colloquium*, volume 167, pages 22–31. Cambridge University Press.

Engvold, O., Hirayama, T., Leroy, J. L., Priest, E. R., and Tandberg-Hanssen, E. (1990). Hvar reference atmosphere of quiescent prominences. In *Dynamics of Quiescent Prominences*, pages 294–297. Springer.

Engvold, O. and Jensen, E. (1977). On Pikel'ner's theory of prominences. *Solar Physics*, 52(1):37–40.

Fan, Y. (2009). Magnetic fields in the solar convection zone. *Living Reviews in Solar Physics*, 6(1):4.

Fan, Y. (2012). Thermal Signatures of Tether-cutting Reconnections in Pre-eruption Coronal Flux Ropes: Hot Central Voids in Coronal Cavities. ApJ, 758:60.

Fan, Y. (2015). MHD Equilibria and Triggers for Prominence Eruption. In Vial, J.-C. and Engvold, O., editors, *Solar Prominences*, volume 415 of *Astrophysics and Space Science Library*, page 297.

Fan, Y. and Gibson, S. (2003). The emergence of a twisted magnetic flux tube into a preexisting coronal arcade. *The Astrophysical Journal Letters*, 589(2):L105.

Farnebäck, G. (2003). Two-frame motion estimation based on polynomial expansion. In Bigun, J. and Gustavsson, T., editors, *Image Analysis*, pages 363–370, Berlin, Heidelberg. Springer Berlin Heidelberg.

Fontenla, J., Rovira, M., Vial, J.-C., and Gouttebroze, P. (1996). Prominence thread models including ambipolar diffusion. *The Astrophysical Journal*, 466:496.

Forbes, T. (2000). A review on the genesis of coronal mass ejections. *Journal of Geophysical Research: Space Physics*, 105(A10):23153–23165.

Forland, B., Gibson, S., Dove, J., Rachmeler, L., and Fan, Y. (2013). Coronal cavity survey: Morphological clues to eruptive magnetic topologies. In *Coronal Magnetometry*, pages 141–153. Springer.

Gibson, S. and Fan, Y. (2006). Coronal prominence structure and dynamics: A magnetic flux rope interpretation. *Journal of Geophysical Research: Space Physics*, 111(A12).

Gilbert, H. R., Holzer, T. E., and MacQueen, R. (2005). A new technique for deriving prominence mass from soho/eit fe xii (19.5 nanometers) absorption features. *The Astrophysical Journal*, 618(1):524.

Gosain, S., Schmieder, B., Venkatakrishnan, P., Chandra, R., and Artzner, G. (2009). 3d evolution of a filament disappearance event observed by stereo. *Solar Physics*, 259(1-2):13.

Gouttebroze, P., Heinzel, P., and Vial, J. C. (1993). The hydrogen spectrum of model prominences. A&AS, 99:513–543.

Gouttebroze, P. and Labrosse, N. (2000). A ready-made code for the computation of prominence nlte models. *Solar Physics*, 196(2):349–355.

Gouttebroze, P., Labrosse, N., Heinzel, P., and Vial, J.-C. (2002). Prediction of line intensity ratios in solar prominences. In *SOLMAG 2002. Proceedings of the magnetic coupling of the solar atmosphere Euroconference*, volume 505, pages 421–424.

Gunár, S., Mein, P., Schmieder, B., Heinzel, P., and Mein, N. (2012). Dynamics of quiescent prominence fine structures analyzed by 2D non-LTE modelling of the Hα line. A&A, 543:A93.

Gunár, S., Parenti, S., Anzer, U., Heinzel, P., and Vial, J.-C. (2011). Synthetic differential emission measure curves of prominence fine structures. II. The SoHO/SUMER prominence of 8 June 2004. A&A, 535:A122.

Heasley, J. N. and Mihalas, D. (1976). Structure and spectrum of quiescent prominences - Energy balance and hydrogen spectrum. ApJ, 205:273–285.

Heasley, J. N. and Milkey, R. W. (1976). Structure and spectrum of quiescent prominences. II - Hydrogen and helium spectra. ApJ, 210:827–835.

Heasley, J. N. and Milkey, R. W. (1983). Structure and spectrum of quiescent prominences. IV - The ultraviolet ionization continua of hydrogen and helium. ApJ, 268:398–402.

Heinzel, P. (2007). The fine structure of solar prominences. *arXiv preprint arXiv:0705.1464*.

Heinzel, P. (2015). Radiative transfer in solar prominences. In *Solar Prominences*, pages 103–130. Springer.

Heinzel, P. and Anzer, U. (1999). Magnetic dips in prominences. *Solar Physics*, 184(1):103–111.

Heinzel, P., Anzer, U., and Gunár, S. (2005). Prominence fine structures in a magnetic equilibrium. II. A grid of two-dimensional models. A&A, 442:331–343.

Heinzel, P., Bommier, V., and Vial, J. C. (1996). A Complex Diagnostic of Solar Prominences. Sol. Phys., 164:211–222.

Heinzel, P., Gouttebroze, P., and Vial, J.-C. (1987). Formation of the hydrogen spectrum in quiescent prominences-one-dimensional models with standard partial redistribution. *Astronomy and Astrophysics*, 183:351–362.

Heinzel, P., Gouttebroze, P., and Vial, J.-C. (1994). Theoretical correlations between prominence plasma parameters and the emitted radiation. A&A, 292:656–668.

Heinzel, P., Schmieder, B., Fárník, F., Schwartz, P., Labrosse, N., Kotrč, P., Anzer, U., Molodij, G., Berlicki, A., DeLuca, E., et al. (2008). Hinode, trace, soho, and ground-based observations of a quiescent prominence. *The Astrophysical Journal*, 686(2):1383.

Heinzel, P., Vial, J.-C., and Anzer, U. (2014). On the formation of mg ii h and k lines in solar prominences. *Astronomy & Astrophysics*, 564:A132.

Hirayama, T. (1971). Spectral analysis of four quiescent prominences observed at the peruvian eclipse. *Solar Physics*, 17(1):50–75.

Hirayama, T. (1985). Modern observations of solar prominences. Sol. Phys., 100:415–434.

Hood, A. and Anzer, U. (1988). Thermal condensations in coronal magnetic fields. *Solar physics*, 115(1):61–80.

Hood, A. W. and Priest, E. R. (1981). Critical conditions for magnetic instabilities in force-free coronal loops. *Geophys. Astrophys. Fluid Dyn.*, 17:297–318.

Howard, R. A., Moses, J. D., Vourlidas, A., Newmark, J., Socker, D., Plunkett, S., Korendyke, C., Cook, J., Hurley, A., Davila, J., et al. (2008). Sun earth connection coronal and heliospheric investigation (secchi). *Space Science Reviews*, 136(1-4):67.

Huber, K.-P. (2013). *Molecular spectra and molecular structure: IV. Constants of diatomic molecules*. Springer Science & Business Media.

Inhester, B. (2006). Stereoscopy basics for the stereo mission. *arXiv preprint astro-ph/0612649*.

Isenberg, P. A. and Forbes, T. G. (2007). A three-dimensional line-tied magnetic field model for solar eruptions. *The Astrophysical Journal*, 670(2):1453.

Ivanov-Kholodnyi, G. and Nikol'Skii, G. (1961). Ultraviolet solar radiation and the transition layer between the chromosphere and the corona. *Soviet Astronomy*, 5:31.

Jejčič, S., Schwartz, P., Heinzel, P., Zapiór, M., and Gunár, S. (2018). Statistical analysis of uv spectra of a quiescent prominence observed by iris. *Astronomy & Astrophysics*, 618:A88.

Kaiser, M. L., Kucera, T., Davila, J., Cyr, O. S., Guhathakurta, M., and Christian, E. (2008). The stereo mission: An introduction. *Space Science Reviews*, 136(1-4):5–16.

Karpen, J. and Antiochos, S. (2008). Condensation formation by impulsive heating in prominences. *The Astrophysical Journal*, 676(1):658.

Karpen, J. T., Antiochos, S. K., and DeVore, C. R. (2012). The mechanisms for the onset and explosive eruption of coronal mass ejections and eruptive flares. *The Astrophysical Journal*, 760(1):81.

Kippenhahn, R. and Schlüter, A. (1957). Eine theorie der solaren filamente. mit 7 textabbildungen. *Zeitschrift fur Astrophysik*, 43:36.

Kohl, J. and Parkinson, W. (1976). The mg ii h and k lines. i-absolute center and limb measurements of the solar profiles. *The Astrophysical Journal*, 205:599–611.

Kopp, R. and Pneuman, G. (1976). Magnetic reconnection in the corona and the loop prominence phenomenon. *Solar Physics*, 50(1):85–98.

Kumar, P., Karpen, J. T., Antiochos, S. K., Wyper, P. F., DeVore, C. R., and DeForest, C. E. (2018). Evidence for the Magnetic Breakout Model in an Equatorial Coronal-hole Jet. ApJ, 854:155.

Kuperus, M. and Raadu, M. (1974). The support of prominences formed in neutral sheets. *Astronomy and Astrophysics*, 31:189.

Kuperus, M. and Tandberg-Hanssen, E. (1967). The nature of quiescent solar prominences. *Solar Physics*, 2(1):39–48.

Labrosse, N. (2015). Derivation of the major properties of prominences using nlte modelling. In *Solar Prominences*, pages 131–155. Springer.

Labrosse, N. and Gouttebroze, P. (2004). Non-LTE radiative transfer in model prominences. i. integrated intensities of he i triplet lines. *The Astrophysical Journal*, 617(1):614.

Labrosse, N., Heinzel, P., Vial, J.-C., Kucera, T., Parenti, S., Gunßr, S., Schmieder, B., and Kilper, G. (2010). Physics of solar prominences: I—spectral diagnostics and non-LTE modelling. *Space Science Reviews*, 151(4):243–332.

Labrosse, N. and McGlinchey, K. (2012). Plasma diagnostic in eruptive prominences from sdo/aia observations at 304 å. *Astronomy & Astrophysics*, 537:A100.

Landi, E., Young, P., Dere, K., Del Zanna, G., and Mason, H. (2013). Chianti—an atomic database for emission lines. xiii. soft x-ray improvements and other changes. *The Astrophysical Journal*, 763(2):86.

Leenaarts, J., Pereira, T. M. D., Carlsson, M., Uitenbroek, H., and De Pontieu, B. (2013). The formation of iris diagnostics. ii. the formation of the mg ii h&k lines in the solar atmosphere. *The Astrophysical Journal*, 772(2):90.

Lemaire, P., Emerich, C., Curdt, W., Schühle, U., and Wilhelm, K. (1998). Solar h i lyman alpha full disk profile obtained with the sumer/soho spectrometer. *Astronomy and Astrophysics*, 334:1095–1098.

Lemen, J. R., Akin, D. J., Boerner, P. F., Chou, C., Drake, J. F., Duncan, D. W., Edwards, C. G., Friedlaender, F. M., Heyman, G. F., Hurlburt, N. E., et al. (2011). The atmospheric imaging assembly (aia) on the solar dynamics observatory (sdo). In *The Solar Dynamics Observatory*, pages 17–40. Springer.

Leroy, J., Bommier, V., and Sahal-Brechot, S. (1984). New data on the magnetic structure of quiescent prominences. *Astronomy and Astrophysics*, 131:33–44.

Levens, P., Labrosse, N., Schmieder, B., Ariste, A. L., and Fletcher, L. (2017). Comparing uv/euv line parameters and magnetic field in a quiescent prominence with tornadoes. *Astronomy & Astrophysics*, 607:A16.

Levens, P., Schmieder, B., Labrosse, N., and Ariste, A. L. (2016). Structure of prominence legs: plasma and magnetic field. *The Astrophysical Journal*, 818(1):31.

Liewer, P., De Jong, E., Hall, J., Howard, R., Thompson, W., Culhane, J., Bone, L., and van Driel-Gesztelyi, L. (2009). Stereoscopic analysis of the 19 may 2007 erupting filament. *Solar Physics*, 256(1-2):57–72.

Lin, Y., Engvold, O., Van der Voort, L. R., and van Noort, M. (2007). Evidence of traveling waves in filament threads. *Solar Physics*, 246(1):65–72.

Lin, Y., Engvold, O., van der Voort, L. R., Wiik, J. E., and Berger, T. E. (2005a). Thin threads of solar filaments. *Solar Physics*, 226(2):239–254.

Lin, Y., Engvold, O., and Wiik, J. E. (2003). Counterstreaming in a large polar crown filament. *Solar Physics*, 216(1-2):109–120.

Lin, Y., Martin, S., and Engvold, O. (2008a). Filament substructures and their interrelation. In *Subsurface and Atmospheric Influences on Solar Activity*, volume 383, page 235.

Lin, Y., Martin, S., Engvold, O., van der Voort, L. R., and van Noort, M. (2008b). On small active region filaments, fibrils and surges. *Advances in Space Research*, 42(5):803–811.

Lin, Y., Soler, R., Engvold, O., Ballester, J., Langangen, Ø., Oliver, R., and van der Voort, L. R. (2009). Swaying threads of a solar filament. *The Astrophysical Journal*, 704(1):870.

Lin, Y., Wiik, J. E., Engvold, O., Van Der Voort, L. R., and Frank, Z. A. (2005b). Solar filaments and photospheric network. *Solar Physics*, 227(2):283–297.

Litvinenko, Y. E. and Martin, S. F. (1999). Magnetic reconnection as the cause of a photospheric canceling feature and mass flows in a filament. *Solar Physics*, 190(1-2):45–58.

Liu, R. and Alexander, D. (2009). Hard x-ray emission in kinking filaments. *The Astrophysical Journal*, 697(2):999.

Liu, W., Berger, T. E., and Low, B. (2012). First sdo/aia observation of solar prominence formation following an eruption: Magnetic dips and sustained condensation and drainage. *The Astrophysical Journal Letters*, 745(2):L21.

Liu, W., De Pontieu, B., Vial, J.-C., Carlsson, M., Uitenbroek, H., Okamoto, T. J., Berger, T. E., Antolin, P., et al. (2015). First high-resolution spectroscopic observations of an erupting prominence within a coronal mass ejection by the interface region imaging spectrograph (iris). *The Astrophysical Journal*, 803(2):85.

Liu, Y. D., Hu, H., Wang, C., Luhmann, J. G., Richardson, J. D., Yang, Z., and Wang, R. (2016). On sun-to-earth propagation of coronal mass ejections: Ii. slow events and comparison with others. *The Astrophysical Journal Supplement Series*, 222(2):23.

Liu, Y. D., Luhmann, J. G., Lugaz, N., Möstl, C., Davies, J. A., Bale, S. D., and Lin, R. P. (2013). On sun-to-earth propagation of coronal mass ejections. *The astrophysical journal*, 769(1):45.

Low, B. (2001). Coronal mass ejections, magnetic flux ropes, and solar magnetism. *Journal of Geophysical Research: Space Physics*, 106(A11):25141–25163.

Mackay, D. H., Karpen, J. T., Ballester, J. L., Schmieder, B., and Aulanier, G. (2010). Physics of Solar Prominences: II – Magnetic Structure and Dynamics. *Space Science Reviews*, 151:333–399.

Magara, T. (2004). A model for dynamic evolution of emerging magnetic fields in the sun. *The Astrophysical Journal*, 605(1):480.

Malherbe, J.-M. (1988). The formation of solar prominences. In *Dynamics and structure of quiescent solar prominences*, pages 115–141. Springer.

Martin, S. (1998). Solar phys. 182, 107. doi: 10.1023.

Martin, S. F., Bilimoria, R., and Tracadas, P. W. (1994). Magnetic field configurations basic to filament channels and filaments. In *Solar surface magnetism*, pages 303–338. Springer.

Martin, S. F., Marquette, W. H., and Bilimoria, R. (1992). The solar cycle pattern in the direction of the magnetic field along the long axes of polar filaments. In *The solar cycle*, volume 27, page 53.

Mathioudakis, M., McKenny, J., Keenan, F., Williams, D., and Phillips, K. (1999). The effects of opacity in the transition region of yz cmi. *Astronomy and Astrophysics*, 351:L23–L26.

McCauley, P. I., Su, Y. N., Schanche, N., Evans, K. E., Su, C., McKillop, S., and Reeves, K. K. (2015). Prominence and Filament Eruptions Observed by the Solar Dynamics Observatory: Statistical Properties, Kinematics, and Online Catalog. Sol. Phys., 290:1703–1740.

Mok, Y., Drake, J., Schnack, D., and Van Hoven, G. (1990). Prominence formation in a coronal loop. *The Astrophysical Journal*, 359:228–231.

Moore, R. L. and Roumeliotis, G. (1992). Triggering of eruptive flares: destabilization of the preflare magnetic field configuration. In *Eruptive Solar Flares*, pages 69–78. Springer.

Morgan, H., Habbal, S. R., and Lugaz, N. (2009). Mapping the Structure of the Corona Using Fourier Backprojection Tomography. ApJ, 690:1119–1129.

Morgan, H., Habbal, S. R., and Woo, R. (2006). The depiction of coronal structure in white-light images. *Solar Physics*, 236(2):263–272.

Paletou, F., Vial, J.-C., and Auer, L. H. (1993). Two-dimensional radiative transfer with partial frequency redistribution. II. Application to resonance lines in quiescent prominences. A&A, 274:571.

Panesar, N. K. (2014). *A Study of quiescent prominences using SDO and STEREO data*. Universitätsverlag Göttingen.

Parenti, S. (2014). Solar prominences: observations. *Living Reviews in Solar Physics*, 11(1):1.

Parenti, S. (2015). Spectral diagnostics of cool prominence and pctr optically thin plasmas. In *Solar Prominences*, pages 61–77. Springer.

Parenti, S. and Vial, J.-C. (2007). Prominence and quiet-sun plasma parameters derived from fuv spectral emission. *Astronomy & Astrophysics*, 469(3):1109–1115.

Parenti, S. and Vial, J.-C. (2013). On the nature of the prominence-corona transition region. *Proceedings of the International Astronomical Union*, 8(S300):69–78.

Pécseli, H. and Engvold, O. (2000). Modeling of prominence threads in magnetic fields: Levitation by incompressible mhd waves. *Solar Physics*, 194(1):73–86.

Pesnell, W. D., T. B. J. and Chamberlin, P. C. (2012). *The Solar Dynamics Observatory (SDO)*, volume 275. Springer.

Pettit, E. (1950). The evidence for tornado prominences. *Publications of the Astronomical Society of the Pacific*, 62:144.

Pottasch, S. R. (1963). The lower solar corona: Interpretation of the ultraviolet spectrum. *The Astrophysical Journal*, 137:945.

Priest, E. (2014). *Magnetohydrodynamics of the Sun*. Cambridge University Press.

Priest, E. and Tandberg-Hanssen, E. (1989). Book-review-dynamics and structure of quiescent solar prominences.

Priest, E. R. (2012). *Dynamics and structure of quiescent solar prominences*, volume 150. Springer Science & Business Media.

Robbrecht, E., Berghmans, D., and Van der Linden, R. A. M. (2009). Automated LASCO CME Catalog for Solar Cycle 23: Are CMEs Scale Invariant? ApJ, 691:1222–1234.

Rust, D. and Kumar, A. (1994). Helical magnetic fields in filaments. *Solar physics*, 155(1):69–97.

Rybicki, G. and Hummer, D. (1992). An accelerated lambda iteration method for multilevel radiative transfer. ii-overlapping transitions with full continuum. *Astronomy and Astrophysics*, 262:209–215.

Rybicki, G. B. and Hummer, D. G. (1991). An accelerated lambda iteration method for multilevel radiative transfer. i-non-overlapping lines with background continuum. *Astronomy and Astrophysics*, 245:171–181.

Sahal-Brechot, S., Malinovsky, M., and Bommier, V. (1986). The polarization of the O VI 1032 A line as a probe for measuring the coronal vector magnetic field via the Hanle effect. A&A, 168:284–300.

Scherrer, P. H., Schou, J., Bush, R., Kosovichev, A., Bogart, R., Hoeksema, J., Liu, Y., Duvall, T., Zhao, J., Schrijver, C., et al. (2012). The helioseismic and magnetic imager (hmi) investigation for the solar dynamics observatory (sdo). *Solar Physics*, 275(1-2):207–227.

Schmieder, B., Tian, H., Kucera, T., Ariste, A. L., Mein, N., Mein, P., Dalmasse, K., and Golub, L. (2014). Open questions on prominences from coordinated observations by iris, hinode, sdo/aia, themis, and the meudon/msdp. *Astronomy & Astrophysics*, 569:A85.

Schmit, D., Bryans, P., De Pontieu, B., McIntosh, S., Leenaarts, J., and Carlsson, M. (2015). Observed Variability of the Solar Mg II h Spectral Line. ApJ, 811:127.

Schrijver, C. J. (2009). Driving major solar flares and eruptions: A review. *Advances in Space Research*, 43(5):739–755.

Schrijver, C. J., Elmore, C., Kliem, B., Török, T., et al. (2008). Observations and modeling of the early acceleration phase of erupting filaments involved in coronal mass ejections. *The Astrophysical Journal*, 674(1):586.

Schwartz, P., Heinzel, P., Kotrč, P., Fárník, F., Kupryakov, Y. A., DeLuca, E., and Golub, L. (2015). Total mass of six quiescent prominences estimated from their multi-spectral observations. *Astronomy & Astrophysics*, 574:A62.

Seaton, D. B., Berghmans, D., Nicula, B., Halain, J.-P., De Groof, A., Thibert, T., Bloomfield, D. S., Raftery, C. L., Gallagher, P. T., Auchère, F., Defise, J.-M., D'Huys, E., Lecat, J.-H., Mazy, E., Rochus, P., Rossi, L., Schühle, U., Slemzin, V., Yalim, M. S., and Zender, J. (2013). The SWAP EUV Imaging Telescope Part I: Instrument Overview and Pre-Flight Testing. Sol. Phys., 286:43–65.

Serio, S., Peres, G., Vaiana, G., Golub, L., and Rosner, R. (1981). Closed coronal structures. ii-generalized hydrostatic model. *The Astrophysical Journal*, 243:288–300.

Shibata, K. (1998). Evidence of magnetic reconnection in solar flares and a unified model of flares. *Astrophysics and Space Science*, 264(1-4):129–144.

Staath, E. and Lemaire, P. (1995). High resolution profiles of the mg ii h and mg ii k lines. *Astronomy and Astrophysics*, 295:517–528.

Stellmacher, G., Koutchmy, S., and Lebecq, C. (1986). The 1981 total solar eclipse. iii-photometric study of the prominence remnant in the reversing south polar field. *Astronomy and Astrophysics*, 162:307–311.

Stellmacher, G., Wiehr, E., and Dammasch, I. (2003). Spectroscopy of solar prominences simultaneously from space and ground. *Solar Physics*, 217(1):133–155.

Sterling, A. C. and Moore, R. L. (2003). Tether-cutting energetics of a solar quiet-region prominence eruption. *The Astrophysical Journal*, 599(2):1418.

Sterling, A. C. and Moore, R. L. (2004a). Evidence for gradual external reconnection before explosive eruption of a solar filament. *The Astrophysical Journal*, 602(2):1024.

Sterling, A. C. and Moore, R. L. (2004b). External and internal reconnection in two filament-carrying magnetic cavity solar eruptions. *The Astrophysical Journal*, 613(2):1221.

Sterling, A. C. and Moore, R. L. (2005). Slow-rise and fast-rise phases of an erupting solar filament, and flare emission onset. *The Astrophysical Journal*, 630(2):1148.

Tandberg-Hanssen, E. (1995). Astrophysics and space science library, vol. 199. *The nature of solar prominences*.

Thompson, W. (2006). Coordinate systems for solar image data. *Astronomy & Astrophysics*, 449(2):791–803.

Thompson, W. T., Davila, J. M., Fisher, R. R., Orwig, L. E., Mentzell, J. E., Hetherington, S. E., Derro, R. J., Federline, R. E., Clark, D. C., Chen, P. T., et al. (2003). Cor1 inner coronagraph for stereo-secchi. In *Innovative Telescopes and Instrumentation for Solar Astrophysics*, volume 4853, pages 1–12. International Society for Optics and Photonics.

Titov, V. S. and Démoulin, P. (1999). Basic topology of twisted magnetic configurations in solar flares. 351:707–720.

van Ballegooijen, A. A. and Martens, P. (1989). Formation and eruption of solar prominences. *The Astrophysical Journal*, 343:971–984.

van Driel-Gesztelyi, L., Attrill, G., Démoulin, P., Mandrini, C., and Harra, L. (2008). Why are cmes large-scale coronal events: nature or nurture? In *Annales geophysicae: atmospheres, hydrospheres and space sciences*, volume 26, page 3077.

van Driel-Gesztelyi, L., Malherbe, J.-M., and Démoulin, P. (2000). Emergence of a u-loop-sub-photospheric link between solar active regions. *Astronomy and Astrophysics*, 364:845–852.

Van Hoven, G., Mok, Y., and Drake, J. (1992). Prominence condensation and magnetic levitation in a coronal loop. *Solar physics*, 140(2):269–287.

Vial, J., Gouttebroze, P., Artzner, G., and Lemaire, P. (1979). Profiles of h i (la), mg ii (h and k), ca ii (h and k) lines of an active filament at the limb, with the lpsp instrument aboard the oso-8 satellite. *Solar Physics*, 61(1):39–59.

Vial, J. C. (1982a). Optically thick lines in a quiescent prominence - Profiles of Lyman-alpha, Lyman-beta /H I/, K and H /Mg II/, and K and H /Ca II/ lines with the OSO 8 LPSP instrument. ApJ, 253:330–352.

Vial, J. C. (1982b). Two-dimensional nonlocal thermodynamic equilibrium transfer computations of resonance lines in quiescent prominences. ApJ, 254:780–795.

Vial, J.-C. (1990). The prominence-corona interface. In *Dynamics of Quiescent Prominences*, pages 106–119. Springer.

Vial, J.-C. and Engvold, O., editors (2015). *Solar Prominences*, volume 415 of *Astrophysics and Space Science Library*.

Vial, J. C., Gouttebroze, P., Artzner, G., and Lemaire, P. (1979). Profiles of H I /L-alpha/, MG II /h and k/, CA II /H and K/ lines of an active filament at the limb, with the LPSP instrument aboard the OSO-8 satellite. Sol. Phys., 61:39–59.

Vial, J.-C., Pelouze, G., Heinzel, P., Kleint, L., and Anzer, U. (2016). Observed iris profiles of the h and k doublet of mg ii and comparison with profiles from quiescent prominence nlte models. *Solar Physics*, 291(1):67–87.

Wang, Y.-M. (1999). The jetlike nature of he ii λ304 prominences. *The Astrophysical Journal Letters*, 520(1):L71.

Wang, Y.-M. and Sheeley Jr, N. (2002). Observations of core fallback during coronal mass ejections. *The Astrophysical Journal*, 567(2):1211.

Webb, D. and Hundhausen, A. (1987). Activity associated with the solar origin of coronal mass ejections. *Solar physics*, 108(2):383–401.

Webb, D. F. and Howard, T. A. (2012). Coronal mass ejections: observations. *Living Reviews in Solar Physics*, 9(1):3.

Woods, T., Eparvier, F., Hock, R., Jones, A., Woodraska, D., Judge, D., Didkovsky, L., Lean, J., Mariska, J., Warren, H., et al. (2010). Extreme ultraviolet variability experiment (eve) on the solar dynamics observatory (sdo): Overview of science objectives, instrument design, data products, and model developments. In *The Solar Dynamics Observatory*, pages 115–143. Springer.

Wülser, J.-P., Jaeggli, S., De Pontieu, B., Tarbell, T., Boerner, P., Freeland, S., Liu, W., Timmons, R., Brannon, S., Kankelborg, C., et al. (2018). Instrument calibration of the interface region imaging spectrograph (iris) mission. *Solar Physics*, 293(11):149.

Wülser, J.-P., Lemen, J. R., Tarbell, T. D., Wolfson, C. J., Cannon, J. C., Carpenter, B. A., Duncan, D. W., Gradwohl, G. S., Meyer, S. B., Moore, A. S., et al. (2004). Euvi: the stereo-secchi extreme ultraviolet imager. In *Telescopes and Instrumentation for Solar Astrophysics*, volume 5171, pages 111–123. International Society for Optics and Photonics.

Zharkova, V. (1989). Toward hydrogen emission in filamentary quiescent prominences. *Hvar Observatory Bulletin*, 13:331.

Zirker, J., Engvold, O., and Martin, S. (1998). Counter-streaming gas flows in solar prominences as evidence for vertical magnetic fields. *Nature*, 396(6710):440.

Zirker, J. B., Engvold, O., and Yi, Z. (1994). Flows in quiescent prominences. *Solar physics*, 150(1-2):81–86.

Appendix A

Computation of the incident radiation

IDL code

```
;;Get the data of IRIS mosaic observation and derive the coordinates
files=file_search('mosaicdata/iris/IRISMosaic_20140527_MgIIk.fits')
data = READFITS(files[0], hdr)
header = FITSHEAD2STRUCT(hdr)
wcs = fitshead2wcs(header,system='A')
xyz= wcs_get_coord(wcs, [0,0,0])
coordx=findgen(1002)*header.CDELT1+xyz[0]
coordy=findgen(6011)*header.CDELT2+xyz[1]
wav=findgen(101)*header.CDELT3+xyz[2]
;;How the intensity at each wavelength changes with the angle mu is stored in 'disk/par
It is derived from IRIS mosaic observation on March 12.
restore,'disk/parak.sav'

dx=header.CDELT1
dy=header.CDELT2
num=0
ALTI=13.6d
;hight above the limb in arcsec, 13.6 corresponds to 10000km.
Rs=953.0d
;radius of the sun in arcsec in Mg II, derived from mosaic observation
RM=Rs+ALTI*1.0d
J=fltarr(101)
theta1=acos(Rs/RM)
psi1=!pi/2.0-theta1

 H= RS/(RS+ALTI)
```

```
 G2=SQRT(1.0-H*H )
 J1 = 0.5*(1.-G2 )*180

px0=905.2
py0=161.4

for k=0,100 do begin
for m=0,1001 do begin
  for n=0,6010  do begin
    px=coordx[m]
    py=coordy[n]
    r=sqrt((px-px0)^2.0+(py-py0)^2.0)
    if (r lt Rs*sin(theta1))  then begin
    theta=asin(r/Rs)
    R1=RM-Rs*cos(theta)
    alpha=atan(r/R1)
    psi=asin((RM/Rs)*sin(alpha))
    mu=cos(psi)
    ds=dx*dy/cos(theta)*mu
    mu0=0.23d
    limbp=parak[k,0]+parak[k,1]*mu0^1.0+parak[k,2]*mu0^2.0+parak[k,3]*mu0^3.0
    limbd=(parak[k,0]+parak[k,1]*mu+parak[k,2]*mu^2.0+parak[k,3]*mu^3.0)/limbp
    ;;limb darknening is taken into account
    D=R1^2.0+r^2.0
    domega=ds/D
    dJ=domega*data[m,n,k]/4/!pi*limbd
    J[k]=J[k]+dJ
    num=num+1
    endif
endfor
endfor
endfor
```

université PARIS-SACLAY
ÉCOLE DOCTORALE
Ondes et Matière (EDOM)

Titre: Les protubérances et leurs éruptions observées avec la mission IRIS et les instruments auxiliaires

Mots clés: filaments, protubérances; spectroscopie; transfert radiatif

Résumé: Les protubérances solaires sont de fascinantes structures magnétiques à grande échelle dans l'atmosphère solaire. Elles sont l'objet de recherches depuis des dizaines d'années mais des questions comme leur formation, leur stabilité et leur éruption ne sont toujours pas bien comprises. Le sujet est d'autant plus important que les éruptions de protubérances sont le plus souvent associées aux éruptions ("flares") et aux éjections de masse coronales qui impactent directement l'atmosphère de la Terre. De grands progrès ont été obtenus dans ce domaine et celui des éruptions en particulier avec une combinaison d'observations synoptiques et continues depuis l'espace (voir SoHO/EIT, STEREO/SECCHI/EUVI, et SDO/AIA) et en spectro-imagerie multilongueurs d'onde. Depuis le lancement du satellite IRIS en 2013, beaucoup de résultats d'observations et de modélisations ont été obtenus grâce à la très haute résolution spectrale et spatiale d'IRIS tant en spectroscopie qu'en imagerie.
Dans cette thèse, nous nous focalisons sur les signatures observationnelles des processus mis en avant pour expliquer les éruptions de protubérances. Nous essayons aussi de déterminer les variations de conditions physiques d'une protubérance éruptive et d'estimer à la fois les masses de matière qui quittent le Soleil et celles qui retournent au Soleil pendant une éruption. En ce qui concerne les vitesses, nous parvenons à construire le vecteur vitesse en chaque pixel de la protubérance observée, grâce à la combinaison d'une méthode de "flot optique" appliquée aux images AIA à 30.4 nm et IRIS Mg II h&k à 280 nm, ce qui donne accès aux vitesses dans le plan du ciel, d'une part, et grâce à la technique Doppler appliquée aux profils IRIS Mg II h&k ce qui permet de calculer les vitesses le long de la ligne de visée, d'autre part. En ce qui concerne les densités et températures, nous comparons les intensités absolues observées avec les valeurs déduites de calculs de transfert radiatif Hors-Equilibre Thermodynamique Local, ce qui nous permet de construire des cartes de ces quantités. Les densités électroniques ainsi déduites sont dans la gamme 1.3×10^9 to 7.0×10^{10} cm^{-3} et les densités totales d'hydrogène dans la gamme 1.5×10^9 to 3.6×10^{11} cm^{-3} dans les diverses régions de la protubérance. La température moyenne est d'environ 1.1×10^4 K, une valeur plus élevée que dans les protubérances quiescentes. Le degré d'ionisation (rapport protons/Hneutre) varie entre 0.1 et 10. Les flux de masse à l'intérieur de la protubérance et leurs variations temporelles ont pu ainsi être calculés. La masse totale d'hydrogène ainsi déduite est dans la gamme 1.3×10^{14} to 3.0×10^{14} g. La perte totale de masse de la protubérance vers la surface solaire évaluée sur la durée d'observation avec IRIS est d'un ordre de grandeur plus faible que la masse totale de la protubérance. Nous explorons aussi les corrélations entre indices spectraux observables dans les raies h et k de Mg II et des quantités physiques comme la densité et la mesure d'émission (ME). Nous avons choisi de calculer des modèles uni-dimensionnels (1D) isothermes et isobares en utilisant le code NLTE PRODOP_Mg disponible à MEDOC (IAS) et en procédant au calcul exact du rayonnement incident. Nous en déduisons des corrélations entre les intensités émergentes dans les raies h et k d'une part, et les densités et les ME d'autre part. Moyennant quelques hypothèses sur la température, nous établissons une relation entre les intensités k (et h) et la ME, une relation qui devrait être utile pour déterminer les densités d'hydrogène et d'électrons aussi bien que l'épaisseur effective d'une protubérance observée. Ainsi donc, l'évolution des propriétés morphologiques et thermodynamiques d'une protubérance éruptive ont été étudiées dans cette thèse. Ces travaux conduisent à une meilleure compréhension de quelques aspects des protubérances (éruptives), tels la distribution et l'évolution des densités, de la température, des vitesses et du degré d'ionisation. Nous avons ainsi fourni des contraintes utiles à la modélisation des protubérances. Un chapitre est aussi dédié à la programmation des observations, effectuée dans le cadre d'une visite effectuée au laboratoire américain chargé de l'instrument IRIS (le LMSAL à Palo Alto). Malgré la complexité de ces opérations nous avons aussi pu obtenir une moisson de résultats nouveaux. A la suite de cette formation, nous avons pu programmer une deuxième semaine d'observations IRIS depuis MEDOC à l'I.A.S.

Title: Prominences and their eruptions as observed with the IRIS mission and ancillary instruments

Keywords: filaments, prominences; spectroscopic; radiative transfer

Abstract: Solar prominences are fascinating, large-scale magnetic structures in the solar atmosphere. They have been investigated for many decades, but the issues of their formation, stability, and eruption are still not well understood.
Much progress has been made in our knowledge of prominences and their eruptions with both synoptic (continuous) measurements from space (with SoHO/EIT, STEREO/SECCHI/EUVI, and SDO/AIA) and multiwavelength spectroimaging. Since the launch of IRIS in 2013, a lot of results have been obtained in both observational and modeling domains with IRIS high spectral and spatial resolution imaging and spectroscopy.
In this thesis we focus on the observational signatures of the processes which have been put forward for explaining eruptive prominences. We also try to figure out the variations of physical conditions of the eruptive prominence and estimate the masses leaving the Sun vs. the masses returning to the Sun during the eruption.
As far as velocities are concerned, we derive a full velocity vector for each pixel of the observed prominence by combining an optical flow method on the AIA 304 Å and IRIS Mg II h images in order to derive the plane-of-sky velocities and a Doppler technique on the IRIS Mg II h&k profiles to compute the line-of-sight velocities. As far as densities and temperatures are concerned, we compare the absolute observed intensities with values derived from Non Local Thermodynamic Equilibrium (NLTE) radiative transfer computations to build pixel per pixel maps of these quantities. The derived electron densities range from 1.3×10^9 to 7.0×10^{10} cm^{-3} and the derived total hydrogen densities range from 1.5×10^9 to 3.6×10^{11} cm^{-3} in different regions of the prominence. The mean temperature is around 1.1×10^4 K which is higher than in quiescent prominences. The ionization degree is in the range of 0.1 to 10.
The mass flows in the prominence and their variations with time are consequently computed. The derived total hydrogen mass is in the range of 1.3×10^{14} to 3.0×10^{14} g. The total mass drainage from the prominence to the solar surface during the whole observation time of IRIS is about one order of magnitude smaller than the total mass of the prominence.
We also explore the correlations between the observable spectral features in h and k lines of Mg II to physical quantities such as the density and the Emission Measure (EM). We choose to compute one-dimensional (1D) isothermal and isobaric models using the PRODOP_Mg NLTE code available at MEDOC (IAS) with the exact computation of the incident radiation. Then we derive correlations between the k and h emergent intensities on one hand and the densities and EM on the other hand. With some assumptions on the temperature we obtain a unique relation between the k (and h) intensities and the EM that should be useful for deriving either the hydrogen and electron densities or the effective thickness of an observed prominence.
Thus, the detailed evolution of the morphology and thermodynamic properties of an erupting prominence have been studied in the thesis. These investigations lead to our understanding in some aspects of prominences, e.g., the distribution and evolution of densities, temperatures, velocities and ionization degree. These could be useful constraints for theoretical prominence models. In the conclusion, we summarize our results and provide some suggestions for future analysis, observations and ideal observing capabilities.

Université Paris-Saclay
Espace Technologique / Immeuble Discovery
Route de l'Orme aux Merisiers RD 128 / 91190 Saint-Aubin, France